Indian Institute of Technology Guwahati

Department of Physics

Relativistic Accretion Flows Around Rotating Black Holes: Effects of Viscosity, Thermal Conduction, and Magnetic Fields

A Thesis Submitted for the Degree of

Doctor of Philosophy (PhD)

by

Monu Singh

Supervised by

Prof. Santabrata Das

December, 2025

Indian Institute of Technology Guwahati, Guwahati


भारतीय प्रौद्योगिकी संस्थान गुवाहाटी
Indian Institute of Technology Guwahati

Declaration

I, Monu Singh (Roll No. 186121001), hereby declare that this thesis, entitled “Relativistic Accretion Flows Around Rotating Black Holes: Effects of Viscosity, Thermal Conduction, and Magnetic Fields”, submitted to Indian Institute of Technology Guwahati for the award of the degree of Doctor of Philosophy, is a record of original research work carried out by me under the supervision of Prof. Santabrata Das.

Signature: ________________________________

Name: Monu Singh
December, 2025

Disclaimer

The views and conclusions expressed in this thesis are those of the author and do not necessarily reflect the opinions or policies of Indian Institute of Technology Guwahati...

Certificate

This is to certify that the work contained in the thesis entitled **"Relativistic Accretion Flows Around Rotating Black Holes: Effects of Viscosity, Thermal Conduction, and Magnetic Fields"** submitted by Mr. Monu Singh in the fulfillment of the requirement for the award of the degree of Doctor of Philosophy in Physics, Department of Physics, Indian Institute of Technology Guwahati, is a record of the candidate's own work carried out by him under my supervision and guidance. The matter embodied in this report has not been submitted in part or full to any other university or institute for the award of any degree.

Dr. Santabrata Das
Professor
Department of Physics
Indian Institute of Technology Guwahati
Guwahati - 781039
Assam, India.

Acknowledgments

I express my deepest gratitude to my supervisor, Prof. Santabrata Das. I am deeply grateful for his unwavering support, insightful guidance, and constant encouragement throughout my PhD journey, dedicating so much time, effort, and expertise to guide me through this challenging yet rewarding journey. His mentorship has been invaluable to my growth as a researcher. I also want to acknowledge Mrs. Anupama Das, the compassion she carries is so admirable, she also used to cook delicious food for the whole group during the tough times of COVID-19, and later on as well.

I also thank my doctoral committee members, Prof. Debaprasad Maity (Chair), Prof. Sovan Chakraborty, and Prof. Sayan Chakrabarti for their time, thoughtful critiques, and encouragement. Their perspectives have greatly strengthened me and broadened my academic horizons. I can not thank them enough for supporting me very much in or out of the office in every way possible.

I also acknowledge the Department of Physics, IIT Guwahati, for providing all the resources and infrastructure for carrying out research. I also extend my thanks to all the HODs of the department for their support and guidance, Prof. Subhradip Ghosh, Prof. Perumal Alagarsamy, and Prof. Bosanta R. Boruah.

I would also like to thank some faculty members of the Department of Physics, IIT Guwahati, Dr. Charudatt Y. Kadolkar, Dr. Bibhas Ranjan Majhi, Dr. Meduri C Kumar, Prof. Subhaditya Bhattacharya, and Dr. Pankaj Mishra, with whom I have interacted, and not just talked about academia but also about Art, Music, Culture, History, and Technology, etc.

Now, I thank all the past members of the accretion physics group at the IIT Guwahati, Dr. Biplob Sarkar, Dr. Ramiz Aktar, Dr. Indu Kalpa Dihingia, Dr. Aneesha U. and Dr. Samik Mitra for their support, fruitful, and healthy discussions whenever I needed them. I also thank the current members of the group, Dr. Pradeep Kumar Yadav, Gargi Sen, Seshadri Majumdar, Camelia Jana, Amit Kumar, Sreetama Das Choudhary, Subhankar Patra, Surendra Mund, and Sandip Naskar, for all the discussions and lots of beautiful memories.

Throughout my doctoral journey at IIT Guwahati, I have been privileged to forge meaningful friendships and professional relationships that have enriched both my academic pursuits and personal growth. I extend my heartfelt gratitude to my dear friends who shared in the triumphs and tribulations of this transformative experience: Rajnandan (my pseudo-roommate and constant companion), Sampreet, Sourav, Sudeshna, Akhil, Akanshu, Mrinal, Roson, Shivam, and Rakhshanda. Together, we navigated the complexities of doctoral life, finding joy in countless moments of laughter and strength in mutual support during challenging times.

I am equally grateful to the remarkable individuals whose paths intersected with mine during this journey, each contributing to my intellectual and personal development through meaningful interactions, collaborative discussions, and shared experiences: Debabrata, Angana, Mandira, Prantik, Bhargabi, Golam, Partha, Pushpesh, Subhangi, Sahabub, Shashi Priya, Sumit, Suresh, Banashree, Esha, Lipika, Shantanu, Saraswati, Pooja Kumari, Pooja Gupta, Anterdipan, Himanshu Murari, Indrajit, Shalini, Subhankar Patra, Bhoomika, Swarup, Rajesh Karmakar, Narendra Kumar, Sumit Goswami, and Surojit Dolui, Nikita. The diverse perspectives and insights shared by this vibrant community of scholars have been invaluable to my growth as a researcher and individual. I am particularly proud to note that many of these exceptional colleagues have already successfully completed their doctoral degrees, serving as both inspiration and testament to the excellence fostered within our academic community. The camaraderie, intellectual stimulation, and unwavering support of these friends and colleagues have made my doctoral experience not merely an academic endeavour but a profoundly enriching human journey that I will cherish throughout my career.

I am deeply grateful to my cherished friends who have been steadfast companions since the inception of my higher studies: Mamta, Divya, Ankit Gupta, Sushila Mehra, and Jyoti. Their enduring friendship, unwavering encouragement, and continuous support have been instrumental throughout my academic journey, providing a foundation of stability and motivation that transcended geographical boundaries and temporal distances.

I wish to acknowledge my fellow boarders at Lohit Hostel, IIT Guwahati, who created a vibrant residential community that became my home away from home. The spirited participation in recreational activities—from cricket matches and football games to numerous other sporting and cultural events—provided essential respite from academic rigors and fostered a sense of camaraderie that extended far beyond the confines of our studies. These shared experiences on the playing fields and in common spaces contributed significantly to maintaining the work-life balance crucial for doctoral success, while building lasting friendships that transcended academic boundaries.

I extend my sincere gratitude to the Department of Physics and Astrophysics at the University of Delhi, where I completed my Master's degree, which served as the foundational launchpad for my journey into the captivating realm of astrophysical research. The rigorous academic curriculum and inspiring faculty mentorship during my Master's program ignited my passion for astrophysics and provided the essential theoretical framework that would later prove invaluable in my doctoral pursuits.

The main encouragements behind this effort came from my family. I am happy to acknowledge the debts to my family members for their unconditional support and encouragement to maintain the interest and enthusiasm for my research.

Abstract

Accretion onto black holes underpins some of the most luminous and energetic astrophysical systems, such as active galactic nuclei (AGN) and X-ray binaries (XRBs). In the accretion process, the potential energy of the accreting material gets converted into heat as a result of frictional and turbulent forces inside the accretion flow. In accretion physics, viscosity and thermal conduction are fundamental processes which govern the accretion properties around black holes. Viscosity is essential to transport the angular momentum because it allows matter to spiral inwards rather than maintain stable orbital trajectories. Thermal conduction enables the transfer of energy through heat flux. Furthermore, the presence of magnetic fields significantly influences the dynamics of accretion flows around black holes. Therefore, in this thesis, we present a semi-analytic investigation into the dynamics and structure of hot, relativistic, viscous, transonic, and magnetised accretion flows around rotating black holes. The study focuses on the interplay between viscosity, thermal conduction, and magnetic field to explore their role in shaping accretion physics and observational features, including shock wave formation in accretion flow.

The investigation begins with studying the viscous accretion flows where the α-viscosity parameter varies with radial distance. This approach is motivated by magnetohydrodynamic simulations suggesting that constant α assumptions are oversimplified. Using a relativistic equation of state and a pseudo-Kerr potential, the study reveals that radially varying viscosity parameters govern the properties of the accretion flow. Furthermore, viscosity also modifies the formation and properties of shock waves, which play a crucial role in producing high-energy radiation via inverse Comptonisation in the post-shock region. We identify the effective domain of the parameter space for standing shock spanned by energy and angular momentum of the flow, which is sensitive to the black hole spin and the viscosity parameters.

Following this, the role of thermal conduction is studied in weakly collisional ADAF-like flows, where radiative cooling processes are inefficient. Unlike earlier works that relied on self-similar solutions, this thesis presents global, shock-inclusive solutions that account for both thermal conduction and parametric cooling. We self-consistently solve the governing fluid equations to obtain the global transonic accretion solutions for a set of model parameters, namely energy, angular momentum, viscosity, conduction parameter and parametric cooling parameter. The presence of thermal conduction significantly alters

the accretion flow by pushing critical points outward and modifying shock properties. To our knowledge, for the first time, this study focuses on examining the shock properties, such as shock radius, compression ratio and shock strength regulated by the dissipation parameters, i.e., thermal conduction parameters, viscosity parameter, and parametric cooling. We show that shock-induced global accretion solutions persist for a wide range of model parameters and identify the boundary of the parameter space in the energy-angular momentum plane that admits standing shocks for different dissipation parameters. A critical conduction parameter is identified, beyond which shocks cease to exist, and its critical value is shown to depend on black hole spin and viscosity. This has important implications for understanding accretion in systems like Sgr A* and M87.

The study is further extended to include toroidal magnetic fields along with thermal conduction, synchrotron and bremsstrahlung cooling. This investigation demonstrates, depending on the model parameters, the magnetized accretion flow undergoes shock transitions and shock-induced global accretion solutions persist over a wide range of model parameters including the conduction parameter, plasma-β, and viscosity parameter. We find that the shock properties, such as shock radius, compression ratio, and shock strength, are regulated by thermal conduction, plasma-β, and viscosity parameter. Furthermore, we compute the critical conduction parameter, a threshold beyond which shock formation ceases to exist, and investigate its dependence on plasma-β and viscosity parameter for both weakly rotating and rapidly rotating black holes. Finally, we examine the spectral energy distribution (SED) of the accretion disk and observe that increased thermal conduction and magnetic field strength lead to enhanced luminous emission spectra from black hole sources.

In conclusion, this thesis offers a comprehensive and physically motivated framework for understanding relativistic accretion around rotating black holes by incorporating viscosity, thermal conduction, and magnetic fields. The work of this thesis is based on the papers listed below.

List of Publications

Publications in journals:

1. **Singh, M.**, & Das, S. (2024). "Properties of relativistic hot accretion flow around rotating black hole with radially varying viscosity." *Astrophysics and Space Science*, 369:1.* [1] DOI | arXiv
2. **Singh, M.**, & Das, S. (2025). "Role of thermal conduction in relativistic hot accretion flow around rotating black hole with shock." *Journal of Cosmology and Astroparticle Physics*, 2025(02), 068.* DOI | arXiv
3. **Singh, M.**, Jana, C., & Das, S. (2025). "Effect of thermal conduction on accretion shocks in relativistic magnetized flows around rotating black holes." *Journal of Cosmology and Astroparticle Physics*, JCAP05(2025)055.* DOI | arXiv
4. Jana, C., **Singh, M.**, Rakshit, S., & Das, S. (2025). "Study of mass outflows from magnetized accretion disks around rotating black holes with thermal conduction." *Journal of Cosmology and Astroparticle Physics*, JCAP10(2025)090. DOI | arXiv

In preparation:

1. Behaviour of accretion flow around rotating black holes with different disk heights and hybrid disk heights geometries.

Conferences/Workshops/Schools attended

- Hosted North East Meet of Astronomers (NEMA-VI), IIT Guwahati, Nov 2020 (Online)
- Attended International Workshop on Numerical Astrophysics, Ferdowsi University of Mashhad, Iran, July 2020 (Online)
- **Monu Singh**, S. Das, "Dissipative accretion flows around black holes with viscosity parameter α as a function of radial distance," NEMA-VIII, Manipur University, India, Nov 2020

---

[1] Publications marked with * will be included in the thesis.

- **Monu Singh**, S. Das, "Dissipative accretion flow around black holes with radially varying viscosity," 32nd Meeting of IAGRG, IISER Kolkata, India, 19–21 Dec 2022
- **Monu Singh**, S. Das, "Properties of relativistic hot accretion flow around rotating black hole with radially varying viscosity," RETCO-V, Indian Institute of Astrophysics, Kodaikanal, India, 3–5 Apr 2023
- Hosted 10th International Conference on Gravitation and Cosmology (ICGC 2023), IIT Guwahati, India, Dec 2023

Contents

List of Figures

List of Tables

Introduction 1

> `"...We lost the skyline, We stepped right off the map`
> `Drifted into black space, And let the clocks`
> `relapse..."`
>
> *Steven Wilson 'The Sky Moves Sideways'*

1.1 Accretion process

Accretion is a process in which plasma spirals around the compact object due to its extreme gravitational attraction. The journey of understanding the accretion process began with Hoyle & Lyttleton (1939), who studied the pressure-less accretion flow around a star. Later on, Bondi & Hoyle (1944) and Bondi (1952) worked on the spherical accretion solutions around a star without considering the inflowing matter's angular momentum and incorporated gas pressure in their investigation. In the real astrophysical context, matter possesses angular momentum, allowing the transfer of this angular momentum as inflowing matter traverses its journey around compact objects. Shakura & Sunyaev (1973) incorporated the angular momentum of the flow and its transport during the accretion of matter onto compact objects. During the accretion process, some part of the gravitation energy is converted to thermal energy, and the generated heat can be radiated away through radiation processes (Abramowicz & Fragile, 2013). The extraction of gravitational potential energy from matter which accretes onto a gravitating object is known to be the dominant source of power in several types of close binary systems, and is widely believed to provide the power supply in active galactic nuclei and quasars. The growing acknowledgement of the significance of accretion has coincided with the substantial advancement of observational methodologies in astronomy, particularly the utilisation of the full range of electromagnetic radiation from radio waves to X-rays and gamma rays. (Frank et al., 2002).

(a) M87

(b) Sgr A*

Figure 1.1: (a) The first image of a black hole at the core of the galaxy M87. Image provided by EHT in the press release dated April 10, 2019 (Event Horizon Telescope Collaboration et al., 2019). (b) The second image of a black hole in the heart of the Milky Way galaxy, known as Sgr A* was released by the EHT collaboration in May 2022 (Event Horizon Telescope Collaboration et al., 2022a).

Thus, the new role for gravity arises because accretion on to compact objects is a natural and powerful mechanism for producing high energy radiations. Some simple order-of-magnitude estimates will show how this works. For a compact object of mass M and radius R, the gravitational energy released by the accretion of a mass m on to its surface is given by,

$$\Delta E_{\rm acc} = \frac{GMm}{R}, \tag{1.1}$$

where G is the gravitation constant. If the accreting body is a neutron star with radius $R \sim 10$ km, mass $M \sim M_{\odot}$, $\Delta E_{\rm acc}$ yields as 10^{20} erg per accreted gram. We would expect this energy to be released eventually, mainly in the form of electromagnetic radiations. Hence, the accretion process acts as a power source. For comparison, examine the energy that can be derived from the mass m through nuclear fusion reaction. The maximum is achieved when, as is typically observed in astrophysics, the material is primarily hydrogen, with the predominant contribution arising from the burning of hydrogen into helium. This yields an energy release as,

$$\Delta E_{\rm nuc} = 0.007mc^2,$$

where c is the speed of light. We obtain about 6×10^{18} erg per gram or about one-twentieth of the accretion yield in this case. Consequently, the process of accretion has the potential to release greater amount of energy. The equation (1.1) can be re-written as,

$$L = \frac{GM\dot{m}}{R}, \tag{1.2}$$

where L denotes the luminosity of a compact source (such as a white dwarf, neutron star, or black hole), and $\dot{m}$ represents the accretion rate, defined as the mass accreting per unit time around the compact object. Using the Schwarzschild radius ($r_{\rm s} = 2GM/c^2$), the source's luminosity can be expressed as $L = 0.5\dot{m}c^2\,(r_{\rm s}/r) = \eta\dot{m}c^2$, where η is the efficiency of the accretion process, and its value is decided by based on the nature of compact sources. Equation (1.2) dictates that the luminosity is related to the ratio of the mass (M) and radius (R) of the compact star (white dwarf and neutron star) or the size of the innermost stable circular orbits ($r_{\rm isco}$) for black holes commonly known as the compactness (M/R) of the compact object. In accretion physics, the luminosity of sources is often defined in terms of Eddington luminosity ($L_{\rm edd}$). The $L_{\rm edd}$ represents the upper limit of luminosity that a star, accreting object, or other luminous astrophysical entity can attain when the outward force from radiation pressure counterbalances the inward gravitational attraction of surrounding matter. It establishes a maximum accretion rate, above which radiation pressure would surpass gravitational forces, preventing or expelling the incoming material. In mathematical terms, it can be written as (Frank et al., 2002),

$$L_{\rm edd} = \frac{4\pi G M m_{\rm p} c}{\sigma_{\rm T}}, \tag{1.3}$$

where $m_{\rm p}$ is the mass of the proton accreting around the compact object, and σ_T is the Thompson scattering cross-section. It is noteworthy to point out that the $L_{\rm edd}$ depends on the mass of the compact object M. Therefore, $L_{\rm edd}$ can be further simplified as

$$L_{\rm edd} \cong 1.38 \times 10^{38} \left(\frac{M}{M_\odot}\right) \text{erg s}^{-1}. \tag{1.4}$$

Equation (1.4) gives the upper estimate on the luminosity of a particular compact object. Like luminosity, we also measure the accretion rate ($\dot{m}$) in terms of the Eddington accretion rate ($\dot{M}_{\rm edd}$), which is written as

$$\dot{M}_{\rm edd} = \frac{L_{\rm edd}}{\eta c^2}. \tag{1.5}$$

The accretion rate ($\dot{m}$) and luminosity (L) are the two most important observables in accretion physics, which are commonly quantified in terms of Eddington units given by equations (1.4) and (1.5). Recent advances in observational capabilities have brought these theoretical considerations into sharp focus. The groundbreaking observations of M87* and Sagittarius A* reported by Event Horizon Telescope Collaboration et al. (2021, 2022b) have provided unprecedented views of accretion flows in the immediate vicinity of supermassive black holes, see Figure-1.1. For example EHT collaboration is successful in constraining the mass accretion rate for M87 and Sgr A*, which are $(3-20)\times10^{-4} M_\odot$ yr^{-1} (The Event Horizon Telescope Collaboration et al., 2021a) and $(5.2-9.5)\times10^{-9} M_\odot$ yr^{-1} (Event Horizon Telescope Collaboration et al., 2022c), respectively. Furthermore, they also estimated the black hole shadow size of M87 ($\sim 42\mu$as) (Event Horizon Telescope Collaboration et al., 2019) and Sgr A* ($\sim 52\mu$as) (Event Horizon Telescope Collaboration et al., 2022a).

1.2 Accretion disk models

Numerous models in the literature elucidate the structure of the accretion disk depending on the various frameworks. In the subsequent sections, we discuss several theoretical models pertinent to these studies.

Standard disk model

The standard disk model, also known as the classical model of the accretion flow, was proposed by Shakura & Sunyaev (1973) (SS73). The model's most significant achievement was predicting the characteristic temperature profile $T \propto r^{-3/4}$, which successfully explained multi-wavelength spectra of numerous accreting systems (Page & Thorne, 1974). In this model, the accretion flow is considered to be Keplerian, geometrically thin ($H/r << 1$, H is the disk height, and r is the radial distance) and optically thick. The relativistic model was also proposed by Novikov & Thorne (1973) with similar physical considerations. Through dimensional analysis, they parameterised the viscous stress ($\tau_{r\phi}$) as proportional to the total pressure (P) within the disk and is given by,

$$\tau_{r\phi} = \alpha P, \tag{1.6}$$

where α is the proportionality constant, which governs the angular momentum transport inside the disk. This formulation, also known as the "α-prescription", encapsulates all the complex, poorly understood microphysics of turbulent viscosity into a single parameter α. Equation (1.6) is written with the consideration that kinematic viscosity (ν), $\nu = \alpha C_s H$, where C_s is the local speed of sound, and H is disk height. The physical reasoning behind this approach is that turbulent eddies in the disk are limited in size by the disk height H and in velocity by the sound speed C_s. This model holds a historical landmark for proposing the mechanism for the transport of the angular momentum. The α-viscosity prescription enabled theoretical progress without requiring a complete understanding of the turbulent transport mechanisms—an approach that proved remarkably successful and continues to be widely used till today, despite later discoveries about the magnetorotational instability (MRI) (Balbus & Hawley, 1991) being the likely physical origin of disk turbulence. Furthermore, the model does not account for heat advection; that is, the heat generated is radiated away in the immediate vicinity. In mathematical terms, $Q^+ = Q^-$, where Q^+ represents the heat produced and Q^- denotes the cooling that occurs due to radiation. The SS73 model predicts a characteristic multi-temperature blackbody spectrum. Each annulus of the disk radiates approximately as a blackbody with temperature T. Notably, observational studies reveal that the typical temperature of the radiation frequently surpasses 10^9 K in instances involving both stellar-mass and supermassive black holes. However, this model provides a framework for understanding the thermal component of the X-ray emission from accreting neutron stars and black holes in binary systems (Melia & Misra, 1993; Esin et al., 1997).

Shapiro, Lightman and Eardley model (SLE)

The Shapiro, Lightman and Eardley model was motivated by observations of hard X-ray spectra from black hole candidates that could not be readily explained by the thermal emission from a standard thin disk (Shapiro et al., 1976). In accretion flow, the blob of mass accreting around the black is composed of both electrons and ions. At a significant distance away from the horizon, ions and electrons can maintain a single temperature by communicating via the Coulomb interaction. However, in the vicinity of the horizon, where the gravitational force is strong, ions and electrons fail to maintain a single temperature. As a result, ions and electrons might have their own temperatures, which is known as a two-temperature accretion flow. Taking into account the two temperature plasma, Shapiro, Lightman, and Eardley (1976) (Shapiro et al., 1976) proposed a model, in which, unlike the Shakura-Sunyaev disk, which is optically thick, the SLE model describes an optically thin flow, where radiation can escape freely without significant absorption or scattering. Despite being optically thin, the SLE model maintains the geometrically thin assumption ($H/r << 1$) of the standard model. Since electrons are lighter than ions, the electron's temperature is significantly lower than the ions. This accretion model additionally considers the Comptonization of soft photons by hot electrons, with temperatures potentially reaching up to 10^9 K. The SLE model was among the first attempts to construct a model for optically thin accretion flows, which would later inspire various radiatively inefficient accretion flow models developed in subsequent decades (Narayan & Yi, 1994, 1995; Esin et al., 1997). The SLE model does not account for the advection of energy with the flow, which becomes increasingly important at higher temperatures where radiative cooling becomes less efficient. The conceptual contrast between the Shakura-Sunyaev disk and the SLE model provided a foundation for understanding state transitions in black hole X-ray binaries, where systems appear to switch between soft (disk dominated) and hard (corona dominated) spectral states. However, it was soon recognised that the accreting plasma in this model exhibits thermally unstable characteristics (Piran, 1978).

Slim disk model

The slim disk model was introduced by Abramowicz et al. (1988). In this model, the accretion disk exhibits comparatively higher accretion rates relative to the classical model proposed by Shakura & Sunyaev (1973), and because of that, the importance of the radiation pressure comes into the picture. A key achievement of the slim disk model was predicting modified temperature profiles, with $T \propto r^{-1/2}$ replacing the standard $r^{-3/4}$ dependence at high accretion rates (Sądowski et al., 2011). This flatter temperature distribution successfully matched observations of X-ray sources and other super-Eddington systems (Mineshige et al., 2000; Kawaguchi, 2003). The geometrical pressure scale height also occurs on the higher side, i.e., $H/r \sim 0.1$. Furthermore, instead of being radiated away, a large portion of the energy produced by viscous dissipation is retained by the accreting matter because of its high optical depth. The most defining feature of slim disks is the incorporation of radial advection of energy. The thin disk model does not properly account for the transonic nature of the flow near the inner boundary, particularly around black holes where material must cross the sonic point smoothly (Abramowicz et al., 1988). Some fraction of the energy generated by viscous dissipation is carried inward with the flow rather than being radiated away locally. Unlike the thin disk model where radial velocities are assumed to be much smaller than the azimuthal velocity, slim disks incorporate significant radial velocities. It allows accretion rates to exceed the Eddington limit without violating energy conservation. Slim disks provide a framework for understanding super Eddington accretion processes and the associated observational phenomena. The measured luminosities of ultra luminous X-ray sources (ULXs) that are beyond the Eddington limit of a conventional stellar-mass black hole are explained by the Slim disks (Watarai et al., 2001; Vierdayanti et al., 2006; Ghosh & Rana, 2021). During certain outburst phases, stellar-mass black holes in binary systems may enter regimes where the accretion flow transitions to a slim disk configuration (Straub et al., 2011). Nevertheless, some fundamental theoretical concerns persist unresolved due to their intrinsic complexity. This pertains to the disk's stability under radiation pressure, the magnetic field's influence on energy transmission inside the disk, the potential production of a heated corona, and outflows (Czerny, 2019). When stars are disrupted by supermassive black holes, the resulting accretion flow can temporarily reach super-Eddington rates where slim disk physics becomes relevant (Coughlin & Begelman, 2014). Some extremely luminous quasars in the early universe may achieve their high luminosities through super-Eddington accretion described by slim disk models (Volonteri & Rees, 2005; Madau et al., 2014). As observational capabilities continue to improve, particularly in the X-ray and extreme ultraviolet bands, the slim disk model provides essential theoretical context for interpreting observations of high-luminosity accreting systems and understanding the physical processes that power these extraordinary cosmic engines (Ohsuga & Mineshige, 2011).

Advection-dominated accretion flow

The Advection-Dominated Accretion Flow (ADAF) model is used to characterise environments in which radiative cooling is inefficient and accretion rates are extremely low (Narayan & Yi (1994, 1995)). The ADAF model's primary achievement was solving the long standing puzzle of why many black hole systems appeared significantly underluminous compared to standard thin disk predictions. By incorporating separate electron and ion temperatures and demonstrating that advection could dominate over radiative cooling at low accretion rates, the model explained how most of the gravitational energy could be carried into the black hole rather than radiated away. The formal mathematical foundation of ADAFs was established in the mid-1990s through the pioneering work of Narayan & Yi (1994, 1995), though important conceptual groundwork had been laid earlier by researchers including Ichimaru (1977), Rees et al. (1982), and Narayan & Popham (1993). Many accreting black holes, including Sagittarius A* at the Galactic Centre, were observed to be dramatically underluminous relative to predictions from standard disk theory given their estimated accretion rates. Observations revealed hard X-ray spectra from many accreting systems that could not be readily explained by thermal emission from a standard thin disk (Melia & Misra, 1993). The two-temperature Shapiro-Lightman-Eardley (SLE) model offered insights into hot accretion flows but suffered from thermal instability. Similar to the SLE model, ADAFs maintain a two-temperature configuration where ions are substantially hotter than electrons ($T_\mathrm{i} >> T_\mathrm{e}$, where T_i and T_e are the ion and electron temperatures, respectively). This occurs because: viscous dissipation primarily heats the ions: while Coulomb collisions between ions and electrons are inefficient at transferring energy at low densities, electrons are responsible for most of the radiative cooling. X-ray binaries exhibited transitions between soft and hard spectral states that required a theoretical framework beyond the standard disk model. ADAF theory addressed these challenges by fundamentally reconsidering the energy transport mechanisms in accreting systems, particularly at low accretion rates. The ADAF is pivotal in explaining low-luminosity black hole systems and specific phases of accretion in both stellar-mass and supermassive black holes (Yuan & Narayan, 2014). A sizable portion of the energy that is viscously dissipated is not radiated away but rather stored as thermal energy in the gas and advected inward with the flow. In an ADAF, inefficient cooling results in the gas reaching extremely high temperatures, nearing the virial temperature, representing the equilibrium between gravitational potential energy and thermal energy. ADAFs are geometrically thick with $H/R \sim 0.5-1$, forming a quasi-spherical hot envelope rather than a thin disk, while remaining optically thin. Due to significant radial pressure support, the rotational velocity is notably sub- (sub-Keplerian is the flow where the angular velocity of the accreting matter is lower than local Keplerian angular velocity). As accretion rates increase, radiative cooling becomes more effective, leading to a transition of the accretion flow to a slim disk or thin-disk configuration (Esin et al., 1997). The sum of kinetic energy, potential energy, and enthalpy per unit mass is usually positive, suggesting that the gas is only marginally bound and susceptible to outflow formation (Tanaka & Menou, 2006). The ADAF model has been successfully applied to a wide range of astrophysical systems, e.g., Sagittarius A*: The supermassive black hole at the Galactic Center accretes at a very low rate relative to its Eddington limit and displays a spectral energy distribution consistent with ADAF predictions. Low-Luminosity AGNs (LLAGNs): Many galactic nuclei display radiatively inefficient characteristics well-described by ADAF models. The MHD simulations have shown that ADAFs naturally develop turbulence, outflows, and jets, with complex time-dependent behavior near the event horizon (Penna et al., 2010; Porth et al., 2019; Nathanail et al., 2020).

Two-component advective flow model (TCAF)

The TCAF model is another very successful accretion flow model based on the advection of energy in the accretion process developed by the Chakrabarti & Titarchuk (1995). This model is composed of the Keplerian and sub-Keplerian components, where Keplerian flow is sandwiched in between the sub-Keplerian flow regions. The TCAF model considers the existence of shock waves in the accretion flow because of the inherent transonic nature of the accretion flow (Fukue, 1987; Chakrabarti, 1989). By demonstrating how sub-Keplerian flows experience shock transitions due to centrifugal forces, the model created a self-consistent picture where the shock-heated post-shock region serves as the hot Compton cloud that upscatters soft photons from the Keplerian disk. This physical picture naturally explained the coexistence of thermal and non-thermal emission components observed in many black hole systems. The existence of the shock front is favoured by the second law of thermodynamics, which says that any physical system evolves towards a higher entropy state, where post-shock flow has higher entropy content than the pre-shock flow. The standing shock transition happens provided the Rankine-Hugoniot conditions (RHC) (Landau & Lifshitz, 1959) for the standing shock are favoured. However, the existence of shock waves is not universal but depends on the properties of flow, e.g., the energy of the flow, the angular momentum of the flow, viscosity parameters, and the heating and cooling mechanism acting within the disk. The post-shock flow, resulting from shock compression, becomes hot and dense, functioning as an effective boundary surrounding the black hole, referred to as the post-shock corona (or Compton corona, henceforth PSC). This PSC serves as a region where soft photons from the Keplerian disk undergo Compton reprocessing by hot electrons, resulting in the emission of hard X-ray radiation. Therefore, this model successfully explains both the soft and high-energy components of the observed emitted spectra (Chakrabarti & Titarchuk, 1995; Mandal & Chakrabarti, 2005). A scenario may arise in which RHC are not satisfied in the flow; in such a case, a stationary shock wave is not feasible, however shock modulation may occur. This shock oscillation may induce the quasi-periodic oscillations (QPOs) in the emiited radiation often observed from black hole candidates, also this model can explain the observed spectral properties of black hole candidates (Chakrabarti & Titarchuk, 1995; Chakrabarti & Manickam, 2000; Mandal & Chakrabarti, 2005; Nandi et al., 2012; Iyer et al., 2015; Das et al., 2021; Majumder et al., 2022; Nandi et al., 2024). TCAF explains various spectral states without requiring fundamentally different accretion models (Chakrabarti & Titarchuk, 1995).

The Two-Component Advective Flow (TCAF) model elegantly explains black hole spectral state transitions as a continuous evolution driven by changing accretion rates in its two components (Chakrabarti & Titarchuk, 1995; Chakrabarti, 1997). The ratio of mass accretion rates ($= \dot{m}_h/\dot{m}_d$, where $\dot{m}_h$ and $\dot{m}_d$ are the halo and disk accretion rates, respectively) between the halo and disk components determines the spectral state of the system. In the low hard state (LHS) (in the low hard state, X-ray luminosity is relatively lower and spectrum is dominated by hard-energy photons), sub-Keplerian flow dominance creates a strong CENBOL (CENtrifugal supported BOundary Layer generally known as PSC) region that efficiently Comptonizes minimal soft photons from a weak Keplerian disk. This produces a hard power-law spectrum (photon index $\sim 1.5-1.8$) with minimal thermal contribution (Chakrabarti & Mandal, 2006). As the system evolves toward intermediate states, the strengthening Keplerian disk provides more soft photons, partially cooling the CENBOL and generating shock oscillations that manifest as QPOs (Chakrabarti et al., 2008, 2009)). The spectrum becomes a balanced mixture of thermal and Comptonized emission. In the high soft state (HSS), Keplerian disk dominance produces abundant soft photons that effectively cool the CENBOL, creating a spectrum dominated by thermal emission with a weak, soft power-law tail (Debnath et al., 2010). At extremely high accretion rates, the very high state emerges with both components operating efficiently, producing strong thermal emission along with significant Comptonization (Mondal et al., 2014). The TCAF model naturally explains the hysteresis observed in hardness-intensity diagrams, as the Keplerian disk responds to accretion rate changes on the viscous timescale while the sub-Keplerian component adjusts almost immediately (Mandal & Chakrabarti, 2010; Ghosh et al., 2019). This framework has been successfully applied to interpret observations from numerous black hole binaries, providing constraints on black hole parameters and accretion physics (Debnath et al., 2014; Molla et al., 2016; Chatterjee et al., 2016; Molla et al., 2017; Shang et al., 2019; Jana et al., 2020). In conclusion, the mathematical formulation of TCAF incorporates transonic flow solutions, shock conditions, and radiative transfer equations to create a comprehensive model that has been successfully fitted to observations from numerous black hole systems, providing important constraints on black hole parameters and accretion physics(Debnath et al., 2014; Chatterjee et al., 2016; Das et al., 2021).

1.3 Advective accretion flow

Considering a steady, axisymmetric accretion flow in a non-relativistic regime, the conservation of mass, radial momentum, angular momentum, and energy are described by the following height integrated differential equations (Narayan & Yi, 1994; Chakrabarti, 1990a; Chakrabarti, 1996; Chakrabarti & Das, 2004; Das, 2007; Yuan & Narayan, 2014). We adopt the cylindrical polar coordinates (r, ϕ, z) system to illustrate the equations as,

$$\dot{M} = 2\pi\Sigma r v, \tag{1.7}$$

$$\upsilon\frac{d\upsilon}{dr}+\frac{1}{\rho}\frac{dP}{dr}+\frac{d\Phi_{\rm e}^{\rm eff}}{dr}=0, \tag{1.8}$$

$$\upsilon\frac{d\lambda}{dr}+\frac{1}{\Sigma r}\frac{d}{dr}(r^2W_{r\phi})=0, \tag{1.9}$$

$$\Sigma\upsilon T\frac{ds}{dr}=Q^+-Q^-, \tag{1.10}$$

where υ, P, ρ, λ, Σ , and $W_{r\phi}$ are the radial velocity, pressure, density, specific angular momentum of the flow, vertically integrated density (Matsumoto et al., 1984) and the viscous stress, respectively. Here, s and T are the entropy density and local temperature of the flow. Q^+ is the heat gained by the flow while accreting onto the central object, which includes viscous heating, heat transfer due to conduction, etc. Furthermore, Q^- defines the heat loss during the accretion via synchrotron and bremsstrahlung cooling mechanisms. $\Phi_{\rm e}^{\rm eff}$ is the effective potential (at the disk equatorial plane) around a black hole, which combines gravitational and centrifugal contributions in a rotating frame. Its form depends on the spacetime geometry (Schwarzschild or Kerr black hole) and the adopted gravitational theory. In Newtonian frameworks $\frac{d\Phi_{\rm e}^{\rm eff}}{dr}=(\Omega_{\rm k}^2-\Omega^2)r$, where Ω and $\Omega_{\rm k}$ $(=\sqrt{GM_{\rm BH}/r^3})$ are angular velocity and Keplerian angular velocity of the flow. For relativistic scenarios, pseudo-Newtonian potentials (e.g., Paczyński-Wiita potential for Schwarzschild black holes (Paczyńsky & Wiita, 1980) are often employed to approximate general relativistic effects.

In the context of accretion, energy dissipation denotes the conversion of energy, mostly kinetic or potential energy of the accreting material, into heat as a result of frictional or turbulent forces inside the accretion flow. This process is crucial in astrophysical accretion since it dictates the dynamics, structure, and observable characteristics of the accretion disk. At the heart of accretion physics, two fundamental transport processes are of the most importance, such as viscosity and thermal conduction. Viscosity is essential to transport angular momentum because it allows matter to spiral inward rather than maintain stable orbital trajectories. Shakura & Sunyaev (1973) gave the viscosity prescription in the study of accretion flow. They proposed the viscous stress ($W_{r\phi}$) inside the disk is proportional to the total pressure (W), i.e., $W_{r\phi}=\alpha W$, where α is the proportionality constant also known as the viscosity parameter. This α-prescription provided a simple yet powerful framework for modelling accretion disks. Earlier, it was suggested that the viscosity arises because of the turbulence inside the disk (Shakura & Sunyaev, 1973), however, how turbulence arise within the accretion disk was unclear. Later, Balbus & Hawley (1991) indicated that the turbulence in the accretion disk is seeded by the magnetic field through magneto-rotational instability (MRI). The MRI works in differentially rotating magnetized flows, where small perturbations are amplified by weak magnetic fields, causing turbulence and angular momentum transport. Since molecular viscosity is not enough to explain the observed accretion rates (Balbus & Hawley, 1998), this mechanism solved a long-standing problem in accretion disk theory. The viscosity parameter α was also considered to be a constant in earlier studies, reflecting the lack of a detailed understanding of the underlying turbulence. Later, it is realized in the various simulation studies that the α parameter can vary spatially and temporally (Matsumoto & Tajima, 1995; Hawley et al., 1995, 1996; Lyubarskii, 1997; Steinacker & Papaloizou, 2002; Sano et al., 2004; Fragile et al., 2007; Penna et al., 2010, 2012; Porth et al., 2019; Mitra et al., 2022). Despite these known limitations, the α-prescription remains invaluable for semi-analytical approaches to accretion flow modeling, as it encapsulates the complex microphysics of angular momentum transport into a single, tractable parameter while maintaining the essential physics of the accretion process.

In the scenario, where the central source accumulates matter at a low rate, the temperature and density profiles of the heated accreting matter correspond to those of a radiatively inefficient accretion flow (RIAF) due to its low radiative efficiency (Ichimaru (1977); Yuan & Narayan (2014)). In this context, the accreting plasma is anticipated to persist in a weakly collisional domain, with mean free pathways surpassing the average length scale of the accretion disk structure, which is equivalent to the gravitational radius. Consequently, thermal conduction gains dynamic significance, enabling the accreting matter to transfer energy through heat flux. Thermal conduction also greatly influences the thermodynamic structure and stability of accretion flows, relevant in both the classical and relativistic regimes (Tanaka & Menou, 2006; Mosallanezhad et al., 2021; Mitra et al., 2023). In the ADAF solutions, Tanaka & Menou (2006) recognised that thermal conduction within the accretion flow extracts the energy for the outflow and jets from the disk. Similar finding was also reported by researchers in the ADAF regime (Shadmehri, 2008; Bu et al., 2016).

Beyond thermal transport processes, the electromagnetic properties of the accreting plasma also play a crucial role in flow dynamics. The ubiquitous nature of the magnetic field in the universe plays a very interesting role in the dynamics of the accretion flow. The dissipation processes in accretion flows surrounding black holes are radically changed by magnetic fields, which power outflows and jets, induce turbulence, and allow reconnection (McKinney & Narayan, 2007; McKinney et al., 2012; Zamaninasab et al., 2014; Nathanail et al., 2020; Latif et al., 2023; Kenzhebayeva et al., 2024; Jiang et al., 2024). These fields govern the efficiency of flow in conveying angular momentum and transforming gravitational energy into heat and radiation. Consequently, they influence the discernible characteristics of accreting black holes, encompassing their spectral energy distribution, variability, and jet dynamics (King et al., 2007; Dihingia et al., 2020; Jiang et al., 2024). Comprehending magnetic field interactions in accretion flows is essential for analysing multiwavelength observations of black hole systems (You et al., 2023; Jiang et al., 2024). Blandford & Znajek (1977) proposed the idea that energy can be extracted from the spin of a rotating black hole via magnetic fields, facilitating the generation of the relativistic jets known as the Blandford-Znajek process. Balbus & Hawley (1991) recognised the significance of comprehending the magnetic field's role, demonstrating that a weak magnetic field within the accretion flow initiates turbulence in the disk, thereby modifying the physical mechanisms at play, such as angular momentum transport and energy distribution. This transport of angular momentum via magnetic field also modifies the viscosity parameter α, which is not a well-constrained quantity. King et al. (2007) (King et al., 2007) identified a notable disparity of around a factor of ~ 10 between observational and theoretical estimates of the viscosity parameter in accretion flow surrounding a black hole. Determining the value of α from both local and global simulations is undeniably complex, as it is influenced by various parameters, including the initial magnetic field geometry and strength (Sorathia et al., 2012). The magnetic field significantly affects the radiation process in accretion flow, especially synchrotron radiation, which correlates directly with the magnetic field; the greater the magnetic field strength, the more pronounced the synchrotron light emitted from the disk (Shapiro & Teukolsky, 1983; Rybicki & Lightman, 1986; Wardziński & Zdziarski, 2000). Furthermore, Magnetic fields also alter thermal conduction processes in accretion flows through several distinct mechanisms, primarily by introducing anisotropy in the transport coefficients and modifying the electron mean free path (Narayan & Yi, 1995; Ghasemnezhad, 2018). In the presence of a magnetic field, thermal conduction becomes highly anisotropic, with significantly different transport rates parallel and perpendicular to the field lines (Sharma et al., 2008; Mosallanezhad et al., 2022).

The accretion rate is also an important parameter that dictates the radiation and matter transport mechanisms in an accretion flow. An increased accretion rate results in greater energy availability for dissipation as heat, radiation, or outflows, such as winds and jets. In the standard disk model, the generated heat (Q^+) is equivalent to the cooling rate (Q^-), expressed as $Q^+ = Q^-$, indicating that $Q^+ \propto \dot{m}$. Thus, the accretion rate not only determines the total energy budget but also controls how much energy is dissipated and how it is distributed across radiation, heat, or mechanical energy. The balance between heating and cooling is established by the accretion rate $\dot{m}$, which in turn determines the accretion regime and affects the properties of the accretion flow. Radiatively inefficient accretion flows (RIAF), such as Advection-Dominated Accretion Flows (ADAFs), predominate at low accretion rates ($\dot{m} << \dot{M}_{\rm edd}$). A significant amount of the energy generated by viscous dissipation is retained in the gas and advected inward rather than radiated outward (Narayan & Yi, 1995). These flows are typically defined by geometrically thick and optically thin configurations, often displaying significant outflows or winds (Esin et al., 1997). At modest accretion speeds ($\dot{m} \sim \dot{M}_{\rm edd}$)., radiatively efficient flows, such as thin accretion disks, are prevalent. In this context, a substantial fraction of the dissipated energy is efficiently radiated away, resulting in geometrically thin and optically thick disks, where energy dissipation primarily occurs within the disk's mid-plane (Shakura & Sunyaev, 1973). The importance of radiation trapping in super-Eddington accretion ($\dot{m} > \dot{M}_{\rm edd}$) scenarios is due to higher optical depths, which lead to the formation of thin or thick disks. The luminosity may be able to exceed the Eddington limit in this regime because a sizable amount of the dissipated energy is either contained and transferred inward or produces powerful winds and outflows (Abramowicz et al., 1988). The physical structure and observable features of the accretion flow, as well as the system's energy output, are all determined by the accretion rate. Altogether, viscosity, thermal conduction, magnetic field strength, and accretion rate are the key physical processes which accommodate the transport of angular momentum, heat, radiation and matter, respectively. In addition, changes to one of the physical dissipation mechanisms can also affect the other transport processes. For example, an increment in viscosity increases the rate of the angular momentum transport, which causes matter to fall more quickly towards the horizon and alter the density profile.

Recently, Uttley & Malzac (2025) shows that a model where fluctuations propagate through the accretion disk at the viscous timescale can account for observed X-ray time delays in black hole accretion flows. The results obtained directly limit the viscous dissipation timeframe as a function of radius, offering empirical measurements of the variations in angular momentum transmission and energy dissipation across the disk. The polarimetric EHT measurements have been invaluable, as they impose limitations on the magnetic field configuration within the inner accretion flow (The Event Horizon Telescope Collaboration et al., 2021b). The observed ordered polarisation pattern indicates a regularly organised magnetic field structure at event horizon scales, limiting the extent of turbulent dissipation and endorsing scenarios in which large-scale magnetic fields prevail over smaller-scale turbulent fields in the innermost regions (Event Horizon Telescope Collaboration et al., 2024). In this thesis, we focus on the interplay between the above-mentioned dissipative processes in the relativistic regime.

1.4 Relativistic accretion flow

The consequences of Einstein's general relativity (GR) theory become important in accretion processes, known as relativistic accretion flows, near black holes. The dynamics of the inflowing matter and the outgoing radiation are shaped by relativistic processes such as spacetime curvature and frame-dragging, which take place in the strong gravitational field close to a black hole. In GR, the ISCO represents the closest orbit where matter can sustain in a stable orbit around a black hole. For a Schwarzschild (non-rotating) black hole, the ISCO is at $r_{ISCO} = 6GM/c^2$. For a rotating (Kerr) black hole, the ISCO moves closer to the event horizon depending on the spin. The horizon also shifts as well with the spin of the black holes. Furthermore, as the horizon shifts with spin, the radiations coming out of the accretion disk also get altered (Shafee et al., 2008). Therefore, general relativistic effects govern the dynamics of accretion flow around the black holes. To circumvent the intricate challenges of relativistic hydrodynamics, astrophysicists proposed a pseudo-Newtonian methodology, wherein a judiciously selected potential replaces the Newtonian potential. The properties of Schwarzschild black holes mimicked by the Tejeda & Rosswog (2013) and Paczyńsky & Wiita (PW80) (Paczyńsky & Wiita, 1980) pseudo-potential. PW80 potential is a highly effective concept utilized in the study of accretion flow surrounding non-rotating black holes (Abramowicz & Zurek, 1981; Chakrabarti, 1989; Chakrabarti & Titarchuk, 1995; Czerny & Elvis, 1987; Chakrabarti & Das, 2001; Hawley & Krolik, 2002; Chakrabarti & Das, 2004; Das, 2007; Shafee et al., 2008; Sarkar & Das, 2016; Dihingia et al., 2018b; Mitra et al., 2023). Nonetheless, as previously mentioned, the effects of spin are significant, and PW80 does not account for this spin effect. Subsequently, the pseudo-Kerr potential has been identified (Artemova et al., 1996; Chakrabarti & Khanna, 1992; Mukhopadhyay, 2002; Chakrabarti & Mondal, 2006; Ghosh & Mukhopadhyay, 2007; Dihingia et al., 2018a). These pseudo-potentials are calculated based on specific assumptions and bear with limitations in some scenarios of the accretion flow. Consequently, the consideration of a pseudo-potential necessitates a preliminary investigation. The disk height (H) is often determined by considering hydrostatic equilibrium in the vertical direction (z). Consequently, the alteration in space-time geometry from Schwarzschild black holes to Kerr or Kerr-like black holes required a modification in disk height. Novikov & Thorne (1973) and Riffert & Herold (1995) reported an adequate characterisation of the thin accretion disk structure surrounding Kerr black holes.

In another aspects, at the outer edges of the disk ($r_{\rm edge}$), the accretion flow is thermally non-relativistic ($k_{\rm B}T << m_{\rm e}c^2$, where $k_{\rm B}$ denotes the Boltzmann constant, T represents the flow's temperature, and $m_{\rm e}$ signifies the electron mass), indicating that the adiabatic index of the flow (Γ) approaches 5/3. As the flow progresses toward the horizon, its temperature increases significantly, approaching the virial temperature, and it becomes thermally relativistic ($k_{\rm B}T >> m_{\rm e}c^2$), with Γ attaining a value of 4/3. This effect of variable Γ was largely avoided in the earlier studies, but later it was realised that the value of Γ plays an important role in governing the properties of the flow (Popham & Gammie, 1998). Chattopadhyay & Ryu (2009) proposed a relativistic equation of state (REoS) that accommodates the variable character of the adiabatic index of the flow while maintaining simplicity.

Observational tests of relativistic effects in accretion flows have become increasingly sophisticated in recent years. The broad iron Kα emission line at 6.4 keV provides one of the most powerful probes of the inner accretion flow, as its profile is shaped by gravitational redshift, Doppler effects, and light bending near the black hole (Reynolds & Nowak, 2003; Miller, 2007). This line's high skewing permits measurements of black hole spin and limits on the inner radius of the accretion disk. More recently, resolved images of the shadow and photon ring around supermassive black holes in M87* and Sgr A* by direct imaging by the Event Horizon Telescope (EHT) have transformed our capacity to test relativistic accretion models (Event Horizon Telescope Collaboration et al., 2019, 2022a). These results explicitly establish the existence of a centre brightness depression compatible with the photon capture radius expected by GR. X-ray resonance mapping methods have further allowed the measurement of light travel time delays between direct and reflected emission components, therefore offering an independent probe of the accretion geometry in the strong gravity regime (Uttley et al., 2014; Kara et al., 2016). Another observational window into strong-field gravity is provided by quasi-periodic oscillations (QPOs) in the X-ray light curves of accreting black holes, which may also arise from relativistic factors, including Lense-Thirring precession. There aren't many studies that cover every facet of flow dissipation and the relativistic effect, which requires further detailed investigation in this direction (Ingram et al., 2016; Sreehari et al., 2020; Das et al., 2021; Majumder et al., 2022; Nandi et al., 2024; Aneesha et al., 2024).

1.5 Shock wave in accretion flow

The phenomenon of shock waves is very common in astrophysical scenarios, e.g., as stars traverse the interstellar medium (ISM), their stellar winds may engage with the ambient gas, resulting in the formation of bow shocks. These shocks generate a curved shock front in advance of the star, akin to the bow wave produced by a moving vessel. The James Webb Space Telescope has documented images of these astrophysical bow shocks, notably surrounding the young star in Herbig-Haro 211 (Raptis et al., 2025). The shock wave may also be present in the accretion flow. The flow initiates at the outer edge and, according to the transonic characteristics, the accretion flow must traverse a transonic point when its sonic state changes from subsonic to supersonic. Multiple transonic points may exist in the flow: one near the horizon, referred to as the inner critical point ($r_{\rm in}$), and another at a farther distance, known as the outer critical point ($r_{\rm out}$). These critical points are the acoustic horizons. Once the outer critical point is traversed by the flow, any disturbance in the flow cannot propagate to the remainder of the flow. During accretion, the centrifugal force and gravitational force operate in opposing directions. If these forces are comparable, they may effectively impede and significantly reduce the flow. Upon traversing $r_{\rm out}$, the flow transitions to a supersonic state; if gravitational and centrifugal forces are comparable, they effectively halt the flow, contingent upon the flow variables. Given that the flow is supersonic and has no communication, a matter accumulation becomes inevitable, potentially resulting in a discontinuous transition in density and other flow variables such as velocity and temperature, resulting in a shock transition. Such a shock wave occurs if the Rankine-Hugoniot shock conditions (RHCs) are satisfied (Landau & Lifshitz, 1959; Frank et al., 2002). The RHCs are the conservation of (a) mass flux (b) energy flux, and (c) momentum flux. At the shock, the density and temperature of the flow rise and the flow velocity decreases significantly. After the shock, the flow gains velocity and plunges into the black hole after passing the inner critical point ($r_{\rm in}$). These shock solutions in the accretion flow are also favoured by thermodynamics, where a subsonic branch has higher entropy than the supersonic branch; the system evolves towards a higher entropy state (Becker & Kazanas, 2001). Many semi-analytical (Fukue, 1987; Chakrabarti, 1989; Yang & Kafatos, 1995; Chakrabarti, 1996; Lu et al., 1999; Chakrabarti & Das, 2001; Becker & Kazanas, 2001; Chakrabarti & Das, 2004; Le & Becker, 2004; Fukumura & Tsuruta, 2004; Das, 2007; Becker et al., 2008; Das et al., 2009a; Kumar et al., 2013; Sarkar & Das, 2016; Aktar et al., 2017a; Dihingia et al., 2019a; Sen et al., 2022; Patra et al., 2022; Singh & Das, 2024; Jana & Das, 2024; Kumar et al., 2025) and simulation studies (Chakrabarti & Molteni, 1993; Molteni et al., 1996b; Ryu et al., 1997; Lanzafame et al., 1998; Giri et al., 2010; Das et al., 2014a; Okuda & Das, 2015; Suková & Janiuk, 2015; Suková et al., 2017; Kim et al., 2019; Okuda et al., 2019; Debnath et al., 2024a; TianLe-Zhao et al., 2024) confirm the existence of shocks in the accretion flow around black holes. In this thesis, we utilise the Rankine-Hugoniot shock conditions to determine the locations of shocks. The shock-induced accretion solution plays significant role in the examination of accretion phenomena surrounding black holes, as these solutions elucidate the hard-energy spectrum observed in black hole candidates. At the shock, the temperature of the flow increase and the post shock flow get puffed up and act as a region characterized by a swarm of hot electrons, referred to as the post-shock corona (PSC), where soft photons from the disk are inversely comptonized to generate hard-energy photons (Chakrabarti & Titarchuk, 1995). In this thesis, we focus on investigating the properties of shock-induced accretion solutions, including various dissipative processes in the relativistic regime.

1.6 Observational studies of black hole X-ray binaries

Observational studies have provided intriguing new information about the harsh cosmic settings, like black holes. The electromagnetic spectrum from black hole systems is primarily characterised by X-ray emissions, especially from the inner accretion disk, where temperatures exceed millions of degrees (Kanbach et al., 2001). Usually, the black hole X-ray binaries show different spectral states. In the high soft state (HSS), a thermal blackbody spectrum is detected, emanating from a geometrically thin, optically thick disk (Sharma et al., 2008; Mao & Yu, 2021; Zhu et al., 2023). Conversely, the low hard state (LHS) yields a power-law spectrum produced by a hot, optically thin corona (Melia & Misra, 1993; Cassatella et al., 2012; Marino et al., 2021; Yu et al., 2023). The transitions among these states yield significant insights into variations in accretion geometry (Esin et al., 1997; Mondal, 2023). The mechanisms facilitating transitions between spectral states continue to be a prominent focus of investigation. These transitions are thought to be associated with variations in the mass accretion rate; nevertheless, the overall situation is more intricate (Done et al., 2007). The truncated disk model proposes that state transitions arise from variations in the inner radius of the thin disk, with the disk approaching the black hole in the soft state and retracting in the hard state (Esin et al., 1997; Meyer et al., 2007). This state transition might be caused by the accumulation of the magnetic field (Begelman & Armitage (2014); Dexter & Begelman (2019)). The disk-corona coupling mechanism also affects transitions, as the characteristics of the corona vary significantly between states (Schnittman & Krolik, 2010). Recent models have emphasized the significance of radiative feedback between the disk and corona during transitions (Marcel et al., 2018a,b). The phenomenon of outflows and jets is often associated with state transitions, with jets being linked to the hard state and diminished during the soft state (Fender et al., 2004). Hysteresis effects, in which the change from hard to soft states occurs at a greater luminosity than the transition from soft to hard state, further complicate our comprehension of these processes (Maccarone & Coppi, 2003; Kylafis & Belloni, 2015). These transitions frequently align with particular categories of QPOs, indicating a basic relationship between alterations in accretion geometry and oscillatory dynamics in the flow (Ingram et al., 2016; Ingram & Motta, 2019).

The X-ray variabilities of the astrophysical sources are frequently observed. The power density spectrum (PDS) of the light curves is used to represent these variabilities in terms of QPOs. Black holes, neutron stars, ultra luminous X-ray sources (ULXs), and even active galactic nuclei (AGNs) have been found to exhibit QPOs, a remarkable signature of accreting compact sources (Belloni et al., 2007; Bachetti et al., 2014; Bonnet-Bidaud et al., 2015; Alston et al., 2016; Motta et al., 2017; Troyer et al., 2018; Ingram & Motta, 2019; Sreehari et al., 2020; Majumder et al., 2022; Nandi et al., 2024; Aneesha et al., 2024). QPOs are mainly divided into two categories: high-frequency QPOs (HFQPOs) and low-frequency QPOs (LFQPOs). LFQPOs generally has a frequency range of about 0.1 Hz to several tens of Hz (< 30 Hz), frequently linked to the precession of the inner accretion flow, disk instabilities, or general relativistic phenomena such as Lense-Thirring precession, which arises from the spacetime distortion caused by the black hole's rotation (Motta et al., 2017, 2018), and post shock corona (PSC) oscillations (Iyer et al., 2015; Debnath et al., 2024b; Singh et al., 2021; Das et al., 2021; Nandi et al., 2024). The LFQPO can be divided into three categories: Type-A, Type-B, and Type-C based on their frequencies, root-mean-square (RMS) amplitude, quality factor and their occurrence in spectral states (Ingram & Motta, 2019). In addition, Belloni et al. (2000) discovered classification of variable states for the black hole X-ray binary GRS 1915+105 into 15 different categories, which shows a range of quasi-periodic oscillations (QPOs) and spectrum transitions. Greek letter-based classifications have been developed for these fluctuating patterns: ρ, θ, α, β, etc (Athulya et al. (2022)). On the other hand HFQPO typically ranges from frequency > 30 Hz to few kilohertz. With numerous ideas explaining their occurrence and the characteristic 3:2 frequency ratio, HFQPOs in black hole X-ray binaries are probably tied to relativistic events in the accretion disk. Each of them provides understanding of the intricate dynamics of accretion disks around black holes: trapped inertial oscillations (Dewberry et al., 2020), Rossby wave instability (Varniere et al., 2020), epicyclic resonances (Huang et al., 2016), PSC oscillations (Aktar et al., 2018; Dihingia et al., 2019a,b; Majumder et al., 2022; Patra et al., 2024; Harikesh et al., 2025) and spinning hotspots (Wang et al., 2005). Furthermore, the shock-induced accretion flow model (TCAF) offers a compelling explanation for the spectro-temporal properties commonly observed in black hole candidates (Chakrabarti & Titarchuk, 1995; Chakrabarti & Manickam, 2000; Mandal & Chakrabarti, 2005; Nandi et al., 2012; Iyer et al., 2015; Das et al., 2021; Majumder et al., 2022; Nandi et al., 2024).

Apart from SMBHs and AGNs, there is another category of compact objects emitting in the X-ray regime known as ultraluminous X-ray sources. Ultraluminous X-ray Sources (ULXs) represent one of the most intriguing classes of high energy astrophysical objects, with luminosities exceeding 10^{39} erg/s, which corresponds to the Eddington limit for a stellar-mass black hole of approximately 10 solar mass (Kaaret et al., 2017). The extreme luminosities of ULXs require either intermediate mass black holes or super-Eddington accretion onto stellar mass compact objects (Poutanen et al., 2007). Super-Eddington accretion models have become increasingly sophisticated, incorporating the effects of radiation pressure, photon trapping, and geometrically thick disk structures. These models predict that super-Eddington flows should produce optically thick outflows that can carry away excess energy and angular momentum while allowing continued high rate accretion onto the central object. The slim disk model developed by Abramowicz et al. (1988) provided the first self-consistent framework for super-Eddington accretion, showing how photon trapping and advection could allow mass accretion rates far exceeding the Eddington rate while maintaining luminosities at or above the Eddington limit. Short term variability studies have revealed that many ULXs show significant flux variations on timescales of hundreds to thousands of seconds, with fractional variability amplitudes typically ranging from 10-50% (Heil et al., 2009). Several ULXs have been observed to exhibit quasi-periodic oscillations (QPOs), which provide powerful diagnostics of accretion flow properties and compact object mass (Das et al., 2021; Majumder et al., 2025). The discovery of QPOs in sources like M82 X-1 and NGC 5408 X-1, with frequencies around 0.1 Hz, initially suggested intermediate mass black holes with masses of several hundred to thousand solar masses (Strohmayer & Mushotzky, 2003). Recently, (Das et al., 2021) investigated the study on ULX source IC 342 X-1, and suggested that IC 342 X-1 is a rapidly rotating source and accretes matter at a super-Eddington accretion rate. Majumder et al. (2023) also investigated the ULXs. They discuss the detailed analysis of five ultraluminous X-ray sources (ULXs), namely NGC1313 X-1, NGC5408 X-1, NGC6946 X-1, M82 X-1, and IC342 X-1, likely containing black holes, utilizing archival

XMM-Newton observations. They also indicate that NGC6946 X-1 and NGC5408 X-1 might accrete at sub-Eddington accretion rate given that their central sources are rotating rapidly, whereas IC342 X-1 and NGC1313 X-1 can accrete in sub/super-Eddington limit irrespective to their spin values. Later on, Majumder et al. (2024) detected the polarisation in the Galactic ULX pulsar Swift J0243.6+6124 with the IXPE instrument. Recently, Majumder et al. (2025) also studied spectral evolution of eight black hole ultraluminous X-ray sources (BH-ULXs), namely NGC 1313 X-1, NGC 5408 X-1, NGC 6946 X-1, IC 342 X-1, NGC 55 ULX-1, NGC 4395 ULX-1, NGC 5204 X-1, and NGC 4190 ULX-1 using XMM–Newton.

1.7 Numerical studies of accretion flow

Hydrodynamics

The study of black hole accretion flows through numerical simulations has been driven by both observational discoveries and theoretical insights. Early observations of energetic phenomena associated with compact objects prompted the development of accretion disk theory (Shakura & Sunyaev, 1973), while more recent observations, such as those from the Event Horizon Telescope (Event Horizon Telescope Collaboration et al., 2019), have provided direct tests of numerical models. Similarly, theoretical breakthroughs like the identification of the magnetorotational instability (Balbus & Hawley, 1991) have fundamentally altered our understanding of accretion physics and required increasingly sophisticated simulation techniques. The earliest numerical studies of accretion flows employed hydrodynamic models that treated the accreting matter as a fluid without considering magnetic fields. Wilson (1972) performed pioneering numerical calculations of spherical accretion onto a black hole, building on the analytical work of Bondi (1952). These early simulations were primarily one-dimensional and utilised Newtonian physics, with simplified treatments of the gravitational potential. Hawley et al. (1984) developed the first two-dimensional hydrodynamic simulations of black hole accretion, using the ZEUS code to study thick accretion disks. These simulations revealed the formation of complex flow structures, including shocks and turbulence, that could not be captured by one-dimensional models. The use of the Paczynski-Wiita potential (Paczyńsky & Wiita, 1980) allowed these Newtonian simulations to approximate some general relativistic effects, particularly the presence of an innermost stable circular orbit (ISCO). As computational capabilities advanced through the 1990s, hydrodynamic simulations incorporated increasingly sophisticated numerical methods. The development of high-resolution shock capturing schemes, such as the Piecewise Parabolic Method (Colella & Woodward, 1984), allowed for more accurate treatment of the complex fluid dynamics in accretion flows. These methods were implemented in codes like ZEUS-2D (Stone & Norman, 1992) and later FLASH (Fryxell et al., 2000). Stone et al. (1999) performed detailed simulations of advection dominated accretion flows (ADAFs), a regime identified by Narayan & Yi (1994) where the energy released through viscous dissipation remains largely trapped in the flow rather than being radiated away. These simulations confirmed many of the properties predicted by analytical ADAF models and revealed additional complexities in the flow structure. The incorporation of radiation transport into hydrodynamic simulations represented another significant advance. Ohsuga et al. (2005) developed radiation hydrodynamic simulations that could model super-Eddington accretion flows, where radiation pressure becomes dynamically important. Their work demonstrated that radiation driven outflows could form naturally in high accretion rate systems, providing a potential explanation for observed winds in X-ray binaries.

Studies by Chakrabarti & Molteni (1993) and Molteni et al. (1994) focus specifically on the shock wave in the accretion flow around the black hole, considering the PW80 potential, and utilising the smooth particle hydrodynamics numerical technique. Consequently, there were many hydrodynamical simulation studies on the phenomenon of shock in the context of accretion flow, exploring the various aspects of accretion around black holes (Molteni et al., 1996b; Ryu et al., 1997; Lanzafame et al., 1998; Das et al., 2014a; Suková & Janiuk, 2015; Suková et al., 2017; Kim et al., 2019; Palit et al., 2019; Debnath et al., 2024a).

Magneto-hydrodynamics

The black hole accretion study was revolutionised by the work of Balbus & Hawley (1991), who identified the magnetorotational instability (MRI) as the physical mechanism responsible for angular momentum transport in accretion disks. The MRI operates in weakly magnetised, differentially rotating flows, causing small perturbations to grow exponentially and generate turbulence that efficiently transports angular momentum outward. Balbus & Hawley (1991) followed their analytical work with numerical simulations that confirmed the growth and saturation of the MRI in local models of accretion disks. These initial simulations used a shearing box approximation, a local representation of a small section of the disk, which allowed for a detailed study of the MRI physics without the computational expense of global simulations. Stone et al. (1996) extended this work with global magnetohydrodynamic (MHD) simulations that demonstrated how the MRI driven turbulence could operate throughout an accretion disk. These simulations showed that the effective viscosity generated by MRI turbulence was comparable to that estimated by the α parameter in earlier models, providing a physical basis for the phenomenological approach of Shakura & Sunyaev (1973). As computational resources expanded, researchers developed increasingly sophisticated global MHD simulations of black hole accretion. Hawley & Krolik (2001) performed three-dimensional MHD simulations that revealed how magnetic fields could alter the structure of the inner accretion flow, including modifications to the location of the effective inner disk edge relative to the ISCO predicted by purely hydrodynamic models. The development of more advanced numerical techniques was crucial for these simulations. The constrained transport method (Evans & Hawley, 1988) addressed the challenge of maintaining the divergence-free condition for magnetic fields ($\nabla . B = 0$, where B is the magnetic field), which is essential for physical accuracy but difficult to maintain numerically. Codes like ATHENA (Stone et al., 2008) incorporated these techniques along with higher-order spatial reconstruction methods and Riemann solvers to provide more accurate treatment of MHD phenomena. Global MHD simulations revealed complex interactions between the disk and corona. Miller & Stone (2000) showed how magnetic buoyancy could lead to the formation of a magnetically dominated corona above the disk, providing a potential explanation for the observed hard X-ray emission from accreting black hole systems. These simulations also demonstrated how magnetic fields could launch winds and outflows from the disk surface. Igumenshchev et al. (2003) showed how magnetic fields in the inner regions of an accretion flow could lead to the formation of a magnetically arrested disk (MAD), where the magnetic pressure becomes strong enough to partially suppress accretion. These MAD configurations were later found to be particularly efficient at producing powerful jets via the Blandford-Znajek process (Blandford & Znajek, 1977), which extracts rotational energy from the black hole itself. Despite these advances, MHD simulations in Newtonian or pseudo-Newtonian gravity could not fully capture the effects of strong gravity near the black hole event horizon. This limitation motivated the development of general relativistic MHD simulations.

General relativistic magnetohydrodynamics (GRMHD) represents the state of the art in black hole accretion modeling, incorporating both the strong gravity of general relativity and the magnetic processes essential for understanding angular momentum transport and outflow formation. The development of GRMHD codes required overcoming significant theoretical and computational challenges. A key breakthrough came with the formulation of GRMHD equations in a form suitable for numerical integration. The 3+1 formalism, which decomposes spacetime into spatial hypersurfaces evolving in time, provided a framework for adapting techniques from Newtonian MHD to the relativistic context. Gammie et al. (2003) developed the HARM (High Accuracy Relativistic Magnetohydrodynamics) code, one of the first to implement GRMHD in a form that could achieve stable evolution of accretion flows around black holes. De Villiers & Hawley (2003) used their GRMHD code to perform simulations of accretion onto rotating black holes, demonstrating how black hole spin could enhance jet power through the Blandford-Znajek process. Their work showed clear differences between accretion onto Schwarzschild and Kerr black holes, particularly in the efficiency of energy extraction and the structure of the resulting outflows. The development of GRMHD simulations accelerated in 2000s and 2010s with the introduction of several sophisticated codes. McKinney & Gammie (2004) extended the HARM code to study the dependence of jet efficiency on black hole spin, finding that rapidly rotating black holes could convert a significant fraction of accreted rest-mass energy into jet power. Tchekhovskoy et al. (2011) used the HARM3D code to perform high resolution simulations of magnetically arrested disks around spinning black holes. Their work demonstrated that these configurations could achieve energy extraction efficiencies exceeding 100% (relative to the rest mass energy of accreted material), confirming that energy was being extracted from the black hole's rotation via the Blandford-Znajek process. Other important GRMHD codes include BHAC (Porth et al., 2017), which implemented adaptive mesh refinement to provide higher resolution in regions of interest; KORAL (Sądowski et al., 2013), which incorporated radiation transport; and H-AMR (Liska et al., 2018), which utilized GPU acceleration to achieve unprecedented resolution in global simulations. Another significant advance has been the incorporation of general relativistic radiation transport. Sądowski et al. (2013) developed the first general relativistic radiation magnetohydrodynamic (GRRMHD) simulations, which could self-consistently model the effects of radiation pressure and radiative cooling on the dynamics of the accretion flow. The PLUTO (Mignone et al., 2007, 2012) is another code utilised for studying the phenomenon of accretion around compact objects. These simulations are particularly important for understanding high accretion rate systems, where radiation can significantly influence the flow structure. The shock wave in the accretion flow utilising the MHD approach has been found, and with the application on supermassive black hole SGR A* (TianLe-Zhao et al., 2024). A major milestone in the field came with the first image of a black hole shadow from the Event Horizon Telescope (EHT) collaboration (Event Horizon Telescope Collaboration et al., 2019). This observation of M87* provided a direct test of GRMHD simulations, which had predicted the general morphology of the observed emission ring.

1.8 Purpose of the thesis

In this thesis, We conduct theoretical explorations of dissipative, relativistic accretion flow around black holes. We begin with prescribing the viscosity parameter (α) which varies with the radial distance r as $\alpha(r) = \alpha_0 r^\theta$, where α_0 and θ are constant parameters which control the viscosity within the flow. We formulate the transonic accretion solutions around the black holes and the effects of viscosity parameters α_0 and θ. We also established the shock-induced accretion solutions. We see the variations of shock properties namely shock radius (r_s), compression ratio (R), and shock strength (S). Furthermore, we examine the ranges of energy and angular momentum of the flow that renders shocked solutions and its modifications with the change in θ. We also illustrate the correlation between the viscosity parameter α_0 and θ for shock-induced accretion solutions. Afterwards, we consider the effects of thermal conduction in advective, relativistic hot accretion flow around black holes. Due to an increase in thermal conduction, there is a corresponding rise in the temperature profile and pressure; thus, the transonic properties of the flow are affected by variations in the degree of thermal conduction within the flow. We also explore the influence of thermal conduction on the shock properties and the modifications in shock parameter space. We study the behaviour of the critical limit of thermal conduction parameter $\Phi_{\rm s}^{\rm cri}$ with viscosity parameter α, parametric cooling ($f_{\rm c}$) and the spin of the black hole ($a_{\rm s}$). Moreover, we further extend the study of accretion flow properties in the presence of thermal conduction, toroidal magnetic field, synchrotron and bremsstrahlung cooling. Here, we examine the connection among thermal conduction, viscosity, magnetic fields, and the cooling mechanisms in accretion flows surrounding black holes, particularly in the presence of shock. We also investigate the shock properties and their variations with model parameters, such as heat conduction, viscosity, and plasma-β. We demonstrate the spectral energy distribution (SED) and its alteration due to thermal conduction and magnetic field activity. This thesis comprises three working chapters, with a brief outline of each chapter presented in order of publication.

Chapter 2

In Chapter 2, we present the study of hot, relativistic, viscous, advective accretion flows around rotating black holes in the steady state with emphasis on the radial variation of viscosity parameter α prescribed in the functional form $\alpha(r) = \alpha_0 r^\theta$, where α_0 and θ are constant parameters. This $\alpha(r)$ presccribtion is motivated by the recent magnetohydrodynamic simulations, which suggest that α may vary radially and affects the dynamics and properties of the inflow matter. Addressing the influence of variable $\alpha(r)$ on transonic flows and the formation of shocks, we utilize a relativistic equation of state (REoS) (Chattopadhyay & Ryu, 2009) and a pseudo-Kerr potential (Dihingia et al., 2018a) to approximate black holes space time geometry. We take care of the cooling mechanism by means of synchrotron emission (Shapiro & Teukolsky, 1983).

This study reveals that accretion flows can pass through multiple transonic points known as critical points, with shock waves existing under suitable conditions, i.e., Rankine-Hugoniot (RH) conditions (Landau & Lifshitz, 1959) of standing shock. The post-shock region, known as the post-shock corona (PSC), is hot and dense, where soft photons are inversely Comptonized and produce high energy radiation. Shock properties, the shock radius (r_s), compression ratio (R), and shock strength (S) are calculated as functions of the viscosity exponent (θ), accretion rate ($\dot{m}$), and black hole spin (a_k).

We find that θ is a decisive parameter which governs the accretion flow dynamics for both non-rotating ($a_{\rm k} = 0$) and rapidly rotating ($a_{\rm k} = 0.99$) BHs. We observe that as viscosity increases with increasing θ, the rise in viscosity enhances angular momentum transport pushing the shock to move inward and reducing the size of the PSC. The existence of shocks is constrained to specific parameter spaces in the flow local energy ($\mathcal{E}$) and angular momentum (λ) plane, with the possibility of shocks to vanish as θ exceeds its critical limit. We compute the correlation between the two different viscosity parameters α_0 and the maximum value of θ which ensure the possiblity of shock-induced accretion solutions, i.e, θ^{max}. We further find that for rapidly rotating black holes ($a_{\rm k} = 0.99$), shocked solutions continue to exist for higher viscosity compared to slowly rotating ones ($a_{\rm k} = 0$).

Chapter 3

Advection dominated accretion flows (ADAFs) and geometrically thin, optically thick accretion disks were proposed in classical studies to explain the behaviour of accreting systems at low and high mass accretion rates. When the accreting plasma is weakly collisional, thermal conduction becomes important for radiatively inefficient accretion flows (RIAFs), which predominate at very low accretion rates (Narayan & Yi, 1994; Yuan & Narayan, 2014).

The structure of the accretion flow is changed by thermal conduction, which allows energy transport through heat flux. The impact of thermal conduction in initiating outflows, boosting wind energy flux, and altering the disk's density and temperature profiles has been investigated in earlier research (MacioŁek-Niedźwiecki et al., 1997; Tanaka & Menou, 2006; Johnson & Quataert, 2007; Ghanbari et al., 2009; Faghei, 2012, 2013; Ghasemnezhad, 2018; Ghoreyshi & Shadmehri, 2020; Rezgui et al., 2022; Nakamura et al., 2019; Mosallanezhad et al., 2021; Bambic et al., 2024). However, there are only very few studies that involve the transonic properties of the accretion flow around black holes, including the effect of thermal conduction (Mitra et al., 2023; Rezaie et al., 2025; Sarkar et al., 2025). Furthermore, due to the existence of multiple critical points, the flow can maximize entropy through shock waves, which are caused by centrifugal barriers in rotating accretion flows. Several spectro-temporal characteristics of black hole sources have been demonstrated using these shock-induced flows. Motivated by this, we examine how thermal conduction affects accretion processes that contain shocks surrounding rotating black holes. The dynamics of low angular momentum, viscous, and advective flows under the effects of parametric cooling and thermal conduction are examined in this work. This study specifically examines shock properties, such as shock radius ($r_{\rm s}$), compression ratio (R), and shock strength (S) as functions of dissipation parameters, such as viscosity parameter α, thermal conduction parameter (also known as saturation parameter) $\Phi_{\rm s}$, and cooling parameter f_c. Here, we use the semi-analytic approach to solve the fluid equations, and to mimic the space-time geometry of black holes, we use a pseudo-Kerr (Dihingia et al., 2018a) potential and a relativistic equation of state (REoS) (Chattopadhyay & Ryu, 2009).

This study identifies that the thermal conduction parameter $\Phi_{\rm s}$ pushes the critical points outward and alters the flow's general structure, and mostly impacting the accretion disk's outer regions. We find that increasing $\Phi_{\rm s}$ pushes the shock front outward due to enhanced thermal pressure, whereas cooling pulls it inward by lowering post-shock pressure. A critical saturation parameter $\Phi_{\rm s}^{\rm cri}$ is computed, beyond which shock ceases to exist. This critical parameter is seen to depend strongly on black hole spin ($a_{\rm k}$), with values ranging from approximately 0.029 for non-rotating black holes to 0.04 for rapidly rotating ones. Viscosity also influences shock formation, with higher α leading to smaller shock radii and lower thresholds for $\Phi_{\rm s}^{cri}$. The shock-induced accretion solutions, including thermal conduction, are found across a wide range of energy, angular momentum, viscosity, and dissipation parameters. These results suggest that thermal conduction plays a pivotal role in the dynamics of weakly collisional accretion systems, such as those observed in Sgr A* and M87, where energy transport through thermal conduction is significant (Tanaka & Menou, 2006; Shadmehri, 2008; Faghei, 2012, 2013; Khajenabi & Shadmehri, 2013a; Ghoreyshi & Shadmehri, 2020; Sarkar et al., 2025).

Chapter 4

In chapter 4, we examine the effects of thermal conduction in relativistic, magnetised, viscous, advective accretion flows surrounding rotating black holes, combining bremsstrahlung and synchrotron cooling mechanisms. In Chapter 3, we address the influence of thermal conduction in conjunction with viscosity and parametric cooling; this research necessitates additional exploration by incorporating a magnetic field and selecting comprehensive cooling mechanisms, specifically synchrotron and bremsstrahlung radiation, in lieu of parametric cooling. Here, we explore the interplay between thermal conduction, viscosity, magnetic field and the cooling mechanism in accretion flow around black holes. In doing so, We consider that accretion flow is threaded by toroidal magnetic fields surrounding a Kerr black hole (Sarkar & Das, 2016; Das & Sarkar, 2018; Dihingia et al., 2020; Jana & Das, 2024), with the gravitational field approximated using the pseudo-potential formulation (Dihingia et al., 2018a). In addition, we utilise a relativistic equation of state (REoS) that satisfactorily takes care of the thermodynamic variables of the accretion flow (Chattopadhyay & Ryu, 2009). We derive global transonic accretion solutions, demonstrating that shock characteristics, including shock radius ($r_{\rm s}$), compression ratio (R), and shock strength (S), are affected by the plasma-β, conduction parameter, and viscosity. This work estimates a limiting conduction value beyond which shock formation ceases. Furthermore, we investigate its correlation with other model parameters for both weakly and rapidly rotating black holes. The results demonstrate that higher thermal conduction and magnetic field augment the luminosity of emission spectra from black hole sources.

Properties of relativistic hot accretion flows around rotating black holes with radially varying viscosity 2

> *"...In questions of science, the authority of a thousand is not worth the humble reasoning of a single individual...."*
>
> *Galileo Galilei*

For almost five decades, the α-viscosity prescription, first presented by Shakura & Sunyaev (1973)), has been a pillar in accretion disk theory. In earlier studies, the α parameter was thought of as a constant parameter. However, increasing data from both numerical models and observation points to the spatially and temporally varying nature of α. Hawley et al. (1995) initially showed via magnetohydrodynamic (MHD) simulations that spatial and temporal fluctuations in α are generated by magnetorotational instability (MRI). Global simulations by Sorathia et al. (2012) indicated radial changes connected to magnetic field configurations. Many simulation studies also confirm the variable nature of α (Matsumoto & Tajima, 1995; Hawley et al., 1995, 1996; Lyubarskii, 1997; Steinacker & Papaloizou, 2002; Sano et al., 2004; Fragile et al., 2007; Penna et al., 2010, 2012; Porth et al., 2019; Mitra et al., 2022). Being motivated by this, in this Chapter, we investigate the properties of viscous, advective accretion flow with radially varying $\alpha(r)$ viscosity parameter around rotating BHs. In doing so, we adopt $\alpha = \alpha_0 r^\theta$, where r is the radial coordinate, α_0 and θ are the parameters which control viscosity across the flow. We consider the relativistic equation of state (REoS) (Chattopadhyay & Ryu, 2009) that addresses the thermal non-relativistic ($k_\mathrm{B}T << m_e c^2$) characteristics of the flow at the outer edge, as well as the thermal-relativistic ($k_\mathrm{B}T >> m_e c^2$) nature of the flow at the inner edge. We also consider a pseudo-Newtonian effective gravitational potential

---

The contents of this chapter are published in Singh & Das (2024) which dictates the space-time geometry around rotating BHs (Dihingia et al., 2018a). We utilize the synchrotron radiation mechanism (Shapiro & Teukolsky, 1983) to examine the cooling effects in the accretion flow. Considering all these, we calculate the global transonic accretion solutions (GTAS) by solving the fluid equations using the accretion model parameters. Moreover, we identify the requisite GTAS that admit standing shock transitions, and render the dependencies of the dynamical as well as thermodynamical flow variables on the model parameters. We observed that the viscosity exponent θ plays a decisive role in controlling the structure and dynamics of accretion flow. In addition, we investigate the shock properties, such as shock radius (r_s), compression ratio (R), and shock strength (S), respectively, and study how r_s, R and S depend on the viscosity (α) and accretion rate ($\dot{m}$). We also determine the range of flow energy ($\mathcal{E}$) and angular momentum (λ) that render shock-induced GTAS, and ascertain the domain of shock parameter space in $\lambda-\mathcal{E}$ plane. We find that such a parameter space is altered as the viscosity exponent (θ) is varied. Since θ plays pivotal role in deciding the accretion disk structure, it is important to explore the limiting value of the viscosity exponent ($\theta^{\rm max}$) beyond which shock solutions cease to exist. Accordingly, we put effort to estimate $\theta^{\rm max}$ and find that it profoundly depends on both BH spin ($a_{\rm k}$) and α_0.

2.1 Basic considerations and model equations

We consider the axisymmetric, steady state, height averaged viscous advective accretion disk around a rotating BH in the presence of synchrotron emission. We also assume that the accretion disk remains confined around the disk equatorial plane. We approximate the effect of gravity by adopting an effective pseudo-potential (Dihingia et al., 2018a) that satisfactorily delineates the spacetime wrapping due to rotating BH. The accretion process inside the disk is driven by the viscous stress ($W_{r\phi}$) and we consider $W_{r\phi} = -\alpha\Pi$, where Π denotes the vertically integrated pressure including ram pressure, and α, the viscosity parameter, is the dimensionless quantity that is assumed to vary with radial coordinate. Needless to mention that α absorbs all the detailed microphysics of the viscous processes. With these considerations, we express all the governing equations using $M_{\rm BH} = G = c = 1$, where $M_{\rm BH}$, G and c denote BH mass, gravitational constant and light speed, respectively. With this, we write the length in unit of $r_g = GM_{\rm BH}/c^2$, and accordingly, time and angular momentum are written in the unit of r_g/c and $r_g c$. Furthermore, we utilize the same unit system in the following Chapters as well.

Governing Equations

The basic fluid equations that describe the motion of the accreting matter inside the disk around a rotating BH are as follows:

(a) Conservation equation for radial momentum:

$$v\frac{dv}{dr}+\frac{1}{h\rho}\frac{dP}{dr}+\frac{d\Phi_{\rm e}^{\rm eff}}{dr}=0, \tag{2.1}$$

where v, P, ρ and h, denote the flow velocity, gas pressure, mass density and specific enthalphy, respectively. In addition, $\Phi_{\rm e}^{\rm eff}$ refers the effective potential of a rotating BH that mimics the spacetime geometry at the disk equatorial plane and is given by (Dihingia et al., 2018a),

$$\Phi_{\rm e}^{\rm eff}=1+\frac{1}{2}\ln\left[\frac{r\Delta}{a_{\rm k}^2(r+2)-4a_{\rm k}\lambda+r^3-\lambda^2(r-2)}\right], \tag{2.1a}$$

where λ is the specific angular momentum of the accreting matter, $a_{\rm k}$ denotes the BH spin, and $\Delta=r^2-2r+a_{\rm k}^2$.

(b) Mass conservation equation:

$$\dot{M}=2\pi v\Sigma\sqrt{\Delta}\,, \tag{2.2}$$

where $\dot{M}$ is the mass accretion rate. In this work, we do not consider the ejection of matter in the form of outflow/jets and hence, $\dot{M}$ is treated as global constant in absence of any mass loss from the disk. Moreover, we express the accretion rate in unit of Eddington accretion rate as $\dot{m}=\dot{M}/\dot{M}_{\rm Edd}$, where $\dot{M}_{\rm Edd}=1.44\times10^{17}\left(\frac{M_{\rm BH}}{M_\odot}\right)$ gm s^{-1}. Further, Σ is the vertically integrated surface mass density of the accreting matter (Matsumoto et al., 1984), and is written as $\Sigma=2\rho H$, where H refers the local disk half thickness expressed as (Riffert & Herold, 1995; Peitz & Appl, 1997),

$$H^2=\frac{Pr^3}{\rho\mathcal{F}},\ \mathcal{F}=\gamma_\phi^2\frac{(r^2+a_{\rm k}^2)^2+2\Delta a_{\rm k}^2}{(r^2+a_{\rm k}^2)^2-2\Delta a_{\rm k}^2},\ \gamma_\phi^2=\frac{1}{(1-\lambda\Omega)}\,.$$

Here, Ω $[=(2a_{\rm k}+\lambda(r-2))/(a_{\rm k}^2(r+2)-2a_{\rm k}\lambda+r^3)]$ denotes the angular velocity of the accreting matter.

(c) Conservation equation for azimuthal momentum:

$$v\frac{d\lambda}{dr}+\frac{1}{\Sigma r}\frac{d}{dr}(r^2W_{r\phi})=0, \tag{2.3}$$

where, we consider the $r\phi$ component of the viscous stress as $W_{r\phi}=-\alpha\Pi=-\alpha(W+\Sigma v^2)$ (Chakrabarti & Molteni, 1995; Chakrabarti & Das, 2004, and references therein). In equation (2.3), W denotes the vertically integrated pressure and Σ represents the vertically integrated mass density.

In this work, we consider radially varying viscosity parameter resembling power law distribution as

$$\alpha = A\left(\frac{r}{r_g}\right)^{\theta} = \alpha_0 r^{\theta}, \tag{2.3a}$$

where A, θ, and α_0 are regarded as constants all throughout the flow. Similar findings on the radial variation of viscosity parameter are also recently reported by the group of workers (Penna et al., 2012). Note that when $\theta \rightarrow 0$, we obtain globally constant viscosity parameter $\alpha = \alpha_0$, as in the case of 'α model' prescription (Shakura & Sunyaev, 1973).

(d) Equation for energy balance:

$$\Sigma \upsilon T\frac{ds}{dr} = \frac{\upsilon H}{\Gamma - 1}\left(\frac{dP}{dr} - \frac{\Gamma P}{\rho}\frac{d\rho}{dr}\right) = Q^{-} - Q^{+}. \tag{2.4}$$

In equation (2.4), T is the flow temperature, s is the specific entropy and and Γ is the adiabatic index. Moreover, during accretion, the heat gain and lost by the flow are denoted by Q^{+} and Q^{-}, respectively. Following Chakrabarti (1996) and Aktar et al. (2017b), we adopt the mixed shear stress prescription to obtain the viscous heating of the flow and is given by,

$$Q^{+} = -\alpha \rho H r\left(\frac{P}{\rho} + \upsilon^2\right)\frac{d\Omega}{dr}. \tag{2.5}$$

In general, the bremsstrahlung cooling process is regarded as the inefficient cooling process (Chattopadhyay & Chakrabarti, 2000). Hence, in this work, we consider energy loss due to synchrotron cooling only. The synchrotron emissivity of the convergent accretion flow is obtained as (Shapiro & Teukolsky, 1983),

$$Q^{-} = Q^{\rm syn} = \frac{16}{3}\frac{e^2}{c}\left(\frac{eB}{m_e c}\right)^2\left(\frac{k_B T}{m_e c^2}\right)^2 n_e \quad {\rm erg\ cm^{-3}\ s^{-1}}, \tag{2.6}$$

where e, m_e, and n_e are the charge, mass, and number density of the electrons, respectively, k_B is the Boltzmann constant, B is the magnetic fields. In the astrophysical context, the presence of magnetic fields is ubiquitous inside the accretion disk, and hence, the ionised flow should emit synchrotron photons, causing the flow to cool down significantly. Indeed, the characteristics of structured magnetic fields inside the disk still remain unclear, and hence, we rely on the random or stochastic magnetic field. For the purpose of simplicity, we utilise the equipartition to estimate the magnetic field and obtain this as $B = \sqrt{8\pi\beta P}$, where β is a dimensionless constant (Das, 2007). Evidently, $\beta \lesssim 1$ confirms that the magnetic fields remain confined within accretion disk (Mandal & Chakrabarti, 2005). For the sake of representation, in this work, we choose $\beta = 0.1$.

To close the equations (2.1 - 2.4), one requires to consider an equation of state (EoS) that relates P, ρ and internal energy (ϵ) of the flow. Hence, we consider an EoS for relativistic flow which is given by (Chattopadhyay & Ryu, 2009),

$$\epsilon = \frac{\rho f}{\left(1+\frac{m_p}{m_e}\right)}, \tag{2.7}$$

with

$$f = \left[1+\Theta\left(\frac{9\Theta+3}{3\Theta+2}\right)\right] + \left[\frac{m_p}{m_e}+\Theta\left(\frac{9\Theta m_e+3m_p}{3\Theta m_e+2m_p}\right)\right],$$

where Θ $(= k_B T/m_e c^2)$ is the dimensionless temperature of the flow. Utilizing the relativistic EoS, we express polytropic index as $N = \frac{1}{2}\frac{df}{d\Theta}$, adiabatic index as $\Gamma = 1 + 1/N$ and sound speed as $C_s^2 = \frac{\Gamma P}{e+P} = \frac{2\Gamma\,\Theta}{f+2\Theta}$, respectively (Chattopadhyay & Ryu, 2009; Dihingia et al., 2018a). Further, following Chattopadhyay & Kumar (2016) and with the help of equation (2.2), we compute the entropy accretion rate as $\dot{\mathcal{M}} = vH\sqrt{\Delta}\left[\Theta^2\left(2+3\Theta\right)\left(3\Theta+2m_p/m_e\right)\right]^{3/4}\exp(k_1)$, where $k_1 = 0.5\times[f/\Theta-(1+m_p/m_e)/\Theta]$.

Using equations (2.1-2.7), we get the radial velocity gradient in the form of wind equation as,

$$\frac{dv}{dr} = \frac{\mathcal{N}(r, v, \Theta, \lambda, \alpha)}{\mathcal{D}(r, v, \Theta, \lambda, \alpha)}, \tag{2.8}$$

where both $\mathcal{N}$ and $\mathcal{D}$ depend on $r, v, \Theta, \lambda, \alpha$, and their explicit mathematical expressions are given in Appendix A. Using equation (2.8), we obtain the radial derivatives of angular momentum (λ) and dimensionless temperature (Θ) as,

$$\frac{d\lambda}{dr} = \lambda_1 + \lambda_2\frac{dv}{dr}, \tag{2.9}$$

and

$$\frac{d\Theta}{dr} = \Theta_1 + \Theta_2\frac{dv}{dr}, \tag{2.10}$$

where the mathematical form of the coefficients, such as λ_1, λ_2, Θ_1, and Θ_2 are described in Appendix-A.

2.2 Critical point analysis

Indeed, during accretion, the subsonic flow starts to accrete towards the BH from a far away distance $r_{\rm edge}$ (hereafter disk outer edge) and crosses the BH horizon (r_h) supersonically. Therefore, the flow must pass through a critical point (r_c) where a smooth transition occurs from the subsonic to supersonic domain. Due to the inherently transonic nature of black hole accretion, the flow must pass through the critical point (r_c). Hence, we employ r_c as reference radius $(r_{\rm ref})$ and supply angular momentum (λ_c) at r_c as local flow parameter for the chosen values of viscosity parameters α_0, θ, BH spin $(a_{\rm k})$, and accretion rate $\dot{m}$ which are considered as the global flow parameters. In a region $r > r_h$, the flow may posses multiple critical points depending on the model parameters. Following Chakrabarti & Das (2004), we perform the critical point analysis, where $\left(\frac{dv}{dr}\right)_{r_c} = \frac{0}{0}$ as one

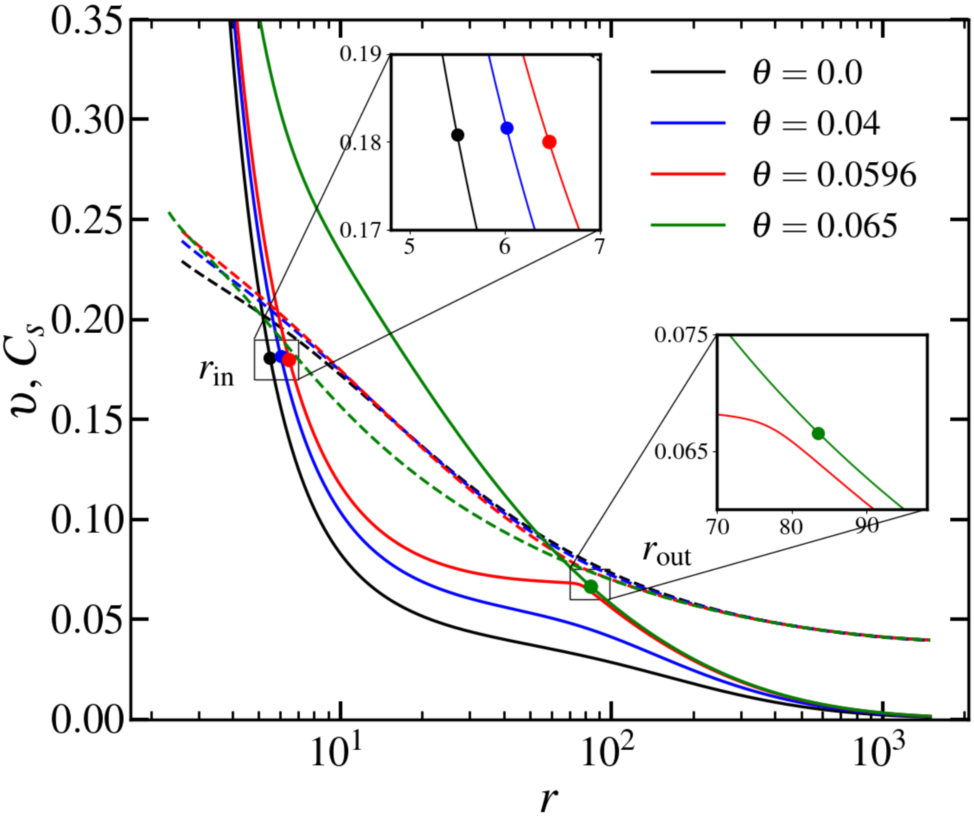

Figure 2.1: Illustration of flow velocity (υ) and sound speed (C_s) with radial distance (r) for various values of θ. Dashed curves indicate the sound speed and solid curves denote flow velocity. See the text for details.

gets $\mathcal{N} = \mathcal{D} = 0$ at the critical point. Due to this, we employ of the l´Hospital rule while calculating $\left(\frac{dv}{dr}\right)$ at r_c. For physically acceptable solutions around BH, we only consider saddle type critical points where $\left(\frac{dv}{dr}\right)$ furnish two distinct real values at the critical point (Das, 2007, and references therein). When r_c occurs near r_h, we identify it as inner critical point (r_{in}), otherwise it is named outer critical point (r_{out}) (Chakrabarti & Das, 2004).

2.3 Global transonic accretion solutions (GTAS)

The global transonic accretion solutions (GTAS) are obtained by solving the coupled differential equations (2.8 - 2.10) for a set of model parameters. Some of these parameters, namely α_0, θ, $\dot{m}$ and a_{k} remain constant all throughout called as global parameters, while critical point r_c and angular momentum λ_c at r_c are treated as local parameters. Employing these model parameters, we first integrate equations (2.8-2.10) starting from r_c upto r_h and again from r_c to r_{edge} (~ 1500). Thereafter, a complete GTAS around BH is obtained by joining both parts of the solutions. Depending on the set of the model

Table 2.1: Power law exponent (θ), critical point location ($r_{\rm c}$), critical point angular momentum ($\lambda_{\rm c}$), critical point velocity ($\upsilon_{\rm c}$), critical point temperature ($\Theta_{\rm c}$), disk outer edge ($r_{\rm edge}$), angular momentum at $r_{\rm edge}$ ($\lambda_{\rm edge}$), velocity at $r_{\rm edge}$ ($\upsilon_{\rm edge}$), temperature at $r_{\rm edge}$ ($\Theta_{\rm edge}$) for global transonic solutions presented in Figure 2.1. See the text for more details.

θ	$r_{\rm c}$ (r_g)	$\lambda_{\rm c}$ ($r_g c$)	$\upsilon_{\rm c}$ (c)	$\Theta_{\rm c}$ ($m_e c^2/k_{\rm B}$)	$r_{\rm edge}$ (r_g)	$\lambda_{\rm edge}$ ($r_g c$)	$\upsilon_{\rm edge}$ (c)	$\Theta_{\rm edge}$ ($m_e c^2/k_{\rm B}$)
0	5.50	3.15	0.1808	27.9476	1500.0	21.10	0.00089	0.98115
0.04	6.019	3.03	0.1816	28.2146	1500.0	21.10	0.00118	0.98106
0.0596	6.464	2.96	0.1800	27.6714	1500.0	21.10	0.00137	0.98099
0.065	83.488	2.83	0.0665	3.4779	1500.0	21.10	0.00140	0.98098

Note: Suffix 'c' denotes quantities measured at critical point ($r_{\rm in}$ or $r_{\rm out}$).

parameters, flow becomes transonic either at r_{in} or at r_{out} before plunging into the BH.

Figure (2.1) illustrates the typical sets of global transonic accretion solutions (GTAS) for flows injected from $r_{\rm edge} = 1500$ for various values of θ. Following the methodology mentioned in Das (2007), we calculate the accretion solution harbouring the inner critical point $r_{\rm in} = 5.50$, where we fix $\lambda_{\rm in} = 3.15$, $\alpha_0 = 0.01$, $\theta = 0.0$, $a_{\rm k} = 0.0$, and $\dot{m} = 0.01$. This renders a global accretion solution as it successfully connects the BH horizon r_h with $r_{\rm edge}$. Afterwards, we note the flow variables at $r_{\rm edge}$ as $\lambda_{\rm edge} = 21.10$, $\upsilon_{\rm edge} = 8.9 \times 10^{-4}$, and $\Theta_{\rm edge} = 0.98115$. In reality, we must get the same accretion solution once the flow equations are integrated towards BH horizon using these noted boundary values. Here, black solid curve represents the radial velocity υ, and black dashed curves represent the sound speed C_s of the flow for $\theta = 0.0$.

Next, we increase $\theta = 0.04$ while other flow variables remain the same at $r_{\rm edge}$ and calculate GTAS by suitably tuning $\upsilon_{\rm edge} = 1.18 \times 10^{-3}$, and $\Theta_{\rm edge} = 0.98106$. Here, we additionally require the boundary values of $\upsilon_{\rm edge}$ and $\Theta_{\rm edge}$ to integrate the fluid equations from $r_{\rm edge}$, as critical point remains unknown. The trajectory is denoted using blue color, where we observe that the inner critical point is shifted outward as $r_{\rm in} = 6.019$ for $\theta = 0.04$. Similarly, for $\theta = 0.0596$, flow solution (red) continues to maintain similar behaviour as in the cases of $\theta = 0.0$ and 0.04, rendering inner critical points at $r_{\rm in} = 6.464$. Solutions of this type that are passing through $r_{\rm in}$ are similar to ADAF-type accretion solutions (Narayan & Yi, 1994). However, when θ is increased further, the nature of the flow solution (in green) changes and becomes transonic at the outer critical point $r_{\rm out} = 83.488$ rather than $r_{\rm in}$. Usually, the solutions containing $r_{\rm out}$ are of Bondi type (Bondi, 1952). To ensure clarity, the regions around the critical points ($r_{\rm in}$ and $r_{\rm out}$) are zoomed in, which are indicated using filled circles in the insets. We tabulate the flow variables at $r_{\rm edge}$, $r_{\rm out}$, and $r_{\rm in}$ in Table 2.1. In general, we observe that the role of θ is crucial to deciding the characteristic of GTAS around the BH.

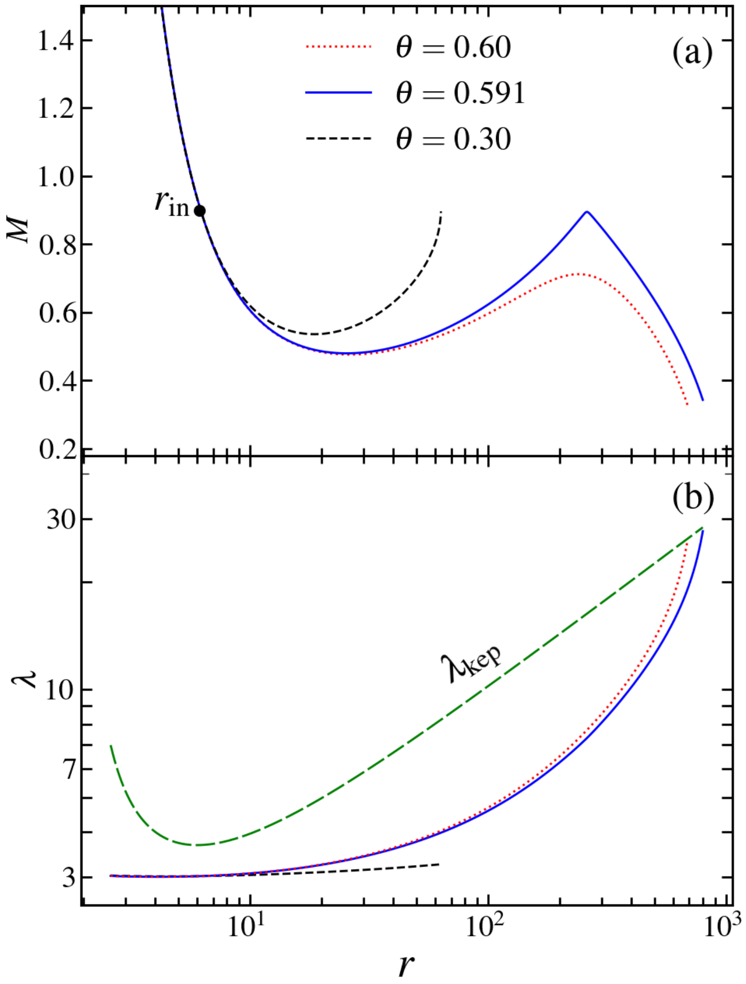

Figure 2.2: Plots of (a) Mach number M $(= v/C_s)$ and (b) angular momentum (λ) with the radial distance r for different θ values. Here, we fix $r_{\rm in} = 6.17$, $\lambda_{\rm in} = 3.01$, $\alpha_0 = 0.01$, and $\dot{m} = 0.01$. Dashed, solid and dotted curves denote results for $\theta = 0.30, 0.591$, and 0.60, respectively. See the text for details.

Subsequently, we demonstrate the accretion flow solutions in Figure (2.2a), depicting the radial change of the Mach number $(M = v/C_s)$. Here, all the solutions become transonic at $r_{\rm in} = 6.17$ with $\lambda_{\rm in} = 3.01$, $\alpha_0 = 0.01$, $\dot{m} = 0.01$, $a_{\rm k} = 0.0$, respectively. For $\theta = 0.60$, we obtain a GTAS that smoothly joins the BH horizon with $r_{\rm edge}$ where flow angular momentum matches with its Keplerian value as shown in the dotted curve. We gradually decrease θ and see that beyond the limiting value, as $\theta = 0.591$, the accretion solution becomes closed as depicted using the solid (blue) curve. The result drawn for $\theta = 0.3$ is shown using the dashed (black) curve. The closed accretion solutions pass through $r_{\rm in}$ are significant as they can join with another solution passing through

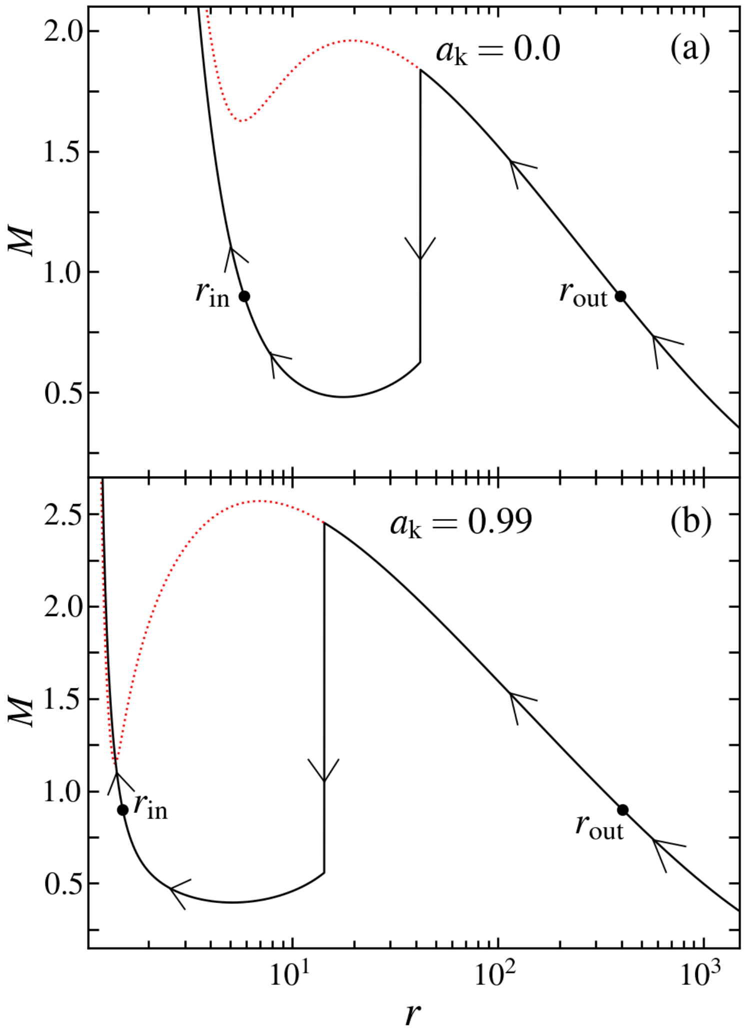

Figure 2.3: An illustration of the shock-induced global transonic accretion solution around BH, where variation of M with r is shown. Vertical down arrow represents the location of shock transition, where Rankine-Hogoniot conditions (Landau & Lifshitz, 1959) for standing shock are satisfied. Filled circles depict critical points, and arrows show the direction of the flow motion towards BH. Dotted curve represents shock free solution. (a) Upper panel is for $a_k = 0.0$, and (b) lower panel is for $a_k = 0.99$. See the text for details.

r_{out} via centrifugally supported shocks. The shock solutions are important since such solutions successfully represent both the temporal evolution and spectral properties of black hole sources. Shock formation in advective accretion flows yields important physical implications (Molteni et al., 1994, 1996a; Chakrabarti & Titarchuk, 1995; Chakrabarti, 1996; Lu et al., 1999; Chakrabarti & Manickam, 2000; Das et al., 2009b; Nagakura & Yamada, 2009; Nandi et al., 2012; Iyer et al., 2015; Okuda & Das, 2015; Suková & Janiuk, 2015; Das et al., 2021). Accordingly, in the next section, we investigate the shock-induced

Table 2.2: Black hole spin ($a_{\rm k}$), critical point location ($r_{\rm c}$), angular momentum ($\lambda_{\rm c}$), radial velocity ($\upsilon_{\rm c}$), and temperature ($\Theta_{\rm c}$) measured at $r_{\rm c}$ for shocked accretion solution presented in figure 2.3. Subscript 'c' refers the quantities measured either at the inner ($r_{\rm in}$) or outer ($r_{\rm out}$) critical point. See the text for details.

$a_{\rm k}$	Critical Point	$r_{\rm c}$ (r_g)	$\lambda_{\rm c}$ ($r_g c$)	$\upsilon_{\rm c}$ (c)	$\Theta_{\rm c}$ ($m_e c^2/k_B$)
0	Inner	5.808	3.091	0.1794	27.4538
	Outer	395.32	3.470	0.0313	0.7580
0.99	Inner	1.492	2.058	0.2653	68.1666
	Outer	405.46	2.445	0.0312	0.7510

GTAS around BHs. In Figure (2.2b), we show the variation of angular momentum for the solutions presented in Figure (2.2a), where big-dashed curve represents the Keplerian angular momentum profile.

In Figure (2.3), we illustrate an example of the shock-induced global accretion solution, which passes through both $r_{\rm out} = 395.32$ and $r_{\rm in} = 5.808$ while accreting onto a non-rotating BH ($a_{\rm k} = 0.0$) and rapidly rotating BH ($a_{\rm k} = 0.99$). Here, matter is injected sub-sonically from $r_{\rm edge} = 1500$ with $\lambda_{\rm edge} = 4.68$, $\upsilon_{\rm edge} = 8.35 \times 10^{-3}$, $\Theta_{\rm edge} = 0.336$, $\dot{m} = 0.01$, $\alpha_0 = 0.01$, and $\theta = 0.1$. As subsonic matter traverses its journey towards the BH, it crosses the outer critical point at $r_{\rm out} = 395.32$ and becomes supersonic, and continues its motion towards the BH. Infalling matter may continue unimpeded across the BH horizon beyond $r_{\rm out}$, as illustrated by the dotted (red) curve. Conversely, supersonic flow presents an alternative scenario wherein flow variables undergo shock transitions to the subsonic regime, provided the Rankine-Hugoniot conditions (RHCs) (Landau & Lifshitz, 1959) for stationary shocks are fulfilled at the shock radius ($r_{\rm s}$). For the mentioned flow parameters, we compute the standing shock radius at $r_s = 42.07$ for a vertically integrated flow by employing shock conditions (RHCs) which are (a) conservation of energy flux: $[\mathcal{E}] = 0$, (b) conservation of mass flux: $[\dot{M}] = 0$, and (c) conservation of momentum flux $[W + \Sigma \upsilon^2] = 0$ across shock. Here, we express the local energy of the flow as $\mathcal{E} = \upsilon^2/2 + \log h + \Phi_{\rm e}^{\rm eff}$, and the quantities within the bracket ([ ]) denote their differences across shock transition location. We depict the shock transition using the vertical arrow. After shock transition, the radial velocity of the matter decreases; however, it progressively increases as the matter approaches the horizon. Eventually, matter reaches the BH horizon at supersonic speed after passing through the inner critical point at $r_{in} = 5.808$. In the figure, arrows show the direction of the flow towards BH. Note that the post-shock branch of the shocked solution is similar in nature to the solution for $\theta = 0.3$ in Figure 2.2. Furthermore, we calculate the shock-induced GTAS around a rotating BH of $a_{\rm k} = 0.99$ for flows injected with $\lambda_{\rm edge} = 3.68$, $\upsilon_{\rm edge} = 8.33 \times 10^{-3}$, $\Theta_{\rm edge} = 0.342$, $\dot{m} = 0.01$, $\alpha_0 = 0.01$, and $\theta = 0.1$ from $r_{\rm edge} = 1500$. The shock front

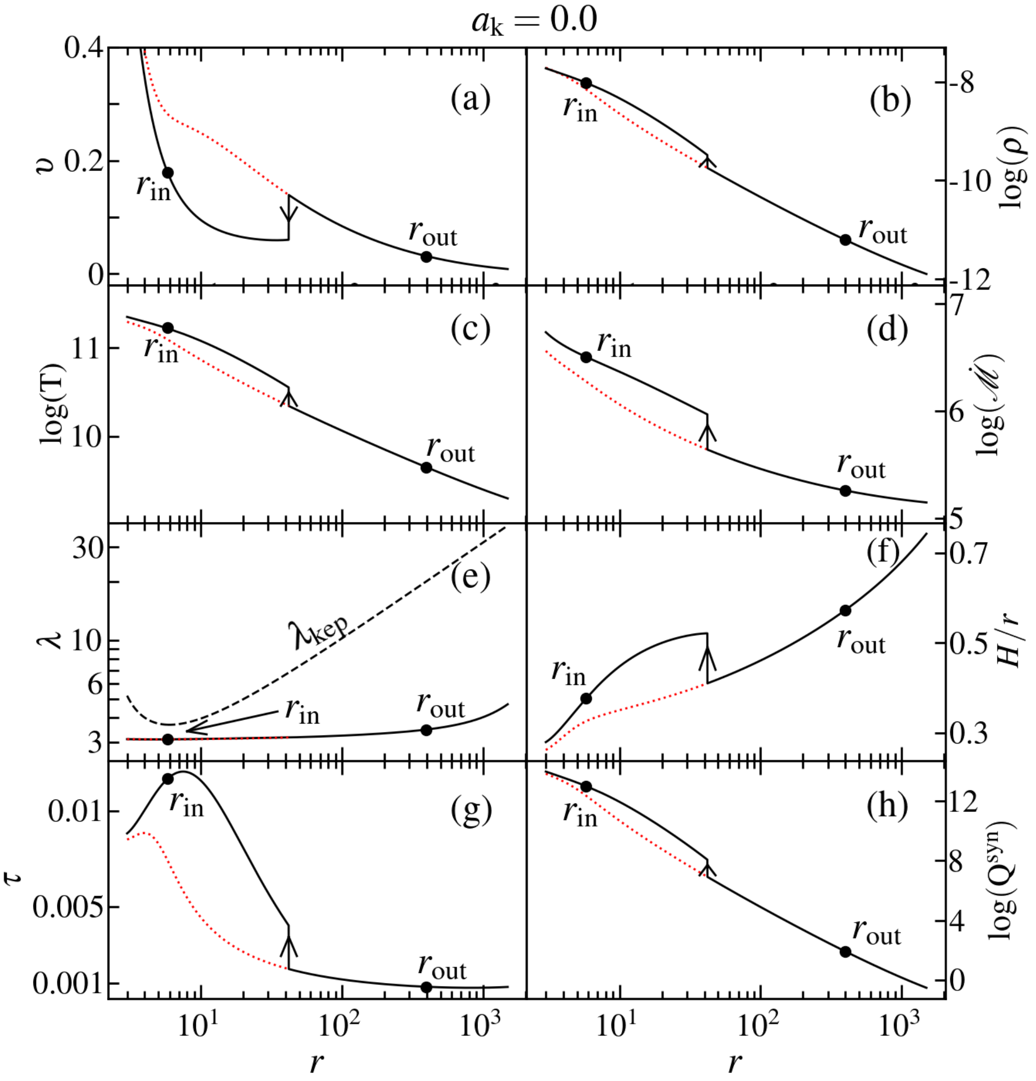

Figure 2.4: Variations of (a) radial flow velocity υ, (b) density ρ, (c) Temperature T, (d) entropy accretion rate $\dot{\mathcal{M}}$, (e) angular momentum λ, (f) disk aspect ratio H/r, (g) optical depth τ, and (h) synchrotron emissivity $Q^{\rm syn}$ for shock-induced accretion solution with r. Here, the vertical arrows represent the shock transition location. The dotted red curve refers to a shock-free solution. See the text for details.

forms at $r_s = 14.33$ in between $r_{\rm out} = 405.46$ and $r_{\rm in} = 1.492$. Here, we observe that for a chosen set of (α_0, θ), shock exists around rapidly rotating BH when $\lambda_{\rm edge}$ assumes a relatively smaller value and vice versa. Indeed, this is expected because accreting matter crosses the BH horizon with angular momentum lower than the marginally stable angular momentum ($\lambda_{\rm ms}$) and $\lambda_{\rm ms}$ evidently decreases with the increase of $a_{\rm k}$ (Das & Chakrabarti, 2008). In Table 2.2, we tabulate the flow variables at the critical points for shock-induced GTAS presented in Figure 2.3.

In Figure 2.4, we show the variations of the different flow variables with radial distance (r) for the shocked accretion solution presented in Figure 2.3. We present the radial velocity (υ) in Figure 2.4(a), where the discontinuous transition of υ can be seen at the shock radius (r_s). We depict the variation of mass density (ρ) of accreting matter in Figure 2.4(b) and find that ρ increases monotonically with decreasing r in the pre-shock branch, although a jump in ρ occurs across the shock front, and this density jump at r_s is inevitable in order to maintain the conservation of mass flux (see equation 2.2). Consequently, the PSC undergoes density enhancement, which is subsequently characterized through the compression ratio defined as $R = \Sigma_+/\Sigma_-$, where Σ ($= 2\rho H$) is vertically integrated mass density of the flow at a given radial distance, and we obtain $R = 2.31$. In Figure 2.4(c), the variation of temperature (T in Kelvin) with r is shown. Temperature enhancement occurs in the PSC as kinetic energy from the upstream (pre-shock) flow undergoes transformation to thermal energy in the downstream (post-shock) flow, consequently producing increased PSC temperatures. The temperature jump at r_s is computed in terms of the shock strength (S), and it is defined as $S = M_-/M_+$, where M_- (M_+) being the pre-shock (post-shock) Mach number. Here, we obtain $S = 2.92$. The entropy accretion rate ($\dot{\mathcal{M}}$) is presented in Figure 2.4(d) and shows that $\dot{\mathcal{M}}$ at PSC is larger compared to the pre-shock region. This discernibly indicates that the shock-induced GTAS are favourable over the shock-free GTAS according to the second law of thermodynamics (Becker & Kazanas, 2001). We demonstrate angular momentum (λ) variation in Figure 2.4(e) and find that the transport of λ remains feeble within several hundreds of gravitational radius, although it increases significantly towards the outer edge of the disk ($r_{\rm edge}$). This possibly happens as the viscous timescale becomes larger than the infall timescale of the accretion flow around the BH. We show that the aspect ratio of the disk is scaled with the radial coordinate in Figure 2.4(f) and find that $H/r < 1$ is maintained all throughout ($r_h \lesssim r \le r_{\rm edge}$) in the presence of shock. Next, we show the variation of scattering optical depth τ in Figure 2.4(g). In this work, τ is expressed as $\tau = \kappa\rho H$, where $\kappa = 0.38$ cm^2 g^{-1}. Since $\tau < 1$, particularly at $r < r_s$, the disk continues to remain optically thin there. Hence, the hard X-ray radiation originating from PSC would escape with ease. In Figure 2.4(h), we illustrate the synchrotron emissivity (in erg cm^{-3} s^{-1}) with r. From the figure, it is clear that the net energy loss from PSC is highly profound in comparison with the pre-shock flow.

Furthermore, in Figure 2.5, we demonstrate the variations of the different flow variables such as υ, ρ, T, $\dot{\mathcal{M}}$, λ, H/r, τ and $Q^{\rm syn}$ with r of the shocked accretion flow around a spinning BH of spin $a_{\rm k} = 0.99$. The figure notably depicts that the overall radial variations of these flow variables are qualitatively similar to the results of $a_{\rm k} = 0.0$, except in the vicinity of the BH horizon (r_h). In particular, we find that τ continues to increase as the flow approaches the horizon ($r \rightarrow r_h$), although it is seen to decrease for weakly rotating BH (see Fig. 2.4). This happens because τ depends in general on density (ρ),

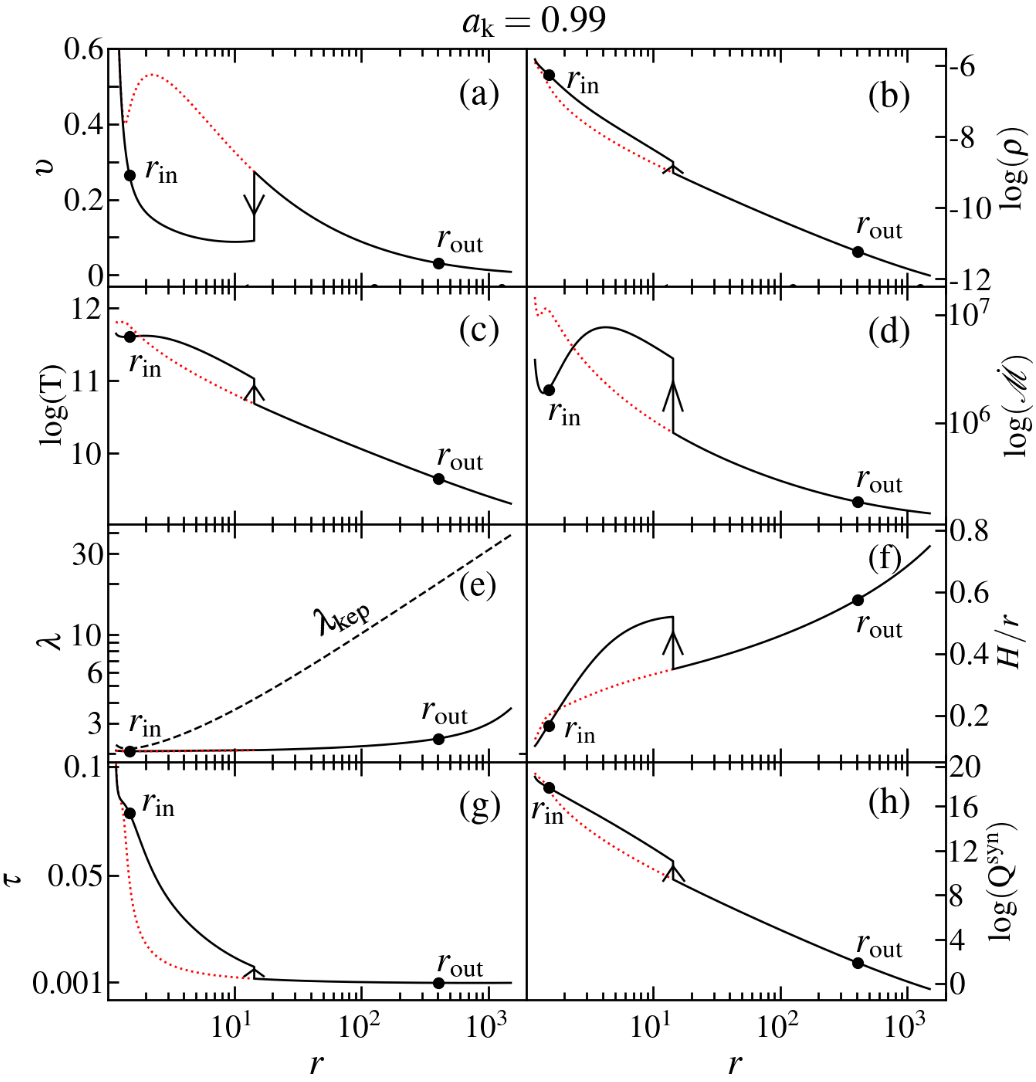

Figure 2.5: Same as Fig. 2.4, but for flow accreting onto a BH of spin $a_k = 0.99$.

and ρ increases significantly in the vicinity of the BH for $a_k = 0.99$. We skip the detailed descriptions of other quantities to avoid repetition.

In Figure 2.6, we present the variation of the shock radius (r_s) with θ for flows injected with fixed outer boundary values at r_{edge}. Here, we choose $\dot{m} = 0.01$, and $\alpha_0 = 0.01$. In the top panel, we fix the energy $\mathcal{E}_{edge} = 1.0004$ and angular momentum $\lambda_{edge} = 4.01$ at $r_{edge} = 1500$ and the flow accretes onto a non-rotating BH of $a_k = 0.0$. We note that for $\theta = 0.0$, the subsonic flow becomes supersonic at $r_{out} = 386.573$ and the shock is formed at $r_s = 129.30$ as the RH conditions are satisfied there. We also calculate the compression ratio and shock strength for this solution, and we obtain $R = 1.65$ and $S = 1.88$. This solution is depicted with the black solid curve, whereas the solid vertical arrow denotes

Table 2.3: Black hole spin ($a_{\rm k}$), power law exponent (θ), inner critical point location ($r_{\rm in}$), inner critical point angular momentum ($\lambda_{\rm in}$), outer critical point location ($r_{\rm out}$), outer critical point angular momentum ($\lambda_{\rm out}$), shock radius (r_s), compression ratio (R), and shock strength (S) for global transonic solutions presented in figure 2.6. See the text for details.

$a_{\rm k}$	θ	$r_{\rm in}$ (r_g)	$\lambda_{\rm in}$ ($r_g c$)	$r_{\rm out}$ (r_g)	$\lambda_{\rm out}$ ($r_g c$)	r_s (r_g)	R	S
0	0	5.315	3.222	386.573	3.419	129.30	1.65	1.88
	0.01	5.520	3.162	387.529	3.373	69.57	2.07	2.51
	0.02	5.787	3.098	388.552	3.322	40.71	2.35	2.99
	0.033	6.295	3.007	389.986	3.252	17.58	2.54	3.35
0.99	0	1.529	2.122	601.228	2.368	35.78	2.90	4.10
	0.01	1.612	2.076	601.479	2.342	18.15	3.17	4.78
	0.015	1.668	2.052	601.615	2.329	13.13	3.24	4.99
	0.021	1.828	2.001	601.907	2.300	6.67	3.27	5.11

the shock radius. As θ is increased to $\theta = 0.01$, shock front moves inwards at $r_s = 69.57$. This happens due to the fact that the increase of θ enhances the viscosity in the accretion flow, and hence, the transport of λ in the outward direction becomes more intense. This weakens the centrifugal repulsion, resulting in the shock moving closer to the BH horizon. Evidently, this finding suggests that shock formation in accretion flow is centrifugally driven. Here, we obtain $R = 2.07$ and $S = 2.51$. We plot this solution using a blue dotted curve. For illustrative purposes, we present an additional solution for $\theta = 0.02$ represented by the dashed curve. Notably, the parameter θ cannot be arbitrarily increased, as we observe that above a critical threshold $\theta_{\rm c} = 0.033$, the RHC for shock formation becomes unfavourable, thereby preventing the shock formation. Although time dependent shocks may be feasible under these conditions, such analysis falls outside the scope of the present study. Notably, θ_c does not have a universal value as it depends on other flow variables. The accretion solution corresponding to $\theta_c = 0.033$ is illustrated using the green dot-dashed curve. In the bottom panel, we present the shocked accretion solutions for flows accreting onto rotating BH of $a_{\rm k} = 0.99$. Here, we choose energy $\mathcal{E}_{\rm edge} = 1.00023$ and angular momentum $\lambda_{\rm edge} = 2.67$ at $r_{\rm edge} = 1500$. The solutions depicted with black (solid), blue (dotted), red (dashed) and green (dot-dashed) correspond to $\theta = 0$, 0.01, 0.015, and $\theta_c = 0.021$, respectively. In Table 2.3, we present the flow quantities respective to these shocked accretion solutions.

In Figure 2.7, variation of shock properties, namely shock radius r_s (upper panel), compression ratio R (middle panel), and shock strength S (lower panel) are depicted with θ. In the left panels, we display the results for the non-rotating BH of $a_{\rm k} = 0.0$, where flows are injected from $r_{\rm edge} = 1500$ with identical energy ($\mathcal{E}_{\rm edge} = 1.0004$) and angular momentum ($\lambda_{\rm edge} = 3.98$). Here, we fix $\dot{m} = 0.01$ and obtain the results for $\alpha_0 = 0.01$

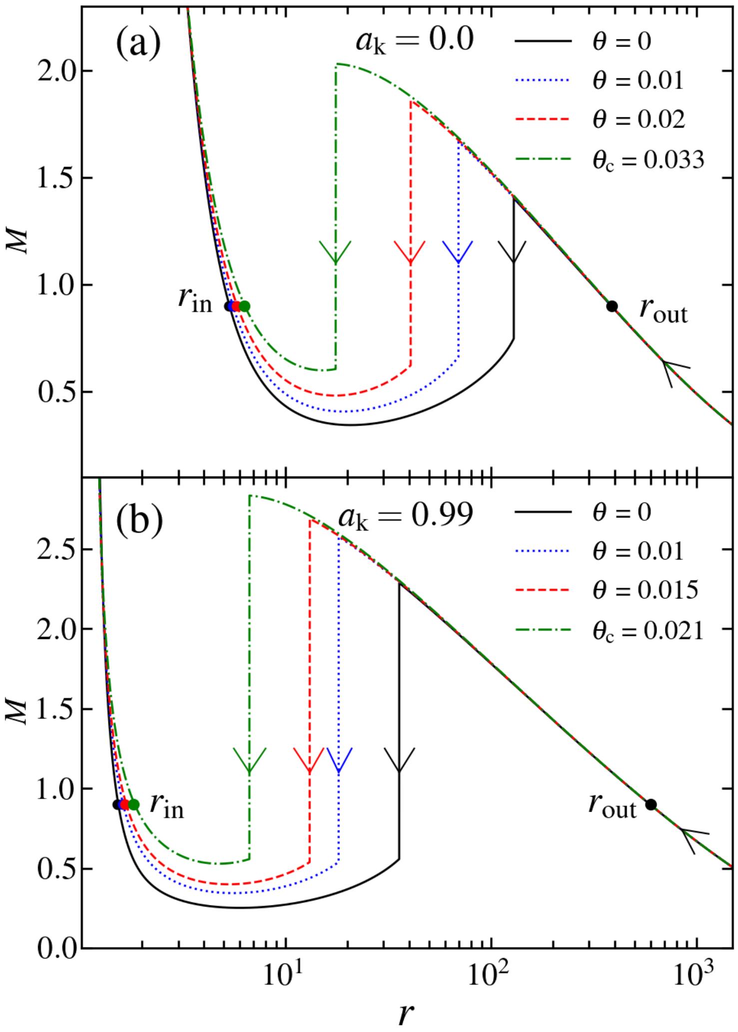

Figure 2.6: Variation of M with r for accretion solutions containing shock waves. Here, we choose global parameters as $\dot{m} = 0.01$, and $\alpha_0 = 0.01$. *Top* panel: Flows with $\mathcal{E}_{\rm edge} = 1.0004$ and $\lambda_{\rm edge} = 4.01$ are injected from $r_{\rm edge} = 1500$ with different θ values onto a non-rotating BH of $a_{\rm k} = 0.0$. *Bottom* panel: Flows with $\mathcal{E}_{\rm edge} = 1.00023$ and $\lambda_{\rm edge} = 2.67$ at $r_{\rm edge} = 1500$ are injected with different θ values onto a rapidly rotating BH of $a_{\rm k} = 0.99$. Critical points are marked with filled circles, and vertical arrows depict the shock transition radii. See the text for details.

(black solid) , 0.011 (blue dashed) and 0.012 (red dotted), respectively. Figure 2.7a clearly demonstrates that stationary shocks exist for an ample range of θ values. As expected, for a constant α_0, the shock radius r_s moves towards the horizon with increasing θ due to the reduction in centrifugal forces opposing gravitational attraction. Additionally, at fixed θ, enhanced values of α_0 increases angular momentum transport efficiency, thereby diminishing the centrifugal barrier. Consequently, the shock front moves inward. It

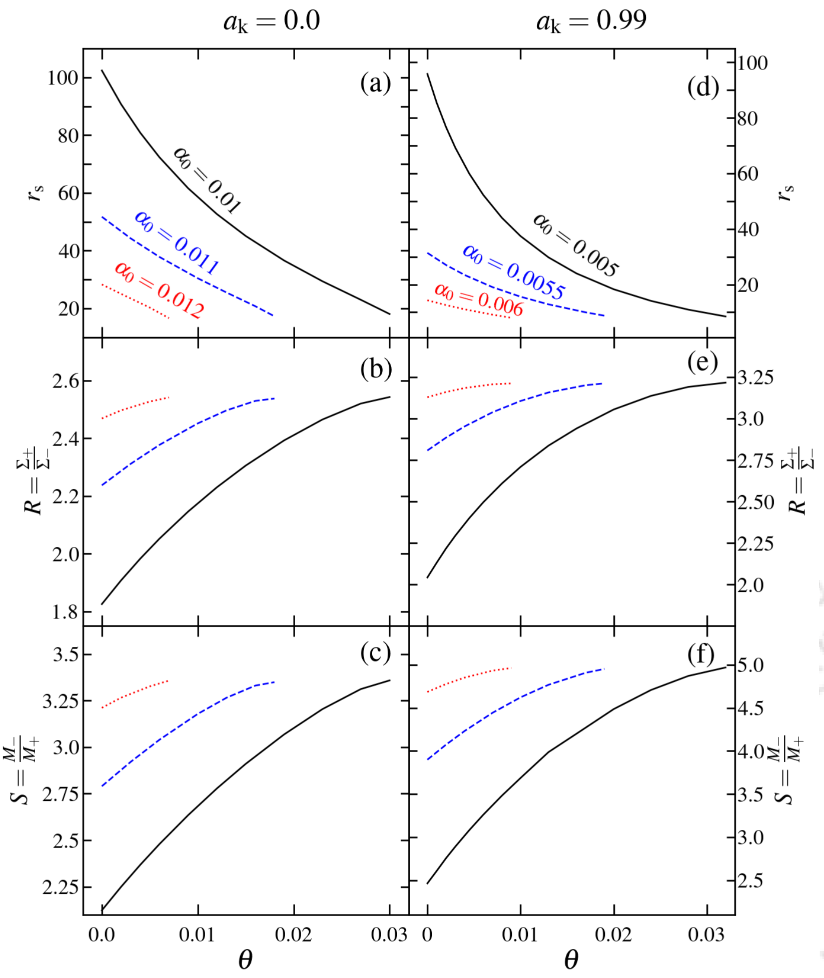

Figure 2.7: Plots of shock radius r_s (upper panel), compression ratio R (middle panel), and shock strength S (lower panel) varied with θ. Here, flow is injected with same energy and angular momentum from the fixed outer edge ($r_{\rm edge}$). In the left panels, Results are shown for $a_{\rm k} = 0$, and solid, dashed, and dotted curves are obtained for $\alpha_0 = 0.01$, 0.011 and 0.012, respectively. In the right panels, results are for $a_{\rm k} = 0.99$, where solid, dashed, and dotted trajectories correspond to $\alpha_0 = 0.005$, 0.0055 and 0.006, respectively. See the text for details.

is noteworthy that for constant α_0, when θ exceeds θ_c, shock formation ceases as the RH conditions are not satisfied. As previously mentioned, θ_c exhibits strict dependence on other flow parameters (see Sect. 2.4). Indeed, the radiative cooling processes that primarily determine the flux of the high energy radiations from the disk are strongly dependent on both ρ and T distributions across the shock transition (Chakrabarti & Titarchuk, 1995; Mandal & Chakrabarti, 2005). Keeping this in mind, in Figure 2.7b, we illustrate the variation of the compression ratio (R, measure of density compression across shock) as a function of θ corresponding to shock-induced GTAS presented in Figure 2.7a.

We see that when θ is enhanced, shock front is generally pushed towards the BH. Due to this, PSC becomes compressed, causing the overall increment in R. A similar trend is generally observed in the variation of R irrespective of the α_0 values, provided that shock wave exists. Similarly, in Figure 2.7c, we present how shock strength (S, measure of temperature jump across the shock transition) varies with various θ for the solutions presented in Figure 2.7a. It is clear that for a fixed α_0, shock strength S monotonically increases as θ is increased and ultimately shifts from a weaker to a stronger regime. We continue the analyses and present the outcome for $a_{\rm k} = 0.99$ in the right side panels of Figure 2.7, where flows are injected from $r_{\rm edge} = 1500$ with identical $\mathcal{E}_{\rm edge} = 1.0004$, $\lambda_{\rm edge} = 2.44$, and $\dot{m} = 0.001$. To maintain the θ parameter range, we select relatively lower values of $\dot{m}$ compared to those employed for flows surrounding non-rotating BH. In Figures 2.7d-f, results are are shown for $\alpha_0 = 0.005$ (solid), 0.0055 (dashed) and 0.006 (dotted), respectively. Notably, the collective variations of r_s, R, and S with respect to θ for $a_{\rm k} = 0.99$ display qualitatively analogous characteristics as those depicted in the left panels for $a_{\rm k} = 0.0$.

In Figure 2.8, we examine the effect of accretion rate ($\dot{m}$) on shock properties in a convergent accretion flow. This important investigation is extremely useful because radiative cooling phenomena are regulated by $\dot{m}$. While doing so, we inject matter onto a non-rotating BH ($a_{\rm k} = 0.0$) from $r_{\rm edge} = 1500$ with $\mathcal{E}_{\rm edge} = 1.0004$, $\lambda_{\rm edge} = 3.98$ and $\alpha_0 = 0.01$. We present the obtained results in left panels, where solid, dashed, and dotted curves correspond to $\dot{m} = 0.01$, 0.1 and 0.2, respectively. Similarly, for $a_{\rm k} = 0.99$, we choose $r_{\rm edge} = 1500$, $\mathcal{E}_{\rm edge} = 1.0004$, $\lambda_{\rm edge} = 2.44$, $\alpha_0 = 0.005$, and results are shown in the right panels. The spin values are marked at the top of the figure. In panels (a) and (d), we depict the variation of r_s with θ, where shock fronts are observed to move further inward close to the BH horizon as θ increases. This feature is commonly observed irrespective of $\dot{m}$ values provided that a shock is formed. Furthermore, for fixed θ, increasing $\dot{m}$ causes the shock front to migrate inward towards to BH horizon. This behaviour is expected since increased $\dot{m}$ enhances cooling effects within the PSC, that reduces thermal pressure. Therefore, the shock conditions are satisfied at a radius nearer to the horizon to preserve pressure balance across the shock discontinuity. In panels (b) and (e), we compare the compression ratio (R) and notice that R increases with θ. This evidently indicates that for a convergent flow, accretion shock becomes stronger as r_s decreases. We further find that shock strength S increases monotonically with θ, and for a given θ, when shocks form closer to BH, S is enhanced and vice versa (see panels (c) and (f)).

Next, we investigate the effect of BH spin ($a_{\rm k}$) on r_s and display the obtained results in Figure 2.9, where the variation of r_s with $a_{\rm k}$ for various values of θ is shown. To examine this, we supply matter from $r_{\rm edge} = 1500$ with $\lambda_{\rm edge} = 3.78$, $\mathcal{E}_{\rm edge} = 1.0004$, $\dot{m} = 0.01$ and $\alpha_0 = 0.01$. In the figure, solid (black), dashed (blue), dotted (red), dot-dashed (green) and big-dashed (magenta) curves are used to identify the results corresponding

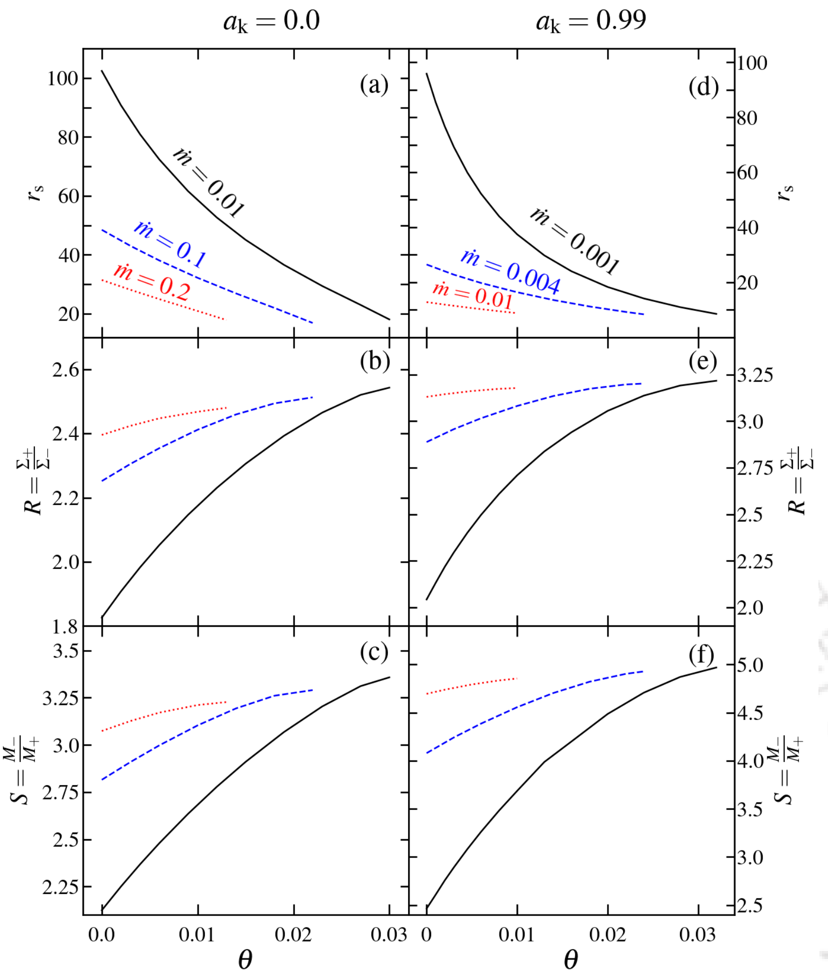

Figure 2.8: Plot of r_s (upper panel), R (middle panel), and S (lower panel) with θ for accreting flows with different $\dot{m}$. In left panels, we fix $r_{\rm edge} = 1500$, $\mathcal{E}_{\rm edge} = 1.0004$, $\lambda_{\rm edge} = 3.98$, and $a_{\rm k} = 0.0$. Solid, dashed, and dotted curves are for $\dot{m} = 0.01$, 0.1 and 0.2. For right panels, we choose $r_{\rm edge} = 1500$, $\mathcal{E}_{\rm edge} = 1.0004$, $\lambda_{\rm edge} = 2.44$, and $a_{\rm k} = 0.99$. Solid, dashed, and dotted curves are for $\dot{m} = 0.001$, 0.004 and 0.01. See the text for details.

to $\theta = 0.0, 0.03, 0.05, 0.07$, and 0.095, respectively. It is evident from the figure that for a fixed θ, r_s shifts outwards from the BH horizon as $a_{\rm k}$ increases for flows with fixed outer boundary conditions. Accordingly, the effective size of the PSC is enhanced, and hence, the possibility of up-scattering the soft photons from the pre-shock disk at PSC is increased in producing the high energy radiations. Furthermore, we observe that for specified θ, shock formation occurs within a particular range of $a_{\rm k}$, and as θ increases, the allowed range of $a_{\rm k}$ shifts toward higher values. This behavior is expected since, for constant $\lambda_{\rm edge}$, increased θ enhances angular momentum transport, resulting in overall reduction of $\lambda(r)$ in the vicinity of the BH. Indeed, it is evident that for higher $a_{\rm k}$, shock

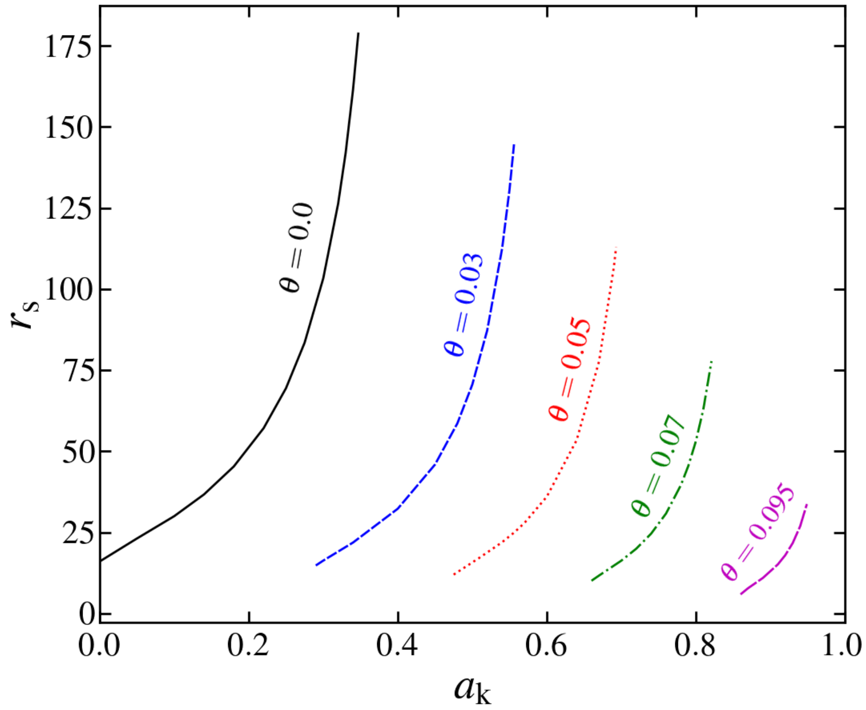

Figure 2.9: Variation of r_s with a_k for different θ values. Results presented using solid, dashed, dotted, dot-dashed and big-dashed curves are for $\theta = 0.0, 0.03, 0.05, 0.07$, and 0.095, respectively. See the text for details.

exists when λ is relatively low (Das & Chakrabarti, 2008), and this happens because of spin-orbit coupling present in the effective potential (see equation (2.1a)) describing spacetime geometry around BH, where the marginally stable angular momentum is seen to decrease with the increase of a_k. Consequently, the range of λ for shock is also decreased with the increase of a_k. These findings align with the results of Sen et al. (2022). In contrast, we see that r_s decreases with the increase in θ for flows accreting onto a BH for a fixed spin (a_k) value. Moreover, we also observe that the lower limit of r_s is gradually reduced when the flow with fixed outer boundary accretes onto the BHs of increasing spin (a_k) values.

2.4 Shock parameter space

In this section, we proceed further to determine the region of model parameters that supports stationary shock solutions for viscous advective accretion flow around BHs. Figures 2.6-2.9 clearly demonstrate that shock-induced GTAS emerge across wide range of angular momentum and θ values. Hence, we investigate how the shock characteristics varies with θ in a viscous flow, and identify the effective domain of parameter space in terms of θ in the $\lambda_{\rm in} - \mathcal{E}_{\rm in}$ plane, where $\lambda_{\rm in}$ and $\mathcal{E}_{\rm in}$ represent the angular momentum and

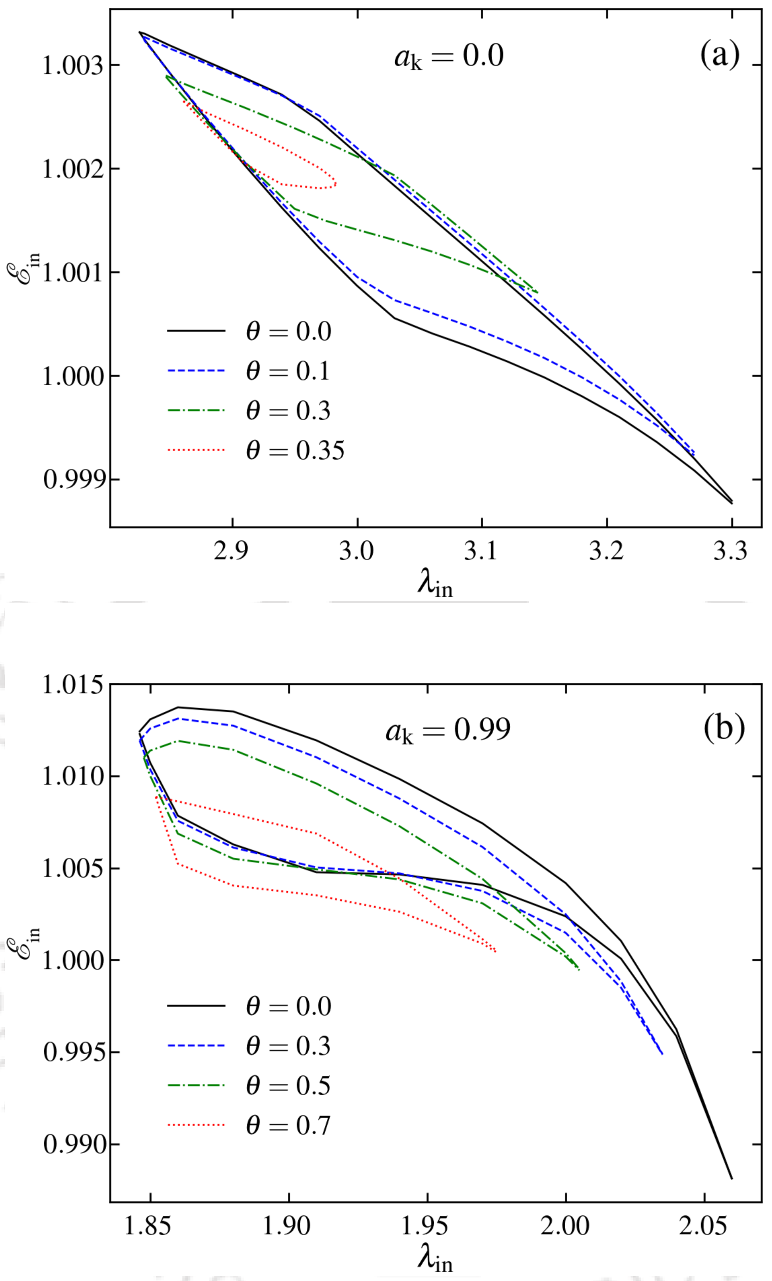

Figure 2.10: Modification of the effective domain of the shock parameter space as a function of θ. Upper panel (a) is for the non-rotating BH of $a_k = 0$, whereas bottom panel (b) depicts results for the rotating BH of $a_k = 0.99$. See the text for details.

energy of the flow at r_{in} (Aktar et al., 2017b, 2019). We select $\mathcal{E}_{in}$ and λ_{in} in defining the shock parameter space as the flow is expected to advect into BH with energy and angular momentum similar to these values. The results are shown in Figure 2.10, where panel (a) is for $a_k = 0.0$ and the effective region bounded with solid (black), dashed (blue), dot-dashed (green), and dotted (red) curves are for $\theta = 0.0, 0.1, 0.3$, and 0.35, respectively. Here, we choose $\dot{m} = 0.01$. Similarly, in panel (b), we depict the results

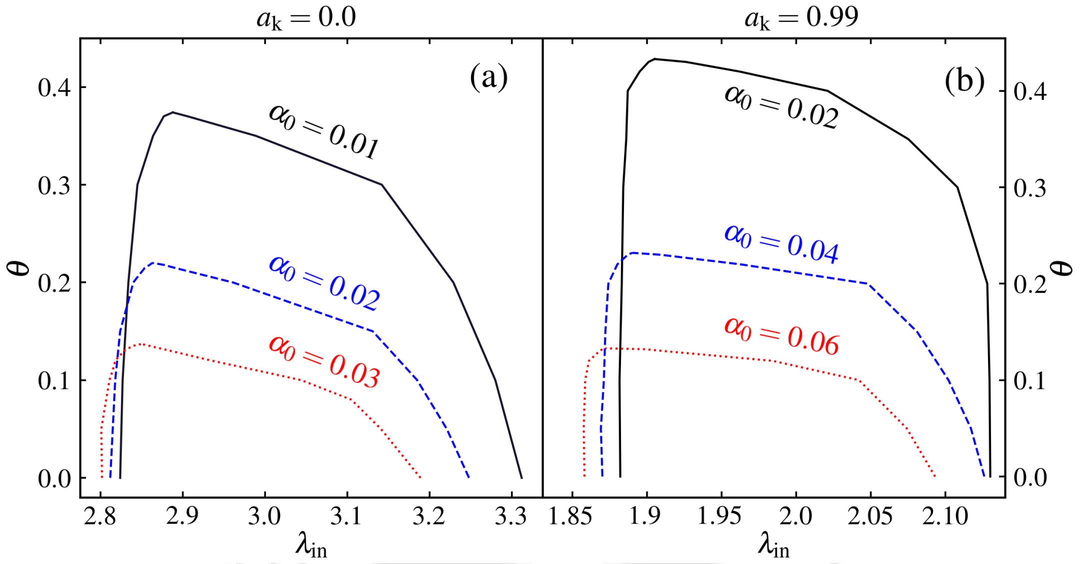

Figure 2.11: Variation of θ with angular momentum at the inner critical point (λ_{in}) that contain shock wave. In panel (a), $a_k = 0.0$ and solid, dashed and dotted curves show results for $\alpha_0 = 0.01, 0.02$, and 0.03, respectively. Similarly, in panel (b), $a_k = 0.99$, and solid, dashed and dotted curves are for $\alpha_0 = 0.02, 0.04$, and 0.06. Here, we set $\dot{m} = 0.01$. See the text for details.

for $a_k = 0.99$, where solid (black), dashed (blue), dot-dashed (green), and dotted (red) curves are used to separate the region for $\theta = 0.0, 0.3, 0.5$, and 0.7, respectively. Here, we set $\dot{m} = 10^{-4}$. In each panel, a_k and θ values are marked. We find that in both panels, the effective region of $\lambda_{in} - \mathcal{E}_{in}$ space for stationary shock is reduced as θ increases, and accordingly, the possibility of shock formation is also diminished (Chakrabarti & Das, 2004; Das, 2007). Indeed, when θ exceeds its limiting value (*i.e.*, $\theta > \theta^{max}$), the parameter space for standing shock disappears. Note that for $\theta > \theta^{\max}$, flow angular momentum at the vicinity of the BH is decreased to such an extent that the centrifugal barrier becomes very weak and it cannot form a shock wave. Hence, stationary shock ceases to exist. Nevertheless, time-dependent shocked accretion solutions may persist for $\theta > \theta^{max}$, which were examined by numerical simulation to study the oscillatory behaviour of shock solutions (Molteni et al., 1994; Das et al., 2014b; Suková & Janiuk, 2015; Lee et al., 2016). Interestingly, the solutions of this type successfully account for the Quasi-periodic Oscillations (QPOs) phenomenon that are generally observed in BH-XRBs (Nandi et al., 2012; Sreehari et al., 2020; Majumder et al., 2022).

We continue our study to investigate the ranges of λ_{in} and θ in terms of α_0 that admit shock-induced GTAS. In doing so, we fix $\dot{m} = 0.01$ and scan the range of θ for a given combinations of (λ_{in}, α_0) by freely varying r_{in} (equivalently $\mathcal{E}_{in}$). The results are presented for $a_k = 0.0$ and 0.99 in Figure 2.11. In panel (a), solid (black), dashed (blue), and dotted (red) are delineated for $\alpha_0 = 0.01$, 0.02, and 0.03, which separate the region for shocked accretion solutions from the shock-free solutions. Similarly, in panel (b), solid (black),

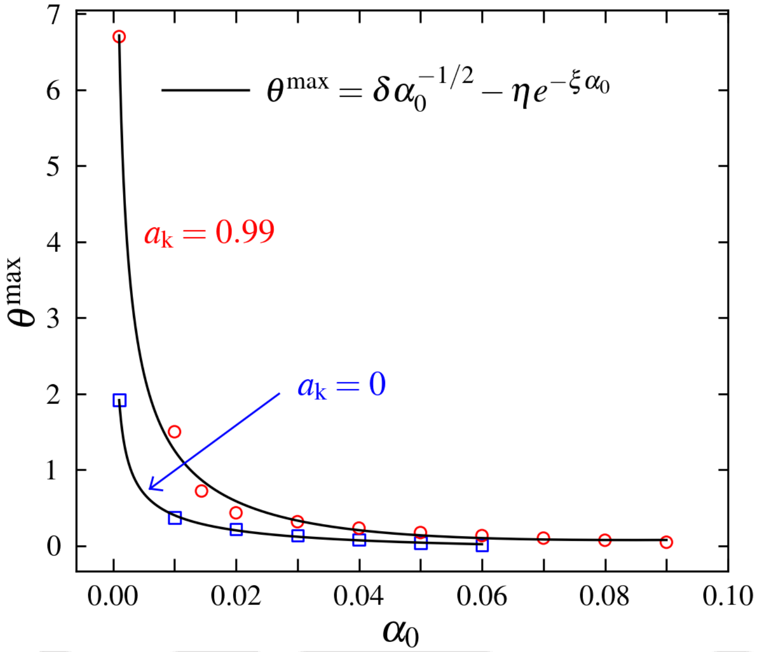

Figure 2.12: Variation of $\theta^{\rm max}$ as function of α_0 for shock-induced accretion solutions. Results represented using open squares and open circles are for $a_{\rm k} = 0.0$ and 0.99, respectively. Solid curves depict the fitted function as mentioned in the text. Here, we fix $\dot{m} = 0.01$. See the text for details.

Table 2.4: Values of the coefficients obtained from the best fit representation of $\theta^{\rm max}$ $(= \delta\alpha_0^{-1/2} - \eta e^{-\xi\alpha_0})$ yielding shock-induced GTAS (see figure 2.12). See the text for details.

$a_{\rm k}$	δ	η	ξ
0	0.07	0.31	2.50
0.99	0.25	1.39	6.48

dashed (blue), and dotted (red) curves are displayed for $\alpha_0 = 0.02$, 0.04, and 0.06. We find that the viable shock region in $\lambda_{\rm in} - \theta$ plane progressively reduces with the increase of α_0 for both non-rotating and rapidly rotating BHs. In addition, we find that for a given α_0, θ reaches its maximum value, namely $\theta^{\rm max}$, at a fixed $\lambda_{\rm in}$. We further observe that as α_0 is increased, the value of $\theta^{\rm max}$ is decreased, and this occurs at correspondingly lower $\lambda_{\rm in}$ values.

Figure 2.12 illustrates the variation $\theta^{\rm max}$ with α_0. Open squares denote the results for $a_{\rm k} = 0.0$, while open circles correspond to $a_{\rm k} = 0.99$. These data points are further fitted empirically using the expression $\theta^{\rm max} = \delta\alpha_0^{-1/2} - \eta e^{-\xi\alpha_0}$, where δ, η, and ξ are the constants, and their values strictly depends on $a_{\rm k}$ which are listed in Table 2.4. In the figure, solid curves denote the best-fit representations of the fitted function described above for $a_{\rm k} = 0.0$ and 0.99, respectively. The figure clearly demonstrates that the accretion flows with relatively higher viscosity continue to harbour shock waves around the highly spinning BHs as compared to the weakly rotating BHs. This behavior occurs primarily because of the fact that the outer critical points transition to nodal type (Dihingia et al., 2019a) at higher viscosity for $a_{\rm k} \rightarrow 0$, thereby preventing shock-induced GTAS formation.

2.5 Chapter Conclusion

In this study, we investigate the properties of the viscous accretion flow that includes the more general viscosity prescription than those usually discussed in the literature (Narayan & Yi, 1994; Chakrabarti, 1996; Chakrabarti & Das, 2004, and references therein). In particular, we consider the viscosity parameter to vary with the radial coordinate as $\alpha(r)$ and observe that GTAS continue to exist around the rotating BH. Depending on input parameters, *i.e.*, viscosity, angular momentum, accretion rate, the accretion flow may harbour shock waves. Indeed, the shock-induced GTAS are significantly promising in the sense that it has the potential to explain the spectro-temporal properties of BH sources (Chakrabarti & Manickam, 2000; Nandi et al., 2001; Smith et al., 2001, 2002; Nandi et al., 2012; Iyer et al., 2015; Das et al., 2021). We find important results that are presented below.

1. There exist global transonic accretion solutions (GTAS) that pass through inner critical points ($r_{\rm in}$, ADAF-type) or outer critical points ($r_{\rm out}$, Bondi-type) for low angular momentum flow. We find that when viscosity is suitably adjusted through modification of the viscosity exponent θ, while maintaining constant values for other flow parameters at the outer boundary ($r_{\rm edge}$), ADAF-type solutions undergo a transition in character to resemble Bondi-type flows (see Figure 2.1). Furthermore, when θ is decreased for an ADAF-type solution, the global accretion solution eventually becomes closed, as it could not connect to the outer edge of the disk (see Figure 2.2), although it can be joined with a Bondi-type solution via the Rankine-Hugoniot standing shock conditions (see Figure 2.3). Notably, these findings are seen in both weakly rotating ($a_{\rm k} \rightarrow 0$) and rapidly rotating ($a_{\rm k} \rightarrow 1$) BHs. Since it is commonly perceived that BHs may accrete low angular momentum flow from their surrounding environment, shock seems to be an indispensable element in the accretion flow.

2. We observe that due to the shock transition, convergent accretion flow is compressed, yielding hot and dense PSC (see Figure 2.4-2.5). Thus, PSC harbours the swarm of hot electrons, which are expected to reprocess the low energy photons from pre-shock flow through inverse Comptonization and produce hard X-ray radiations (Chakrabarti & Titarchuk, 1995; Mandal & Chakrabarti, 2005). Such a signature of excessively high energy radiations is frequently observed from galactic X-ray binaries containing BH sources (Sunyaev & Titarchuk, 1980; Iyer et al., 2015; Baby

et al., 2020, and references therein). Based on this, we deduce that the shock radius (r_s), which coarsely measures the size of PSC, is likely to play a significant role in emitting hard X-ray radiation from the accretion disk.

3. When viscosity is enhanced in the flow, the efficiency of the angular momentum transport increases that evidently reduces the centrifugal repulsion against gravitational force. As a result, for higher θ, the size of PSC is diminishes as the shock front migrate inward to satisfy the pressure balance on both sides of the discontinuity (see Figure 2.6). Therefore, by suitably changing θ, we can control the accreting dynamics, including PSC, while explaining the disk emission.

4. We calculate the limiting range of flow parameters that admit shock transition in viscous accretion flow around both non-rotating and rapidly rotating BHs. We find that shock-induced GTAS are not discrete solutions. In fact, solutions of this type are obtained for an extensive range of the flow parameters (see Figure 2.10). Nevertheless, the possibility of shock formation diminishes as we increase viscosity, and above a critical limit of $\theta > \theta^{\rm max}$, the shock disappears. Notably, $\theta^{\rm max}$ does not own a universal value as it depends on other flow variables.

5. We determine $\theta^{\rm max}$ as function of α_0 for $a_{\rm k} = 0$ and 0.99, and find that it sharply decreases at higher α_0 and ultimately settles down to its asymptotic limit (see Figure 2.12).

Finally, we acknowledge the limitations of this formalism as it is developed considering several assumptions. We employ an effective potential to characterise the space-time geometry around the rotating BH, avoiding a rigorous general relativistic approach. We do not consider the structured large-scale magnetic fields and use a stochastic magnetic field configuration. Additionally, we also assume that the flow maintain a single temperature distribution, although the flow is expected to exhibit two-temperature (for both ions and electrons) profiles.

Role of thermal conduction in relativistic hot accretion flows around rotating black holes with shock

3

> `"...Science and everyday life cannot and should not be separated....."`
>
> *Rosalind Franklin*

In the previous Chapter, we discussed the effect of viscosity, which dictates the rate of transport of angular momentum and the energy dissipation in the flow. We also illustrate the dynamics of shock wave and shock properties with viscosity parameters (α_0 and θ). However, in the scenario, when the central source accretes matter at very low accretion rates, the temperature and density profiles of the hot accreting matter resemble those of radiatively inefficient accretion flows (RIAFs) due to reduced radiative efficiency (Yuan & Narayan, 2014). In this regime, the accreting plasma is expected to remain in a weakly collisional state, with mean free paths exceeding the typical length scales of the accretion disk structure, equivalently, the gravitational radius (r_g). In RIAF, the generated heat is advected towards the horizon. In such an environment, the role of thermal conduction comes into play, and due to thermal conduction, the heat can be redistributed from the inner hot region to the colder outer part of the disk (Tanaka & Menou, 2006). Therefore, the local temperature of the disk gets distributed, and the thermal properties and structure of the disk alter (Tanaka & Menou, 2006; Sharma et al., 2008; Shadmehri, 2008; Khajenabi & Shadmehri, 2013b; Ghoreyshi & Shadmehri, 2020; Mitra et al., 2023). Inspired by this, in this Chapter, we examine the effect of the thermal conduction in the viscous relativistic hot accretion flow around both non-rotating ($a_{\rm k} = 0.0$) and rapidly rotating ($a_{\rm k} = 0.99$) BHs. We study the properties of transonic flow

---

The contents of this chapter are published in Singh & Das (2025) and the formation of the standing shock in the presence of thermal conduction. We also examine the shock properties, namely shock radius ($r_{\rm s}$), compression ratio (R) and shock strength (S) in terms of the model parameters. We find that shock continues to form even in presence of high thermal conduction around both non-rotating ($a_{\rm k} \rightarrow 0$) and rapidly ($a_{\rm k} \rightarrow 0$) rotating black holes. We further identify the parameter space, spanned by the energy and angular momentum of the flow, that permits shocked accretion solutions, and investigate how this parameter space is altered by the influence of thermal conduction. Finally, we determine the critical value of thermal conduction ($\Phi_{\rm s}^{\rm cri}$) that admits standing shocks in dissipative accretion flow and observe that ($\Phi_{\rm s}^{\rm cri}$) exhibits dependencies on viscosity (α), parametric cooling (f_c) and $a_{\rm k}$.

3.1 Basic considerations and governing equations

We consider axisymmetric, viscous, advective accretion flow around a rotating black hole. To describe the accretion flow, we employ the cylindrical coordinate system (r, ϕ, z) with the black hole residing at the origin. In addition, we consider the flow to be in hydrostatic equilibrium in the vertical direction (along the z-direction).

The spacetime geometry of a rotating Kerr-like black hole is satisfactorily described by an effective potential ($\Phi_{\rm e}^{\rm eff}$) (Dihingia et al., 2018a) given by,

$$\Phi_{\rm e}^{\rm eff} = 1 + \frac{1}{2}\ln\left[\frac{r\Delta}{a_{\rm k}^2(r+2) - 4a_{\rm k}\lambda + r^3 - \lambda^2(r-2)}\right], \tag{3.1}$$

where r is the radial coordinate, $a_{\rm k}$ refers the spin of the black hole, and $\Delta = r^2 - 2r + a_{\rm k}^2$. The suffix 'e' denotes the quantity measured at the disk equatorial plane.

The governing hydrodynamic equations that describe the axisymmetric accretion flow in the steady state are, Mass flux conservation, equation, radial momentum conservation equation, azimuthal momentum equation conservation, and energy equation. Here, First 3 equations are same, as it is previous chapter, and only chnages occur in the energy equation due to the thermal conduction part, which is given by,

(a) Mass flux conservation equation:

$$\dot{M} = 2\pi \upsilon \Sigma \sqrt{\Delta}\ , \tag{3.2}$$

(b) The radial momentum equation:

$$\upsilon\frac{d\upsilon}{dr} + \frac{1}{h\rho}\frac{dP}{dr} + \frac{d\Phi_{\rm e}^{\rm eff}}{dr} = 0, \tag{3.3}$$

(b) The azimuthal momentum equation:

$$\upsilon\frac{d\lambda}{dr} + \frac{1}{\Sigma r}\frac{d}{dr}(r^2 W_{r\phi}) = 0, \tag{3.4}$$

and (d) The energy equation:

$$\frac{\upsilon}{\Gamma-1}\left(\frac{dP}{dr}-\frac{\Gamma P}{\rho}\frac{d\rho}{dr}\right)=f_{\rm c}\alpha r(P+\rho\upsilon^2)\frac{d\Omega}{dr}+\frac{1}{r}\frac{d(rF_{\rm s})}{dr} \qquad (3.5)$$

The local variables υ, ρ, P and Σ represent the radial velocity, mass density, isotropic pressure, and vertically integrated density of the flow (Matsumoto et al., 1984). In equation (3.4), $W_{r\phi}$ refers to the vertically integrated viscous stress and is given by

$$W_{r\phi}=-\alpha\Pi=-\alpha\left(W+\Sigma\upsilon^2\right), \qquad (3.6)$$

where α is the viscosity parameter that determines the angular momentum transport inside the disk, and W and Π $(=W+\Sigma\upsilon^2)$ correspond to the vertically integrated gas pressure and total pressure (Matsumoto et al., 1984), respectively. In equation (3.5), Γ denotes the adiabatic index, and H is the local half-thickness of the disk, which is expressed as (Riffert & Herold, 1995; Peitz & Appl, 1997),

$$H^2=\frac{Pr^3}{\rho\mathcal{F}},\ \mathcal{F}=\frac{1}{(1-\lambda\Omega)}\times\frac{(r^2+a_{\rm k}^2)^2+2\Delta a_{\rm k}^2}{(r^2+a_{\rm k}^2)^2-2\Delta a_{\rm k}^2},$$

where Ω represents the angular velocity of the flow and given by,

$$\Omega=\frac{2a_{\rm k}+\lambda(r-2)}{a_{\rm k}^2(r+2)-2a_{\rm k}\lambda+r^3}.$$

The first term on the right-hand side of equation (3.5), we incorporate the parametric cooling factor $f_{\rm c}$ $(=1-Q_{\rm rad}/Q_{\rm vis})$, where $Q_{\rm vis}$ and $Q_{\rm rad}$ refers the viscous heating and radiative cooling rates (Narayan & Yi, 1994; Mitra et al., 2023). In this study, we treat $f_{\rm c}$ to be constant throughout the flow, with $0\le f_{\rm c}\le 1$. When the flow is advection-dominated, $f_{\rm c}=1$, and $f_{\rm c}=0$ correspond to flow dominated by radiative cooling. The second term on the right hand side of Equation (3.5) represents the energy transfer due to saturated thermal conduction (Tanaka & Menou, 2006). Here, $F_{\rm s}$ expresses the saturated conduction flux (Cowie & McKee, 1977), and is defined as $F_{\rm s}=5\Phi_{\rm s}\rho\left(\frac{P}{\rho}\right)^{3/2}$, where $\Phi_{\rm s}$ is the dimensionless saturated conduction parameter (hereafter conduction parameter) with values ranging as $0\le\Phi_{\rm s}\le 1$, and it governs the effect of thermal conduction inside the disk. Note that $\Phi_{\rm s}$, α and $f_{\rm c}$ are often collectively referred to as dissipation parameters.

We close the governing equations (3.2-3.5) employing an equation of state (EoS) that establishes relationships among the internal energy (ϵ), pressure (P) and density (ρ) of the accreting matter. Under realistic conditions, the thermally non-relativistic (adiabatic index $\Gamma=5/3$) flow at the outer edge becomes thermally relativistic ($\Gamma=4/3$) upon approaching the inner edge of the disk. Consequently, to address the thermally relativistic flow, we adopt a relativistic EoS in accommodating the variable adiabatic index (Γ). For accreting fluid consisting of ions and electrons, the relativistic EoS is given by (Chattopadhyay & Ryu, 2009),

$$\epsilon = n_e m_e \rho = \frac{\rho}{\tau} F, \quad \text{and} \quad P = \frac{2\rho\Theta}{\tau}, \tag{3.7}$$

where $\tau = 1 + m_p/m_e$ and

$$F = \left[1 + \Theta\left(\frac{9\Theta + 3}{3\Theta + 2}\right)\right] + \left[\frac{m_p}{m_e} + \Theta\left(\frac{9\Theta m_e + 3m_p}{3\Theta m_e + 2m_p}\right)\right],$$

Here, m_p and m_e refer to the masses of ion and electron, respectively, and Θ $(= k_\mathrm{B}T/m_e c^2)$ is the dimensionless temperature, T is the temperature in Kelvin and k_B is the Boltzmann constant. We delineate sound speed as $C_s = \sqrt{2\Gamma\Theta/(F + 2\Theta)}$, where Γ $[= (1+N)/N]$ denotes the adiabatic index and N $[= (1/2)(dF/d\Theta)]$ is the polytropic index of the flow, respectively (Dihingia et al., 2019a).

Following Chattopadhyay & Ryu (2009) and utilizing the equation (3.2), we compute the entropy accretion rate as,

$$\dot{\mathcal{M}} = \upsilon H \sqrt{\Delta}\left[\Theta^2(2 + 3\Theta)(3\Theta + 2m_p/m_e)\right]^{3/2} \exp\left(k_1\right),$$

where $k_1 = \left[F - (1 + m_p/m_e)\right]/2\Theta$.

We simplify equations (3.2), (3.3), (3.4), (3.5) and (3.7) and obtain the coupled differential equations involving flow variables as

$$R_0 + R_\upsilon \frac{d\upsilon}{dr} + R_\Theta \frac{d\Theta}{dr} + R_\lambda \frac{d\lambda}{dr} = 0 \tag{3.8}$$

$$L_0 + L_\upsilon \frac{d\upsilon}{dr} + L_\Theta \frac{d\Theta}{dr} + L_\lambda \frac{d\lambda}{dr} = 0, \tag{3.9}$$

$$E_0 + E_\upsilon \frac{d\upsilon}{dr} + E_\Theta \frac{d\Theta}{dr} + E_\lambda \frac{d\lambda}{dr} = 0. \tag{3.10}$$

The explicit mathematical expression of the coefficients (R_i, L_i, E_i, $i \to 0$, υ, Θ and λ) in equations (3.8), (3.9) and (3.10) are complex in nature and given in the Appendix-B.

Using equations (3.8), (3.9) and (3.10), we obtain the wind equation given by,

$$\frac{d\upsilon}{dr} = \frac{\mathcal{N}(r, \upsilon, \lambda, \Theta)}{\mathcal{D}(r, \upsilon, \lambda, \Theta)}, \tag{3.11}$$

where the numerator $\mathcal{N}(r, \upsilon, \lambda, \Theta)$ and denominator $\mathcal{D}(r, \upsilon, \lambda, \Theta)$ are functions of flow variables and their explicit expressions are provided in Appendix-B. In addition, we calculate the gradient of Θ and λ as,

$$\frac{d\Theta}{dr} = \Theta_1 + \Theta_2 \frac{d\upsilon}{dr}, \quad \text{and} \quad \frac{d\lambda}{dr} = \lambda_1 + \lambda_2 \frac{d\upsilon}{dr}, \tag{3.12}$$

where Θ_1, Θ_2, λ_1 and λ_2 are expressed in Appendix-B.

Critical point analysis

We discussed the critical point methodology in Chapter 2. Following the same procedure, we self-consistently solve the coupled differential equations (3.11) and (3.12) for a set of model parameters to obtain the global transonic accretion solution around the black hole. For this study, we treat α, $\Phi_{\rm s}$ and $a_{\rm k}$ as global parameters. Furthermore, we choose a reference radius $r_{\rm ref}$ and the angular momentum ($\lambda_{\rm ref}$) at $r_{\rm ref}$ as local parameters to numerically integrate these equations (3.11-3.12). The accretion solutions around the black holes are inherently transonic; the flow inevitably passes through the critical point. Hence, adopting the approach presented in Chakrabarti & Das (2004), we select the critical point ($r_{\rm c}$) as the reference radius *i.e.*, $r_{\rm c} = r_{\rm ref}$ and integrate equations (3.11) and (3.12) bidirectionally from $r_{\rm c}$, inward up to the horizon and then outward to a distant radius (hereafter 'disk outer edge $r_{\rm edge}$'). Subsequently, we combine these two segments of the solution to construct a comprehensive global transonic accretion solution. In particular, depending on local and global parameters, the accretion flow can exhibit single or multiple critical points (Das, 2007; Das et al., 2021, and references therein). As we discussed in Chapter 2, the presence of multiple critical points is a prerequisite for triggering a shock transition in an accretion flow around a black hole (Das et al., 2001).

3.2 Global Transonic Accretion Solutions

In Figure 3.1, we present representative examples of accretion solutions, where Mach number ($M = v/C_s$) is shown as a function of radial coordinate (r). The dotted (black) curve depicts accretion solution that joins the black hole horizon with the outer edge of the disk $r_{\rm edge} = 500$ and transiting through the inner critical point at $r_{\rm in} = 1.452$ with angular momentum $\lambda_{\rm in} = 1.980$, $\alpha = 0.01$ and $\Phi_{\rm s} = 0.0$ while accreting onto a black hole of spin $a_{\rm k} = 0.99$. For this solution, we note the relevant flow variables at the outer boundary as $\lambda_{\rm edge}$, $v_{\rm edge}$, and $\Theta_{\rm edge}$. Interestingly, when the integration (equations (3.11) and (3.12)) is carried toward the horizon utilizing the aforementioned outer boundary values, an identical solution (S_1) is achieved. We calculate the local specific energy (hereafter energy) of the flow as $\mathcal{E} = (v^2/2) + \log(h) + \Phi_{\rm e}^{\rm eff}$ and at $r_{\rm edge}$ yielding $\mathcal{E}_{\rm edge} = 1.0036$. Subsequently, thermal conduction effects are incorporated by setting $\Phi_{\rm s} = 0.0025$ while keeping the remaining model parameters unchanged at $r_{\rm edge}$ as $\lambda_{\rm edge} = 3.294$, $\mathcal{E}_{\rm edge} = 1.0036$, $\alpha = 0.01$, and obtained global transonic accretion solutions by suitably tuning $v_{\rm edge}$ and $\Theta_{\rm edge}$. The thermal conduction parameter lies within the range $0 \leq \Phi_S < 1$. However, based on the self-similar approach, previous studies (Shadmehri, 2008; Ghoreyshi & Shadmehri, 2020, and references therein) reported that for large values of Φ_S, the accretion flow tends to become non-rotating (angular velocity $\Omega \to 0$), and the condition $H/r < 1$ is violated (Riffert & Herold, 1995; Peitz & Appl, 1997). Due to this, we begin with this order of Φ_s. This need to be added here. The resulting solution is plotted using a dashed curve

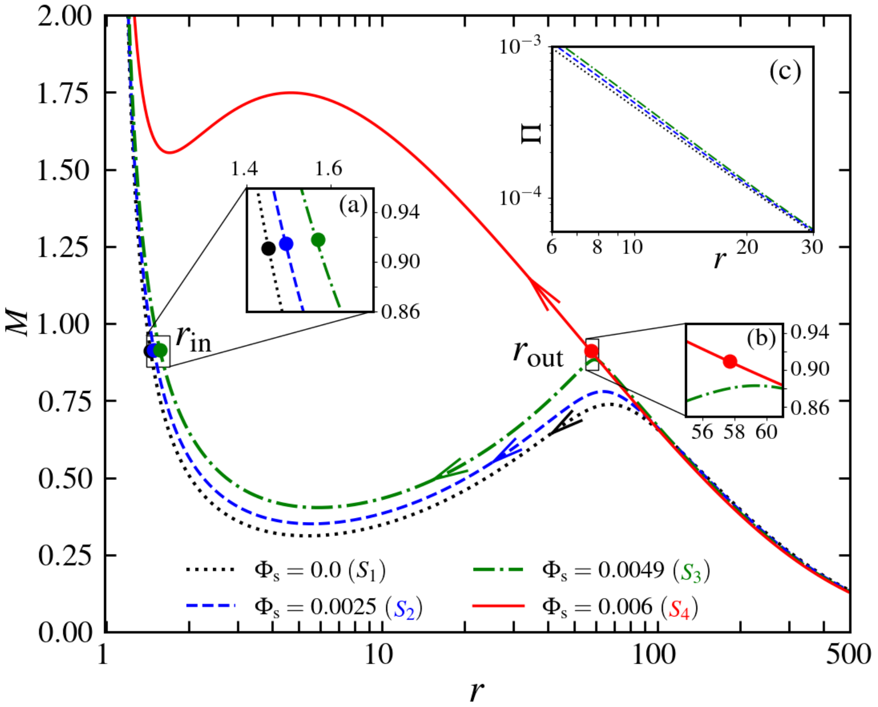

Figure 3.1: Illustrations of Mach number ($M = v/C_{\rm s}$) of the accreting flow as function of radial coordinate (r) for different conduction parameters ($\Phi_{\rm s}$). Flows are injected from the outer edge of the disk with $r_{\rm edge} = 500$ with $\lambda_{\rm edge} = 3.294$, $\mathcal{E}_{\rm edge} = 1.0036$, and $\alpha = 0.01$ onto a black hole of spin $a_{\rm k} = 0.99$. Flow solutions represented here using dotted (black), dashed (blue), and dot-dashed (green) are obtained for $\Phi_{\rm s} = 0.0$ (S_1), 0.0025 (S_2) and 0.0049 (S_3), while solid (red) curve denotes solution corresponding to $\Phi_{\rm s} = 0.006$ (S_4). Critical points are depicted ($r_{\rm in}$ and $r_{\rm out}$) in the figure. Insets (a) and (b) show the zoomed locations of the critical points for clarity, and inset (c) illustrates the pressure profiles. See the text for details.

(S_2, blue) that traverses the inner critical point at $r_{\rm in} = 1.507$. Notably, $r_{\rm in}$ is shifted outward with increasing $\Phi_{\rm s}$ (see inset (a)), and these findings are consistent with the results reported by Mitra et al. (2023). Upon increasing the saturation constant ($\Phi_{\rm s}$), we continue to obtain the analogous solutions containing $r_{\rm in}$ up to the threshold value $\Phi_{\rm s} = 0.0049$ (shown as S_3, dot-dashed in green). Exceeding this critical value, the global accretion solution alters its characteristics as it passes through the outer critical point ($r_{\rm out}$) rather than the inner critical point ($r_{\rm in}$). An example of such a solution is obtained for $\Phi_{\rm s} = 0.006$, which passes through $r_{\rm out} = 57.691$ (see inset (b) for clarity).

The solution S_4 is demonstrated in the figure with a solid (red) curve. The aforementioned results depict that thermal conduction serves as a critical factor in governing the characteristics of accretion solutions, particularly in determining whether the flow transits through $r_{\rm in}$ or $r_{\rm out}$. The comprehensive details of the flow variables evaluated at the critical point ($r_{\rm in}$ or $r_{\rm out}$) and the outer edge of the disk ($r_{\rm edge}$) for these global transonic

Table 3.1: Details of the flow variables corresponding to the global transonic solutions presented in Figure 3.1. In column $2-10$, conduction parameter ($\Phi_{\rm s}$), critical point location ($r_{\rm c}$), angular momentum at $r_{\rm c}$ ($\lambda_{\rm c}$), velocity at $r_{\rm c}$ ($\upsilon_{\rm c}$), temperature at $r_{\rm c}$ ($\Theta_{\rm c}$), outer edge of the disk ($r_{\rm edge}$), angular momentum at $r_{\rm edge}$ ($\lambda_{\rm edge}$), velocity at $r_{\rm edge}$ ($\upsilon_{\rm edge}$), temperature at $r_{\rm edge}$ ($\Theta_{\rm edge}$) are presented. See the text for details.

Solution	$\Phi_{\rm s}$	$r_{\rm c}$ ($r_{\rm g}$)	$\lambda_{\rm c}$ ($r_{\rm g}c$)	$\upsilon_{\rm c}$ c	$\Theta_{\rm c}$ ($m_{\rm e}c^2/k_{\rm B}$)	$r_{\rm edge}$ ($r_{\rm g}$)	$\lambda_{\rm edge}$ ($r_{\rm g}c$)	$\upsilon_{\rm edge}$ c	$\Theta_{\rm edge}$ ($m_{\rm e}c^2/k_{\rm B}$)
S_1	0.0	1.452	1.980	0.3611	161.567	500	3.294	0.006898	1.67759
S_2	0.0025	1.507	1.953	0.3642	165.545	500	3.294	0.006770	1.67784
S_3	0.0049	1.570	1.928	0.3647	165.993	500	3.294	0.006653	1.67807
S_4	0.006	57.691	1.955	0.0816	5.244	500	3.294	0.006547	1.67827

accretion solutions are tabulated in Table 3.1. Furthermore, we compute the total pressure (Π) of the accretion solutions S_1, S_2 and S_3 and expressed the corresponding results in the inset (c). We find that for a fixed r, Π increases with $\Phi_{\rm s}$. This occurs because of the fact that increased saturated conduction parameter ($\Phi_{\rm s}$) facilitates more heat flow from the inner hotter regions. Consequently, this results in a local increase in both temperature and gas pressure (Tanaka & Menou, 2006).

Since the behaviour of the accretion solutions passing through the inner ($r_{\rm in}$) and outer ($r_{\rm out}$) critical points is characteristically different, an investigation of the flow variable profiles for these solutions becomes essential. Subsequently, we compare the radial variation of the flow variables, namely the flow radial velocity (υ), the sound speed ($C_{\rm s}$), the temperature in Kelvin (T) and disk scale height (H/r), and expressed the obtained results in Figure 3.2, where the dashed (blue) and solid (red) curves depict the results corresponding to the accretion solutions S_2 and S_4 shown in Figure 3.1. We observe that υ of S_2 remains lower compared to the same of S_4 particularly in the subsonic region ($r \lesssim 100$), despite that both solutions start with comparable radial velocity from $r_{\rm edge} = 500$ as shown in panel (a). In order to maintain the conservation of mass flux (see equation (3.2)), the density (ρ) of the flow for S_2 increases, leading to an increase in both the radial profile of the sound speed ($C_{\rm s}$, panel (b)) and the flow temperature (T, panel (c)). This ultimately yields a higher disk-scale height H/r, causing a relatively thicker inner disk geometry for S_2.

Next, we examine another distinct characteristic feature of transonic accretion solutions around a rotating black hole. In Figure 3.3, we present the Mach number (M) profile of the accretion solution which passes through the inner critical point ($r_{\rm in}$) for various different conduction parameter values $\Phi_{\rm s}$. Here, we fix the model parameters at $r_{\rm in} = 1.667$ as $\lambda_{\rm in} = 1.903$, $\alpha = 0.01$ and $a_{\rm k} = 0.99$. In panel (a), we choose $\Phi_{\rm s} = 0.0$ and find that the subsonic accretion flow (S_5) from $r_{\rm edge} = 500$ plunges into the black hole supersonically after passing through the inner critical point. Subsequently, we increase the thermal conduction to $\Phi_{\rm s} = 0.006$ and due to the increased effect of thermal conduction, corresponding flow solution (S_6) becomes closed (see Das, 2007, for details) for the same

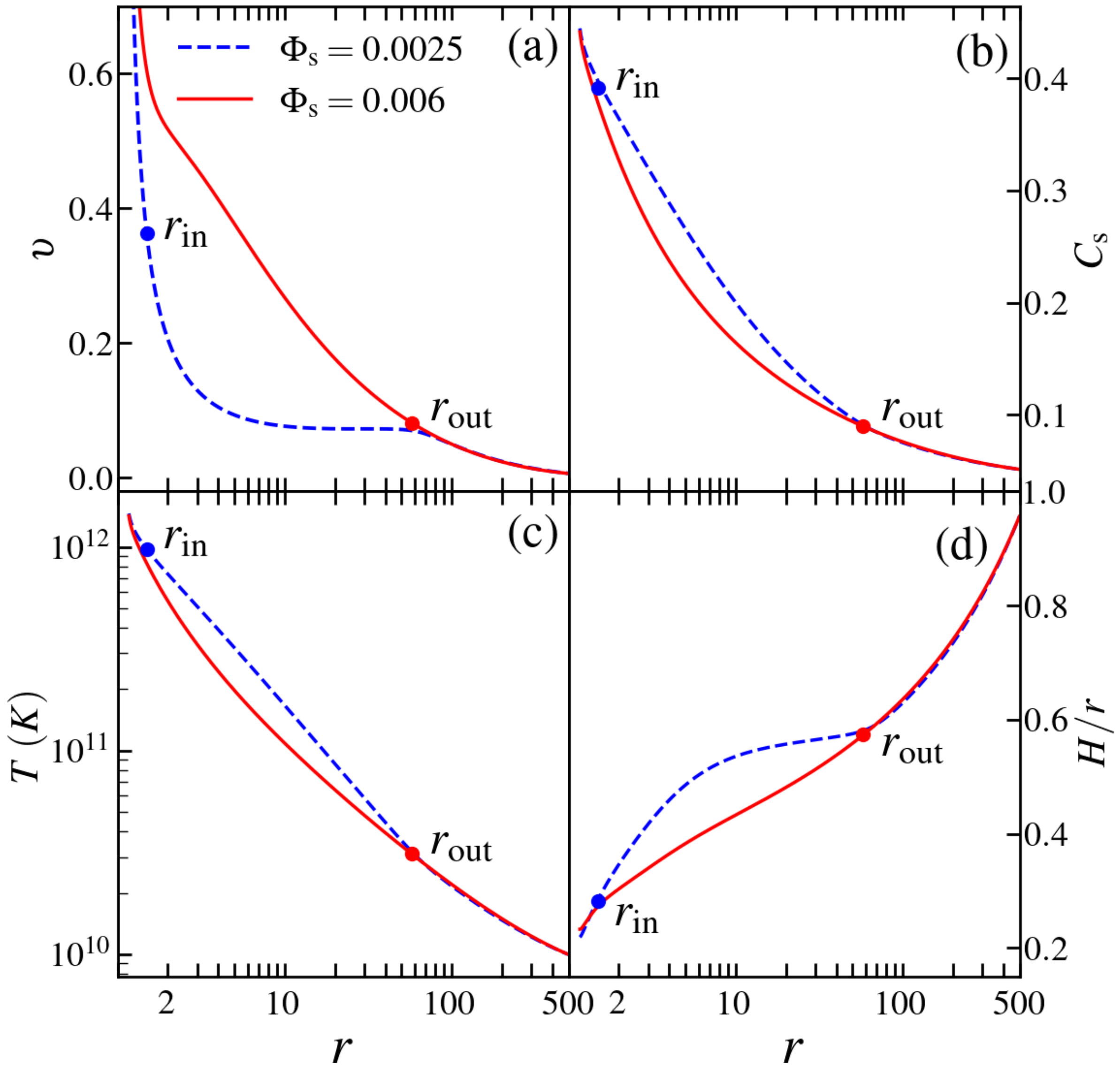

Figure 3.2: Plots of (a) radial velocity υ, (b) sound speed C_s, (c) temperature T, and (d) disk scale height H/r for solutions obtained for different Φ_s. Dashed (blue) and solid (red) curves depict results for solutions labeled S_2 and S_4 in Figure 3.1. Filled circles denote the locations of critical points (r_{in} and r_{out}). See the text for details.

set of model parameters, as shown in panel (b). These findings evidently indicate that for a given set of model parameters, there exists a critical saturation constant (Φ_s^{cri}) beyond which open solutions become closed. A comprehensive discussion of this critical saturation constant is thoroughly examined in Section 3.5. It is noteworthy that such a closed accretion solution is incapable of connecting the outer edge of the disk (r_{edge}) unless it joins with another accretion solution (similar to S_4 of Figure 3.1) via shock transition resulting in a shock-induced global accretion solution around a black hole (see section 3.3). As thermal conduction continues to increase gradually, the closed solution shrinks further, as illustrated in panel (c) for $\Phi_s = 0.03$ (S_7), and ultimately vanishes for $\Phi_s > 0.11$.

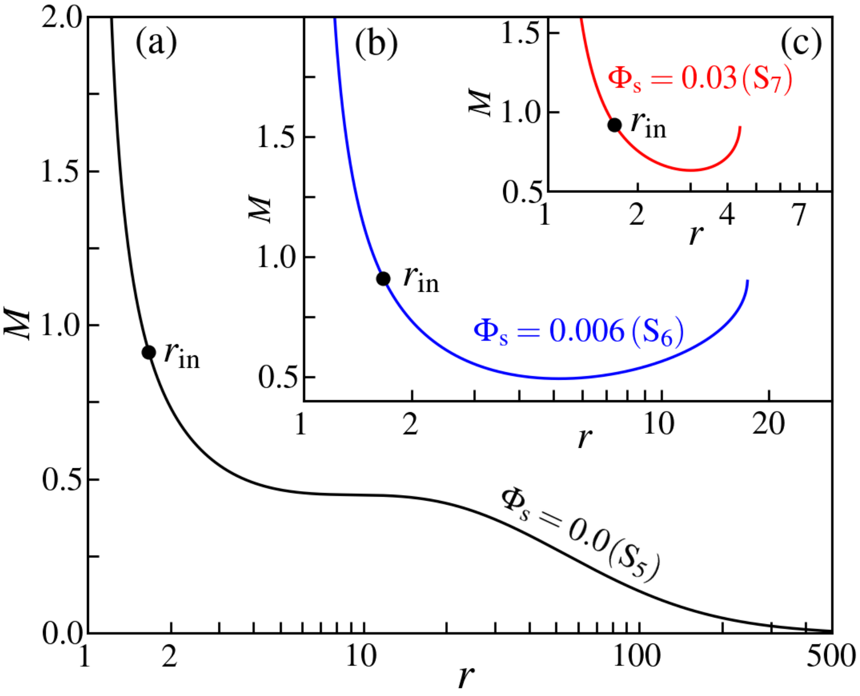

Figure 3.3: Modification of accretion solutions (M vs. r) passing through the inner critical point ($r_{\rm in}$) for different conduction parameter $\Phi_{\rm s}$. Here, we fix $r_{\rm in} = 1.667$, $\lambda_{\rm in} = 1.903$, $\alpha = 0.01$, and $a_{\rm k} = 0.99$. In panels (a), (b) and (c), results are obtained for $\Phi_{\rm s} = 0.0$, 0.006 and 0.03, respectively. See the text for details.

3.3 Shock-induced Global Accretion Solutions

As discussed in the previous section 3.2, rotating accretion flows around a black hole may harbour shock waves (Fukue, 1987; Chakrabarti, 1989; Chakrabarti & Das, 2004; Fukue, 2019; Dihingia et al., 2019a; Mitra & Das, 2024, and references therein) reminiscent of those reported in solar winds (Holzer & Axford, 1970). In a realistic scenario, subsonic accretion flow initially traverses through the outer critical point ($r_{\rm out}$) before continuing its supersonic journey towards the horizon. Meanwhile, rotating flow encounters centrifugal repulsion that eventually triggers the discontinuous transition of the flow variables at the subsonic branch in the form of shock waves. The post-shock flow gradually picks up its velocity and subsequently plunges into the black hole supersonically after passing through the inner critical point ($r_{\rm in}$). Indeed, the formation of the stationary shock is possible, provided that the Rankine-Hugoniot conditions (RHC) (Landau & Lifshitz, 1959) are satisfied. In this investigation, we employ RHCs across the shock front which are expressed as the conservation of (a) mass flux: $\dot{M}_{-} = \dot{M}_{+}$, (b) energy flux : $\mathcal{E}_{-} = \mathcal{E}_{+}$ and (c) momentum flux: $\Pi_{-} = \Pi_{+}$. Here, we treat the shock to be thin, and '$-$' and '$+$' denote the quantities measured across the shock front.

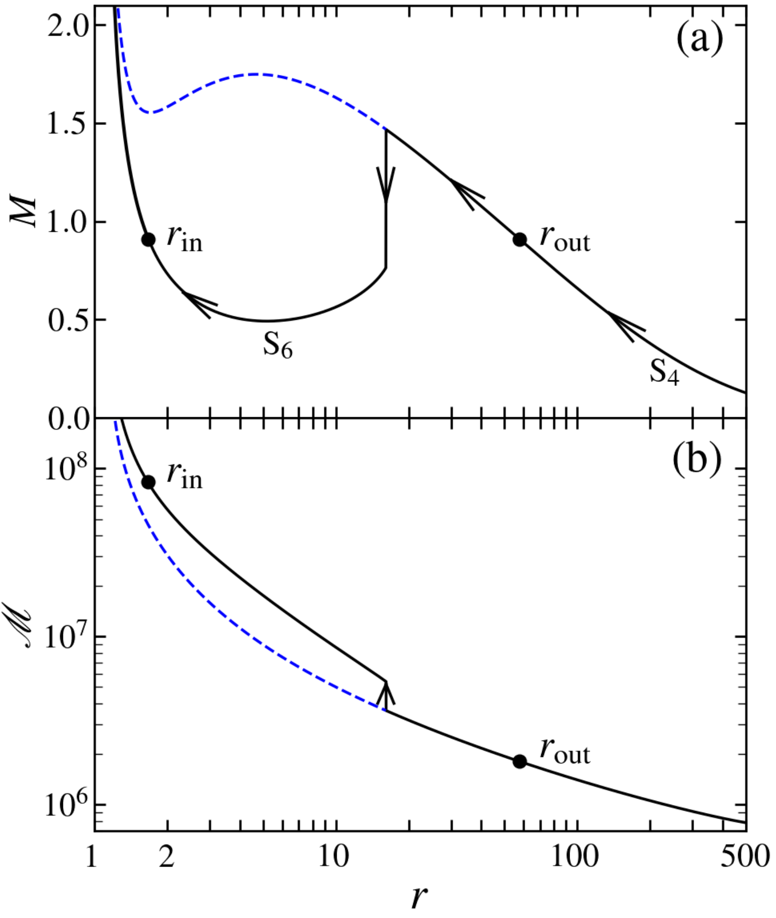

Figure 3.4: An illustration of a complete global accretion solution containing shock around a black hole. The variation of Mach number (M) with the radial coordinate (r) is shown in panel (a) for $\Phi_{\rm s} = 0.006$. Here, RHCs connect S_4 of Figure 3.1 and S_6 of Figure 3.3 at $r_{\rm s} = 16.142$ (vertical arrow) to yield shock-induced global accretion solution. In panel (b), the entropy accretion rate ($\dot{\mathcal{M}}$) is depicted with r for the accretion solution shown in panel (a). Filled circles denote the critical points ($r_{\rm in}$ and $r_{\rm out}$). See the text for details.

In Figure 3.4a, we demonstrate shock-induced global accretion solution around a rapidly rotating black hole ($a_{\rm k} = 0.99$) incorporating the effect of thermal conduction. We observe that a transonic accretion solution passing through $r_{\rm out} = 57.691$ (S_4 in Figure 3.1) encounters a shock transition at $r_s = 16.142$ as the RHCs are satisfied there leading to a jump into the subsonic branch of another solution (S_6 in Figure 3.3) avoiding dashed part of S_4 solution. Subsequently, the subsonic flow gradually gains speed as it progresses inwards and ultimately reaches the BH horizon supersonically after crossing the inner critical point $r_{\rm in} = 1.667$. This occurs because the entropy accretion rate ($\dot{\mathcal{M}}$) in the post-shock flow is greater than the pre-shock flow, as shown in Figure 3.4b, and high-entropy states solutions are thermodynamically preferred (Becker & Kazanas, 2001).

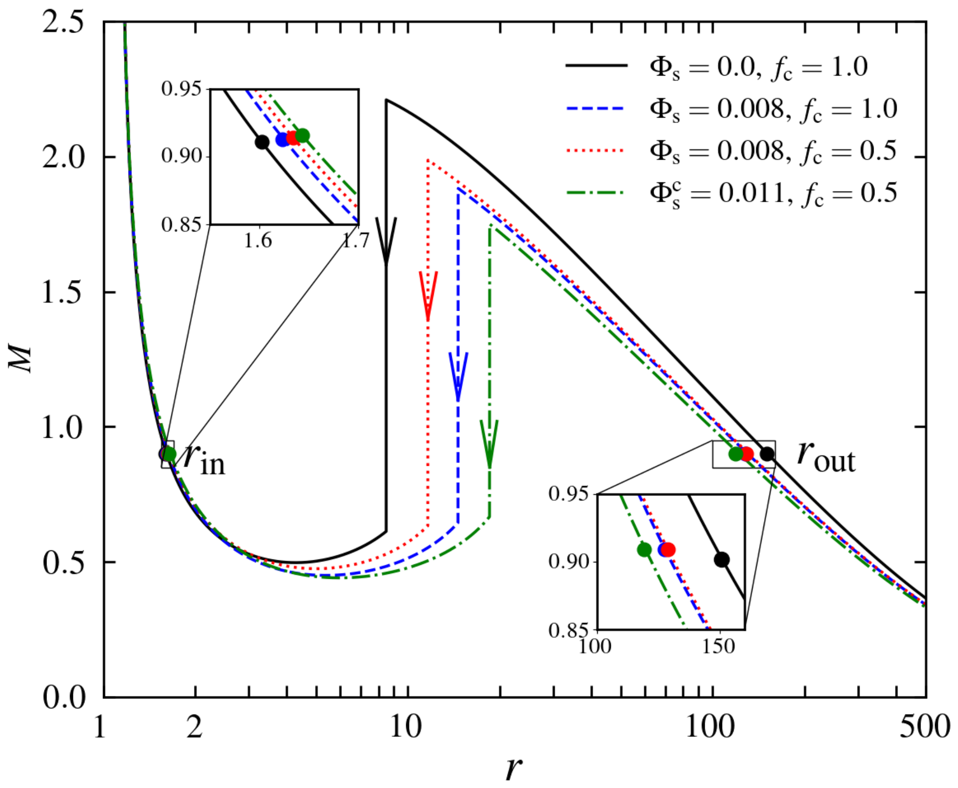

Figure 3.5: Variations of Mach number (M) with radial coordinate (r) for flows injected from $r_{\rm edge} = 500$ with $\lambda_{\rm edge} = 2.351$, $\mathcal{E}_{\rm edge} = 1.0015$, and $\alpha = 0.01$ for a rapidly rotating black hole of $a_{\rm k} = 0.99$. The conduction parameter ($\Phi_{\rm s}$) and cooling parameter ($f_{\rm c}$) are marked in the figure and the corresponding shock radii are obtained as $r_{\rm s} = 8.486$ (solid), 11.637 (dotted), 14.619 (dashed) and 18.548 (dot-dashed). Critical points are zoomed at the insets for clarity. See the text for details.

In the figure, the vertical line denotes the shock transition radius, while the arrows indicate the direction of the flow moving towards the black hole. Because of the shock compression, the convergent post-shock flow becomes hot and dense, forming a puffed-up inner disk (equivalently, post-shock corona, hereafter PSC (Aktar et al., 2017b)). We quantify density compression across the shock by calculating the compression ratio $R = \Sigma_+/\Sigma_-$, which yields $R = 1.68$. In addition, we calculate the shock strength ($S = M_-/M_+$), which determines the temperature jump across the shock, and obtain $S = 1.91$. When the soft photons from the cooler pre-shock flow interact with the hot electrons of the PSC, they undergo inverse Comptonization, resulting in the production of hard X-rays. This indicates that high energy radiation from black hole sources is intrinsically linked to PSC characteristics, *i.e.*, $r_{\rm s}$, R and S, respectively.

Since the shock radius governs the size of the PSC, it is useful to examine the effect of thermal conduction in influencing the shock formation around the rapidly rotating black hole. To elaborate on this, in Figure 3.5, we demonstrate how the shock radius varies due to the increase in the conduction parameter ($\Phi_{\rm s}$) for flows with fixed outer boundary. We

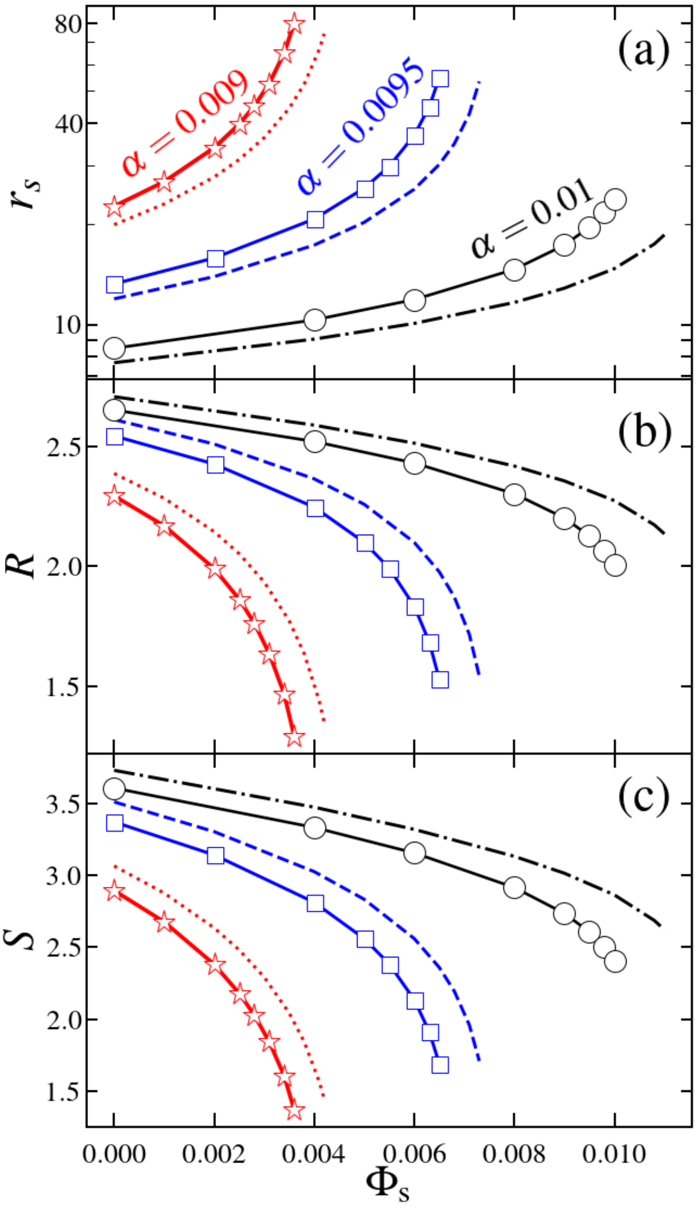

Figure 3.6: Plots of (a) shock radius r_s, (b) compression ratio R and (c) shock strength S varied with conduction parameter $\Phi_{\rm s}$ for different viscosity parameter α. Here, flows are injected from the fixed outer edge with $r_{\rm edge} = 500$ with same $\mathcal{E}_{\rm edge} = 1.0015$ and $\lambda_{\rm edge} = 2.351$. Results for $\alpha = 0.009$, 0.0095, and 0.01, respectively, when cooling is not present ($f_{\rm c} = 1.0$), are shown by asterisks, squares, and circles connected by solid lines. Similarly, findings for $\alpha = 0.009$, 0.0095, and 0.01 are represented by dotted, dashed, and dot-dashed curves in the presence of cooling ($f_{\rm c} = 0.5$). See the text for details.

Table 3.2: Details of the shock-induced global accretion solution in presence of thermal conduction. Column $1-9$ refer conduction parameter ($\Phi_{\rm s}$), cooling parameter ($f_{\rm c}$), inner critical point ($r_{\rm in}$), angular momentum at $r_{\rm in}$ ($\lambda_{\rm in}$), outer critical point ($r_{\rm out}$), angular momentum at $r_{\rm out}$ ($\lambda_{\rm out}$), shock radius ($r_{\rm s}$), compression ratio (R), and shock strength(S) for shocked solutions presented in Figure 3.5. See the text for details.

$\Phi_{\rm s}$	$f_{\rm c}$	$r_{\rm in}$ ($r_{\rm g}$)	$\lambda_{\rm in}$ ($r_{\rm g}c$)	$r_{\rm out}$ ($r_{\rm g}$)	$\lambda_{\rm out}$ ($r_{\rm g}c$)	$r_{\rm s}$ ($r_{\rm g}$)	R	S
0.0	1.0	1.602	1.932	150.549	2.037	8.486	2.65	3.60
0.008	1.0	1.622	1.9106	127.644	2.003	14.619	2.30	2.91
0.008	0.5	1.633	1.9109	128.759	2.004	11.637	2.41	3.13
0.011	0.5	1.643	1.901	119.085	1.987	18.548	2.13	2.62

inject matter subsonically from $r_{\rm edge} = 500$ with $\mathcal{E}_{\rm edge} = 1.0015$, $\lambda_{\rm edge} = 2.351$, $\alpha = 0.01$, and $f_{\rm c} = 1.0$ onto a black hole of spin $a_{\rm k} = 0.99$. For $\Phi_{\rm s} = 0.0$, the flow crosses the outer critical point at $r_{\rm out} = 150.549$ and becomes supersonic and undergoes a shock transition at $r_{\rm s} = 8.486$ (solid vertical arrow) as the RHCs are satisfied there. Here, we obtain $R = 2.65$ and $S = 3.60$. As the thermal conduction is turned on ($\Phi_{\rm s} = 0.008$) keeping the other model parameters fixed, we observe that the shock front moves outward and it settles down to a shock radius at $r_{\rm s} = 14.619$ as depicted using dashed vertical arrow. Due to thermal conduction, the local thermal pressure of the accreting flow is enhanced (see Figure 3.1), which pushes the shock front outward to preserve the pressure balance across shock. For this shocked solution, we obtain $R = 2.30$ and $S = 2.91$. Next, we introduce the parametric cooling by setting $f_{\rm c} = 0.5$ and find that the shock radius is pushed towards the horizon, at $r_{\rm s} = 11.637$, as indicated by the dotted vertical arrow. This is not surprising, as cooling reduces the post-shock pressure, allowing the shock to move inward. When the conduction parameter is further increased to $\Phi_{\rm s} = 0.011$ with cooling ($f_{\rm c} = 0.5$), the shock front moves outward to $r_{\rm s} = 18.548$ (as shown by the dot-dashed vertical arrow), as anticipated. Above a critical value of conduction parameter $\Phi_{\rm s}^{\rm cri} = 0.011$, shock-induced solutions disappear as RHCs are not satisfied. These results clearly demonstrate that thermal conduction plays a significant role in shock formation within a dissipative accretion flow around rotating black holes. We tabulate the model parameters and the obtained shock properties in Table 3.2.

In Figure 3.6, we illustrate the variation of the shock properties, namely shock radius $r_{\rm s}$ (panel (a)), compression ratio R (panel (b)), and shock strength S (panel (c)), as function of conduction parameter $\Phi_{\rm s}$ for various viscosity parameters (α). Here, we fix the outer boundary parameters as $\mathcal{E}_{\rm edge} = 1.0015$, $\lambda_{\rm edge} = 2.351$ at $r_{\rm edge} = 500$ in all cases and choose $a_{\rm k} = 0.99$. In each panel, the asterisks, squares, and circles connected by solid lines represent results obtained for viscosity parameters $\alpha = 0.009$, 0.0095, and 0.01, respectively, with $f_{\rm c} = 1.0$. We observe that stationary shocks continue to form across a wide range of conduction parameters ($\Phi_{\rm s}$) in a viscous accretion flow around a rapidly rotating black hole. We also see that for a fixed α, shock radius moves further out with the increase of $\Phi_{\rm s}$, as the gas pressure is increased due to the increase in thermal conduction. Interestingly, once $\Phi_{\rm s}$ exceeds a critical value ($\Phi_{\rm s} > \Phi_{\rm s}^{\rm cri}$), the shock-induced accretion solutions disappear because the RHCs are no longer satisfied. Notably, $\Phi_{\rm s}^{\rm cri}$ does not have a universal value as it depends on the other model parameters (see Sect. 3.4). In addition, we see that for a given $\Phi_{\rm s}$, when the effect of viscosity is weak, shock forms at larger radii for flows with fixed energy and angular momentum at the outer edge. This happens because lower viscosity effectively reduces the outward transport of angular momentum, resulting in a stronger centrifugal barrier, and hence the shock front settles at larger radii. These observations suggest that shocks are mainly centrifugally supported. Next, we turn on the parametric cooling ($f_c = 0.5$), keeping the other model parameters unchanged, and find that shock forms at relatively smaller radii. The results are shown using dotted, dashed, and dot-dashed curves, which are obtained for $\alpha = 0.009$, 0.0095 and 0.01, respectively. Furthermore, $\Phi_{\rm s}^{\rm cri}$ is found to be higher for lower values of f_c, independent of the viscosity parameter α. In panels (b) and (c), we depict the variation of the compression ratio R and shock strength S as function of $\Phi_{\rm s}$ for the same set of model parameters used in panel (a). We observe that for fixed α, both R and S are decreased with the increase of $\Phi_{\rm s}$ regardless of whether cooling is present or absent. We observe a cut-off in R and S when shock ceases to exit for $\Phi_{\rm s} > \Phi_{\rm s}^{\rm cri}$.

3.4 Shock Parameter Space

As outlined in the previous section, shock formation persists in a dissipative accretion flow even in the presence of substantial thermal conduction. Hence, it is important to determine the ranges of model parameters that allow shock-induced global accretion solutions when thermal conduction is taken into account. We address this by examining the ranges of energy ($\mathcal{E}_{\rm in}$) and angular momentum ($\lambda_{\rm in}$) of the flow calculated at the inner critical point ($r_{\rm in}$) that render shocked solutions. This approach is particularly relevant, because, for a dissipative accretion flow around rapidly rotating black hole ($a_{\rm k} = 0.99$), the feasible ranges of the inner critical point and the angular momentum at the inner edge are exceedingly narrow ($r_{\rm in} \lesssim 2$; $1.5 \lesssim \lambda_{\rm in} \lesssim 3$; Chakrabarti, 1990b; Chakrabarti & Das, 2004). In Figure 3.7, we separate the region of the parameter space in $\lambda_{\rm in} - \mathcal{E}_{\rm in}$ plane that allows standing shocks in dissipative accretion flow and study how the shock parameter space alters for increasing conduction and cooling parameters ($\Phi_{\rm s}$, $f_{\rm c}$). Here, we fix $\alpha = 0.01$ and $a_{\rm k} = 0.99$. In the figure, conduction parameter ($\Phi_{\rm s}$) and cooling parameter ($f_{\rm c}$) are indicated, where the regions bounded with solid and dashed curves are obtained in absence ($f_{\rm c} = 1.0$) and presence ($f_{\rm c} = 0.5$) of cooling. The results demonstrate that increasing the conduction parameter ($\Phi_{\rm s}$) in the absence of parametric cooling shifts the effective region of the parameter space toward lower angular momentum and higher

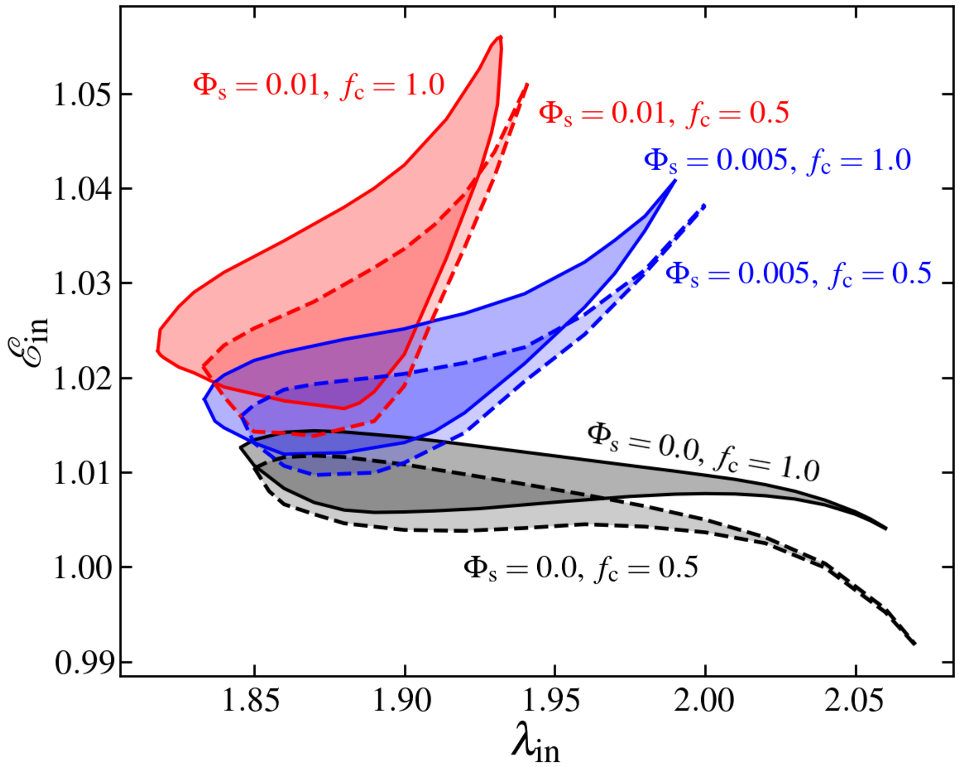

Figure 3.7: Modification of the shock parameter space for different sets of Φ_s and f_c. Effective regions bounded with solid and dashed curves are obtained in the absence and presence of cooling. Here, we fix $\alpha = 0.01$ and $a_k = 0.99$. See the text for details.

energy domains. This behaviour occurs because higher thermal conduction enhances the gas pressure, which in turn increases angular momentum transport (see equation (3.4) and (3.6)). When cooling is activated ($f_c = 0.5$) within the disk, the energy of the flow is reduced, causing the shock parameter space to migrate toward lower energy regions, as shown by the dashed curve.

3.5 Critical Conduction Parameter for Standing Shock

Our previous analysis has demonstrated that when the conduction parameter (Φ_s) exceeds a critical value ($\Phi_s > \Phi_s^{\rm cri}$), the accretion flow does not undergo shock transition because RHCs become unfavourable. Indeed, $\Phi_s^{\rm cri}$ exhibits significant dependence on the other model parameters. Therefore, we calculate $\Phi_s^{\rm cri}$ as function of black hole spin (a_k), considering both cases with and without cooling. Here, we keep the viscosity parameter fixed as $\alpha = 0.01$, and energy ($\mathcal{E}_{\rm in}$) and angular momentum ($\lambda_{\rm in}$) are treated as free parameters at the inner critical point ($r_{\rm in}$). The obtained results are depicted in Figure 3.8a, where open circles joined with solid lines illustrate the variation of $\Phi_s^{\rm cri}$ corresponding to $f_c = 1.0$, whereas open squares connected with dotted lines refer to the same for

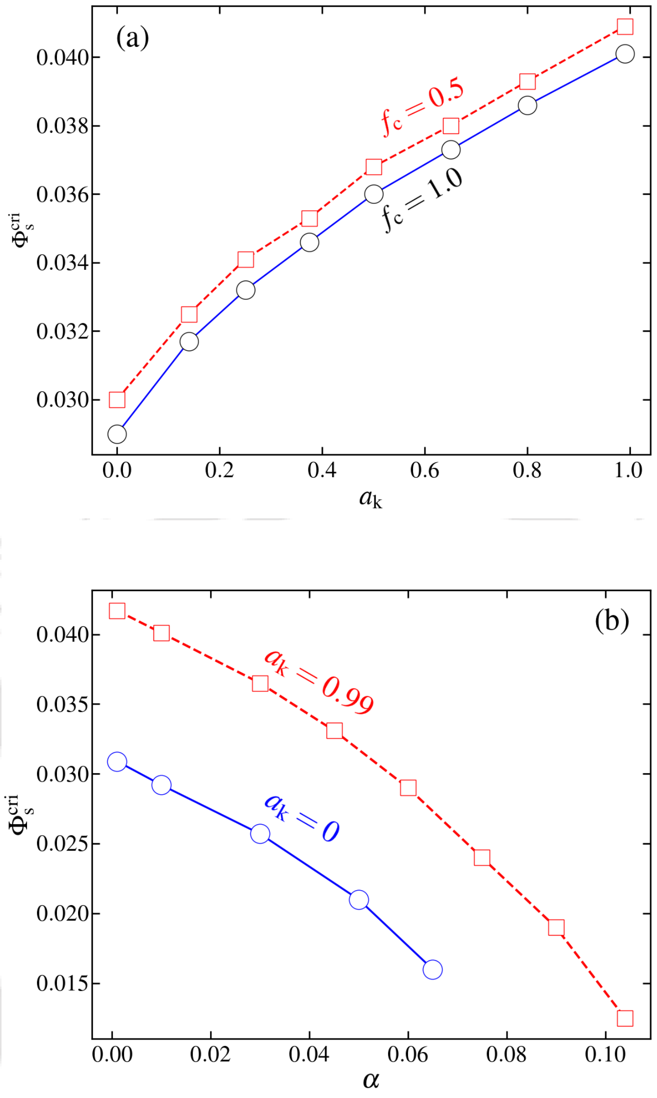

Figure 3.8: Panel (a): Variation of Φ_s^{cri} with black hole spin (a_k) for flows with $\alpha = 0.01$. Open circles and squares joined with solid and dashed lines denote results in absence ($f_c = 1.0$) and presence ($f_c = 0.5$) of cooling. Panel (b): Variation of Φ_s^{cri} with viscosity parameter (α) for different a_k values. Open circles and squares joined with solid and dashed lines are for non-rotating ($a_k = 0.0$) and rapidly rotating ($a_k = 0.99$) black holes, respectively. Here, we choose $f_c = 1.0$. See the text for details.

$f_c = 0.5$. The figure evidently indicates that shock-induced global accretion solutions continue to persist for a wide range of Φ_s, and Φ_s^{cri} increases with a_k. Moreover, our findings reveals that the critical conduction parameter Φ_s^{cri} consistently exhibits higher values when cooling is active within the flow. In particular, we find that in absence of cooling $f_c = 1.0$, $\Phi_s^{cri} = 0.029$ (0.0401) for non-rotating black hole of $a_k = 0.0$ (rapidly rotating black hole of $a_k = 0.99$). Similarly, when cooling is present $f_c = 0.5$, we obtain $\Phi_s^{cri} = 0.03$ (0.0409) for $a_k = 0.0$ (0.99). These findings suggest that dissipative accretion flows around rapidly rotating black holes continue to harbour shocks even in the presence of higher thermal conduction and vice versa.

Furthermore, we conduct a comprehensive investigation of how thermal conduction influences the possibility of shock transitions in dissipative accretion flows characterised by different viscosity parameter α. In doing so, we follow the same approach delineated above, and obtain $\Phi_{\rm s}^{\rm cri}$ for increasing values of α keeping the black hole spin ($a_{\rm k}$) fixed. Here, we choose $f_{\rm c} = 1.0$, disregarding any cooling effects. The obtained results are illustrated in 3.8b, where open circles joined with solid line are for $a_{\rm k} = 0.0$, and open squares connected with dashed lines are for $a_{\rm k} = 0.99$. We find that $\Phi_{\rm s}^{\rm cri}$ monotonically decreases with the increase of α irrespective to $a_{\rm k}$ values. This occurs because the combined effects of thermal conduction and viscosity maintain the level of dissipation favourable to trigger the shock transition inside the accretion flow around rotating black holes. We also observe that shocks disappear at relatively lower viscosity ($\alpha = 0.065$) for non-rotating black holes ($a_{\rm k} = 0$), while for rapidly rotating ($a_{\rm k} = 0.99$) black holes, shocks persist even at higher values as $\alpha = 0.104$.

3.6 Chapter Conclusion

In this Chapter, we address the first comprehensive investigation of the effects of thermal conduction on the shock-induced viscous advective accretion flows around non-rotating ($a_{\rm k} = 0$) as well as rapidly rotating ($a_{\rm k} = 0.99$) black holes in the presence of parametric cooling. We adopt a pseudo-Kerr effective potential which satisfactorily describes the spacetime geometry around a rotating black hole, and consider the relativistic equation of state (REoS). We solve the hydrodynamical governing flow equations and study the role of thermal conduction in triggering the shock transition and influencing its characteristics, namely shock radius ($r_{\rm s}$), compression ratio (R) and shock strength (S), respectively. The main findings of this work are summarised below.

- We self-consistently obtain the global transonic accretion solutions around rotating black holes, taking into account the effects of thermal conduction. We observe that, depending on the conduction parameter ($\Phi_{\rm s}$), the accretion flow with a fixed outer boundary either passes through the inner ($r_{\rm in}$) or the outer ($r_{\rm out}$) critical point before plunging into the black hole (see Figure 3.1).

- We also observe that for a given set of model parameters ($\mathcal{E}$, λ, α, and $a_{\rm k}$), an increase in the conduction parameter pushes the shock to form farther from the black hole horizon. When cooling is activated, the shock front moves inward as the post-shock flow is cooled down due to the rise in the cooling, leading to a reduction in thermal pressure and causing the shock front to settle down at smaller radii (see Figure 3.5).

- The characteristics of the post-shock flow (*i.e.*, PSC), such as its size, temperature, and density, explicitly depend on the shock radius ($r_{\rm s}$), compression ratio (R) and shock strength (S). We find that these quantities are eventually controlled by thermal conduction (see Figure 3.6). Since PSC properties are regulated by $\Phi_{\rm s}$, we argue that thermal conduction seems to play important role in influencing the spectral properties of black holes.

- Furthermore, for different $\Phi_{\rm s}$ and $f_{\rm c}$, we delineate the effective region of the parameter space spanned by $\lambda_{\rm in}$ and $\mathcal{E}_{\rm in}$ that exhibits transonic global accretion solutions embedding shocks around rapidly rotating black holes (see Figure 3.7). The analysis reveals that the parameter space alters due to the increase of conduction parameter ($\Phi_{\rm s}$) and cooling parameter ($f_{\rm c}$). It is important to mention that thermal conduction and parametric cooling have opposing effects on determining the parameter space for standing shock.

- We determine the critical conduction parameter ($\Phi_{\rm s}^{\rm cri}$), beyond which shocked accretion solutions no longer exist. We observe that $\Phi_{\rm s}^{\rm cri}$ varies with $a_{\rm k}$, where, in absence of cooling, $\Phi_{\rm s}^{\rm cri} = 0.0401$ for a rapidly rotating black hole ($a_{\rm k} = 0.99$) and $\Phi_{\rm s}^{\rm cri} = 0.029$ for a non-rotating black hole ($a_{\rm k} = 0$). In addition, we find that $\Phi_{\rm s}^{\rm cri}$ is higher when cooling is present compared to the scenario without cooling. Furthermore, for a fixed $a_{\rm k}$, $\Phi_{\rm s}^{\rm cri}$ is seen to decrease monotonically with the increase of viscosity parameter α (see Figure 3.8).

Finally, we acknowledge the limitations of this study, as it is developed based on certain assumptions. For simplicity, we adopt parametric cooling (Narayan & Yi, 1994) instead of incorporating realistic radiative processes, such as bremsstrahlung, synchrotron, and Compton cooling. We neglect the effects of magnetic fields and do not account for mass loss from the accretion disk. Indeed, all these physical processes are relevant in the context of the accretion disk dynamics.

Effect of thermal conduction on accretion shocks in relativistic magnetized flows around rotating black holes

4

> *"...The opposite of a fact is falsehood, but the opposite of one profound truth may very well be another profound truth......"*
>
> *Niels Bohr*

In Chapters 2 and 3, we have demonstrated the roles of viscosity and thermal conduction on transonic properties and dynamics of shock wave in accretion flow around both non-rotating and rapidly rotating black holes. However, in Chapter 1, we discuss the importance of the magnetic field in scenarios where the magnetic field controls the dynamics of the accretion flow. In particular, the magnetic field indeed plays a governing role along with both viscosity (Hawley et al., 1995; King et al., 2007; Sorathia et al., 2012) and thermal conduction (Tanaka & Menou, 2006; Sharma et al., 2008; Faghei, 2012; Ghoreyshi & Shadmehri, 2020) in accretion solutions. Due to the presence of the magnetic field, the thermal conduction effect becomes anisotropic (Sharma et al., 2008; Mosallanezhad et al., 2022). Furthermore, magnetic field also alters the synchrotron cooling in accretion around black holes (Shapiro & Teukolsky, 1983; Rybicki & Lightman, 1986). Therefore, the magnetic field seems to be one of the key parameter which controls the structure and dynamics of the accretion flow. However, Mitra & Das (2024) has shown the significant influence of radial magnetic flux on shock properties in the accretion flow around the BHs. Furthermore, Datta et al. (2022) discussed the role of various components of the magnetic field, i.e., B_r, B_ϕ and B_z, on the rate of transport of angular momentum. Although The

---

The contents of this chapter are published in Singh et al. (2025)

Event Horizon Telescope Collaboration et al. (2021b) has shown that the accretion flow is threaded by the magnetic field but evidence of which component is dominated is still a question because of Faraday's rotation and other effects. Therefore, all the components of the magnetic field have an impact on the accretion flow dynamics. Nonetheless, presence of toroidal magnetic field can be justified due to the differential rotation and frozen in field condition. Therefore, we extend the previous Chapter's work, and here, we consider that accretion flow is threaded by toroidal magnetic fields. This need to be added here In addition, in the previous chapter, we consider the parametric cooling (f_c). In this work, we take into account the realistic synchrotron and bremsstrahlung cooling mechanisms. Hence, this study focuses on the interplay between various dissipative mechanisms, such as viscosity, thermal conduction and magnetic field on the shock-induced global transonic accretion flow around black holes. In doing so, the gravitational field is approximated using the pseudo-potential formulation (Dihingia et al., 2018a). Moreover, we employ a relativistic equation of state (REoS) that effectively accounts for the thermodynamic properties of the accretion flow (Chattopadhyay & Ryu, 2009). Using this framework, we derive the shock-induced global accretion solutions and investigate key shock properties, such as shock location ($r_{\rm s}$), compression ratio (R), and shock strength (S), while examining their dependence on thermal conduction and magnetic fields. We find that the shock properties, such as shock radius ($r_{\rm s}$), compression ratio (R), and shock strength (S), are regulated by thermal conduction parameter ($\Phi_{\rm s}$), plasma-β ($\beta = P_{\rm gas}/P_{\rm mag}$, $P_{\rm gas}$ and $P_{\rm mag}$ denote the gas and magnetic pressure, respectively) , and viscosity parameter (α). Furthermore, we compute the critical conduction parameter ($\Phi_{\rm s}^{\rm cri}$), a threshold beyond which shock formation ceases to exist, and investigate its dependence on plasma-β and α for both non-rotating ($a_{\rm k} = 0$) and rapidly rotating ($a_{\rm k} = 0.99$) black holes. Finally, we examine the spectral energy distribution (SED) of the accretion disk and observe that increased thermal conduction and magnetic field strength lead to enhanced luminous emission spectra from black hole sources.

4.1 Governing equations and methodology

We consider a magnetized, viscous, advective, and axisymmetric low angular momentum accretion flow around a rotating black hole in the presence of thermal conduction. We adopt cylindrical coordinate system (r, ϕ, z) and assume that the flow maintains hydrostatic equilibrium in the vertical (z) direction. With this, we describe the governing equations that dictate the motion of the accretion flow around rotating black holes as:

$$\upsilon\frac{d\upsilon}{dr}+\frac{1}{h\rho}\frac{dP}{dr}+\frac{d\Phi_{\rm e}^{\rm eff}}{dr}+\frac{\langle B_\phi^2\rangle}{4\pi r\rho}=0, \tag{4.1}$$

$$\dot{M}=2\pi\upsilon\Sigma\sqrt{\Delta}, \tag{4.2}$$

$$\upsilon\frac{d\lambda}{dr}+\frac{1}{\Sigma r}\frac{d}{dr}(r^2T_{r\phi})=0, \tag{4.3}$$

$$\frac{\upsilon}{\rho(\Gamma-1)}\left(\frac{dP_{\rm gas}}{dr}-\frac{\Gamma P_{\rm gas}}{\rho}\frac{d\rho}{dr}\right)=\Lambda-\frac{1}{r\rho}\frac{d(rF_{\rm s})}{dr}-\alpha r(P/\rho+\upsilon^2)\frac{d\Omega}{dr}, \tag{4.4}$$

$$\nabla\times\left(\vec{\upsilon}\times\langle B_\phi\rangle\hat{\phi}-\frac{4\pi}{c}\eta\vec{j}\right)=0, \tag{4.5}$$

where υ is the radial velocity, ρ is the mass density, h is the enthalpy, B_ϕ denotes the azimuthal component of magnetic fields, and '$\langle\,\rangle$' indicates the azimuthal average. Here, η depicts the resistivity, and j is the current density (Oda et al., 2007). The total isotropic pressure P is the sum of the gas pressure ($P_{\rm gas}$) and magnetic pressure ($P_{\rm mag}$) with $P_{\rm gas}=R\rho T/\mu$, R, T and μ being the universal gas constant, local flow temperature and mean molecular weight, respectively. In this investigation, we choose $\mu=0.5$ for fully ionized plasma. Further, we calculate $P_{\rm mag}=\frac{\langle B_\phi^2\rangle}{8\pi}$ and rewrite the total pressure as $P=P_{\rm gas}(1+1/\beta)$, where the plasma-β parameter is defined as $\beta=P_{\rm gas}/P_{\rm mag}$. In equation (4.1), $\Phi_{\rm e}^{\rm eff}$ is the effective potential on the equatorial plane due to a rotating black hole, which is given by (Dihingia et al., 2018a),

$$\Phi_{\rm e}^{\rm eff}=1+\frac{1}{2}\ln\left[\frac{r\Delta}{a_{\rm k}^2(r+2)-4a_{\rm k}\lambda+r^3-\lambda^2(r-2)}\right], \tag{4.6}$$

where λ and $a_{\rm k}$ represent the specific angular momentum of the flow and spin of the black hole, respectively, and $\Delta=r^2-2r+a_{\rm k}^2$.

In equation (4.2), $\dot{M}$ denotes the mass accretion rate, which remains constant throughout the flow. The mass accretion rate is defined as $\dot{m}=\dot{M}/\dot{M}_{\rm Edd}$, where $\dot{M}_{\rm Edd}=1.44\times10^{17}(M_{\rm BH}/M_\odot)$ gm s^{-1}, and $M_\odot$ is the solar mass. Here, Σ corresponds to the vertically integrated surface mass density of the accreting matter given by $\Sigma=2\rho H$ (Matsumoto et al., 1984), where H is the local half-thickness of the disk. We evaluate H as described in (Riffert & Herold, 1995; Peitz & Appl, 1997) and is given by,

$$H=\sqrt{\frac{Pr^3(1-\lambda\Omega)}{\rho}\times\frac{(r^2+a_{\rm k}^2)^2-2\Delta a_{\rm k}^2}{(r^2+a_{\rm k}^2)^2+2\Delta a_{\rm k}^2}}, \tag{4.7}$$

where Ω is angular velocity of the flow and is expressed as,

$$\Omega=\frac{2a_{\rm k}+\lambda(r-2)}{a_{\rm k}^2(r+2)-2a_{\rm k}\lambda+r^3}.$$

In equation (4.3), we incorporate the vertically integrated total stress, which is predominantly dominated by the $r\phi$ component of the Maxwell stress $T_{r\phi}$, surpassing the contributions from the other components. For an advective flow with substantial radial velocity, following Machida et al. (2006), we calculate $T_{r\phi}$ as, $T_{r\phi} = \frac{\langle B_r B_\phi \rangle}{4\pi} H = -\alpha(W + \Sigma v^2)$, where W is the vertically integrated pressure and α is a constant that controls the viscous effect inside the disk.

In this work, we assume that the flow is cooled through both bremsstrahlung and synchrotron processes. The bremsstrahlung and synchrotron rates (in units of erg cm^{-3} s^{-1}) are expressed as (Shapiro & Teukolsky, 1983; Rybicki & Lightman, 1986; Wardziński & Zdziarski, 2000),

$$Q^{\rm brem} = 1.4 \times 10^{-27} n_e^2 T_e^{1/2} (1 + 4.4 \times 10^{-10} T_e),$$
$$Q^{\rm syn} = \frac{16}{3} \frac{n_e e^2}{c} \left(\frac{eB}{m_e c}\right)^2 \left(\frac{k_B T_e}{m_e c^2}\right)^2,$$

where, n_e is electron number density, T_e is the electron temperature, e is the electron charge, m_e is the electron mass, k_B is the Boltzmann constant and B is the magnetic fields. Consequently, we obtain the dimensionless total cooling rate as $\Lambda = (Q^{\rm brem} + Q^{\rm syn})/\rho \times (GM_{\rm BH}/c^5)$. Following Cowie & McKee (1977) and Tanaka & Menou (2006), we estimate the saturated conduction flux as $F_{\rm s} = 5\Phi_{\rm s}\rho \left(\frac{P_{\rm gas}}{\rho}\right)^{3/2}$, where $\Phi_{\rm s}$ is the dimensionless saturated conduction parameter (hereafter conduction parameter) lies in the range $0 \leq \Phi_{\rm s} < 1$. And, Γ is the adiabatic index of the accreting gas.

Equation (4.5) describes the advective transport of toroidal magnetic field through the azimuthally averaged induction equation. Because of the large scale of the accretion, the Reynolds number is typically high, permitting the exclusion of the magnetic diffusion term. Furthermore, we also neglect the dynamo term and assume that the azimuthally averaged toroidal magnetic fields approach zero at the surface. As a result, the toroidal magnetic flux rate is given as,

$$\dot{\Phi} = -4\pi v H B_0(r), \tag{4.8}$$

where $B_0(r)$ is the azimuthally averaged toroidal magnetic field confined to the disk equatorial plane. The magnetic flux $\dot{\Phi}$ is not conserved in the accretion flow and may vary inversely with the radial distance r. Following Machida et al. (2006) and Oda et al. (2007), we consider $\dot{\Phi} \propto r^{-\zeta}$, where ζ is a parameter that depicts the magnetic flux advection rate. Incorporating these considerations into account, the parametric relation for the magnetic flux rate is given by,

$$\dot{\Phi}(r, \zeta, \dot{M}) = \dot{\Phi}_{\rm edge}(\dot{M}) \left(\frac{r}{r_{\rm edge}}\right)^{-\zeta},$$

where $\Phi_{\rm edge}$ is the advection rate of toroidal magnetic flux measured at the outer edge of the disk ($r_{\rm edge}$). In this work, we consider $\zeta = 1$ unless stated otherwise.

Closure of the flow equations is accomplished via the relativistic equation of state (REoS) that relates the internal energy (ϵ), $P_{\rm gas}$ and ρ of the accretion flow. For this purpose, we adopt the REoS proposed by Chattopadhyay & Ryu (2009), which is given by,

$$\epsilon = \frac{\rho f}{\left(1 + \frac{m_p}{m_e}\right)}, \tag{4.9}$$

with

$$f = \left[1 + \Theta\left(\frac{9\Theta + 3}{3\Theta + 2}\right)\right] + \left[\frac{m_p}{m_e} + \Theta\left(\frac{9\Theta m_e + 3m_p}{3\Theta m_e + 2m_p}\right)\right], \tag{4.10}$$

where m_p is the mass of the ions and Θ $(= k_B T/m_e c^2)$ is the dimensionless temperature. Using REoS, we obtain the polytropic index as $N = (1/2)(df/d\Theta)$ and the adiabatic index $\Gamma = (1 + N)/N$. Subsequently, we define the sound speed as $C_\mathrm{s} = \sqrt{\Gamma P_\mathrm{gas}/(\epsilon + P_\mathrm{gas})} = \sqrt{2\Gamma\,\Theta/(f + 2\Theta)}$.

We simplify equations (4.1)-(4.5) to obtain the wind equation along with the radial derivatives of Θ, λ and β as,

$$\frac{d\upsilon}{dr} = \frac{\mathcal{N}(r, \upsilon, \lambda, \Theta, \beta)}{\mathcal{D}(r, \upsilon, \lambda, \Theta, \beta)}, \tag{4.11}$$

$$\frac{d\Theta}{dr} = \Theta_1 + \Theta_2 \frac{d\upsilon}{dr}, \tag{4.12}$$

$$\frac{d\lambda}{dr} = \lambda_1 + \lambda_2 \frac{d\upsilon}{dr}, \tag{4.13}$$

$$\frac{d\beta}{dr} = \beta_1 + \beta_2 \frac{d\upsilon}{dr}. \tag{4.14}$$

In equations (4.11, 4.12, 4.13, 4.14), the explicit expressions for the quantities $\mathcal{N}$, $\mathcal{D}$, Θ_1, Θ_2, λ_1, λ_2, β_1, and β_2 are mathematically extensive. Therefore, we provide them in the Appendix-C.

In order to obtain the global accretion solution, we simultaneously solve equations (4.11, 4.12, 4.13, 4.14) (Das, 2007; Sarkar & Das, 2016; Das & Sarkar, 2018; Singh & Das, 2024, and references therein). In doing so, we consider mass accretion rate ($\dot{m}$), viscosity parameter (α), black hole spin (a_k), and conduction parameter (Φ_s) as global parameters, since these quantities remain constant all throughout. During accretion, the subsonic flow begins its journey from the outer edge of the (r_edge) and gradually moves toward the black hole. As it progresses, the flow reaches the critical point (r_c), where it makes smooth transition to supersonic state before entering the black hole. Due to the inherently transonic nature of black hole accretion, the flow must pass through the critical point (r_c). Hence, we choose the same methodology as in previous Chapters. However, we have the magnetic induction equation as well, which was not there for the hydrodynamical cases. Therefore, we choose r_c as the reference radius (r_ref) and supply plasma-β (β_c) along with the angular momentum (λ_c) at r_c as local flow parameters. Employing the model parameters, we carry out the critical point analysis and apply l'Hôpital's rule to compute the radial velocity gradient, which takes the form $(d\upsilon/dr)_\mathrm{c} = 0/0$ at r_c. We then solve $\mathcal{N}(r, \upsilon, \lambda, \Theta, \beta) = 0$ and $\mathcal{D}(r, \upsilon, \lambda, \Theta, \beta) = 0$ to find radial velocity (υ_c) and temperature (Θ_c) at r_c. Subsequently, using these flow variables at r_c, we integrate equations (4.11), (4.12), (4.13), and (4.14) up to horizon (r_h) and then to the outer edge of the (r_edge).

Finally, we join these two parts of the solution to obtain the global accretion solution. Afterwards, we note the flow variables at $r_{\rm edge}$ as energy $\mathcal{E}_{\rm edge}$, angular momentum $\lambda_{\rm edge}$, plasma-$\beta_{\rm edge}$, radial velocity $\upsilon_{\rm edge}$, and temperature $\Theta_{\rm edge}$. It is important to mention that the same global accretion solution can also be derived using the outer boundary flow variables mentioned above. In the following sections, we continue to present our results based on these outer boundary flow variables.

Depending on the model parameters, the flow may contain either single or multiple critical points. Notably, accretion flows with multiple critical points are of particularly noteworthy, as they can undergo shock transitions provided Rankine-Hugoniot shock conditions (RHCs)[2] are satisfied. In reality, rotating matter experiences centrifugal repulsion in the vicinity of the black hole, resulting in an accumulation of matter that forms an effective boundary layer around it. However, this accumulation cannot persist indefinitely, as it leads to discontinuous transitions in the flow variables, manifesting as shock waves at its threshold. This shock transition is consistent with the second law of thermodynamics, as it is characterized by a higher entropy state of the accreting matter (Becker & Kazanas, 2001). Due to shock compression, the density and temperature of the convergent flow sharply increase downstream, just after the shock transition, resulting in a hot and dense post-shock flow (hereafter referred to as the post-shock corona, PSC). As a result, the PSC serves as an ideal environment for reprocessing soft photons from the pre-shock flow into high energy X-ray radiation through the inverse Comptonization process. These high energy X-rays are commonly observed from black hole X-ray binary (BH-XRB) sources (Chakrabarti & Titarchuk, 1995; Mandal & Chakrabarti, 2005; Nandi et al., 2012; Iyer et al., 2015; Nandi et al., 2018; Majumder et al., 2022, and references therein).

4.2 Results

Figure 4.1 presents an illustrative example of a shock-induced global magnetized accretion solution around a rotating black hole in presence of thermal conduction. In panel (a), we show the variation of Mach number ($M = \upsilon/C_{\rm s}$) with radial coordinate (r). Here, we choose $\dot{m} = 0.0001$, $\alpha = 0.01$ and $\Phi_{\rm s} = 0.01$, and inject flow subsonically from the outer edge of the disk at $r_{\rm edge} = 500$, characterized by angular momentum $\lambda_{\rm edge} = 2.266$, energy $\mathcal{E}_{\rm edge} = 1.00105$, plasma-$\beta_{\rm edge} = 80$ on to a super massive black hole of mass $M_{\rm BH} = 4.3 \times 10^6\ {\rm M}_\odot$ and spin $a_{\rm k} = 0.99$. The flow becomes supersonic after passing through the outer critical point at $r_{\rm out} = 180.28$ with angular momentum $\lambda_{\rm out} = 2.056$,

---

[2] RHCs are the conservation of (a) mass flux $\dot{M}_+ = \dot{M}_-$, (b) energy flux $\mathcal{E}_+ = \mathcal{E}_-$, (c) momentum flux $W_+ + \Sigma_+ v_+^2 = W_- + \Sigma_- v_-^2$ and (d) magnetic flux $\dot{\Phi}_+ = \dot{\Phi}_-$ across the shock front (Landau & Lifshitz, 1959; Sarkar & Das, 2016; Das & Sarkar, 2018; Singh & Das, 2025; Jana & Das, 2024). Here, '$-/+$' refer upstream/downstream quantities across the shock front, while $\mathcal{E}$ $[= v^2/2 + \log h + \Phi_{\rm e}^{\rm eff} + \langle B_\phi^2 \rangle/(4\pi\rho)]$ depicts the local flow energy.

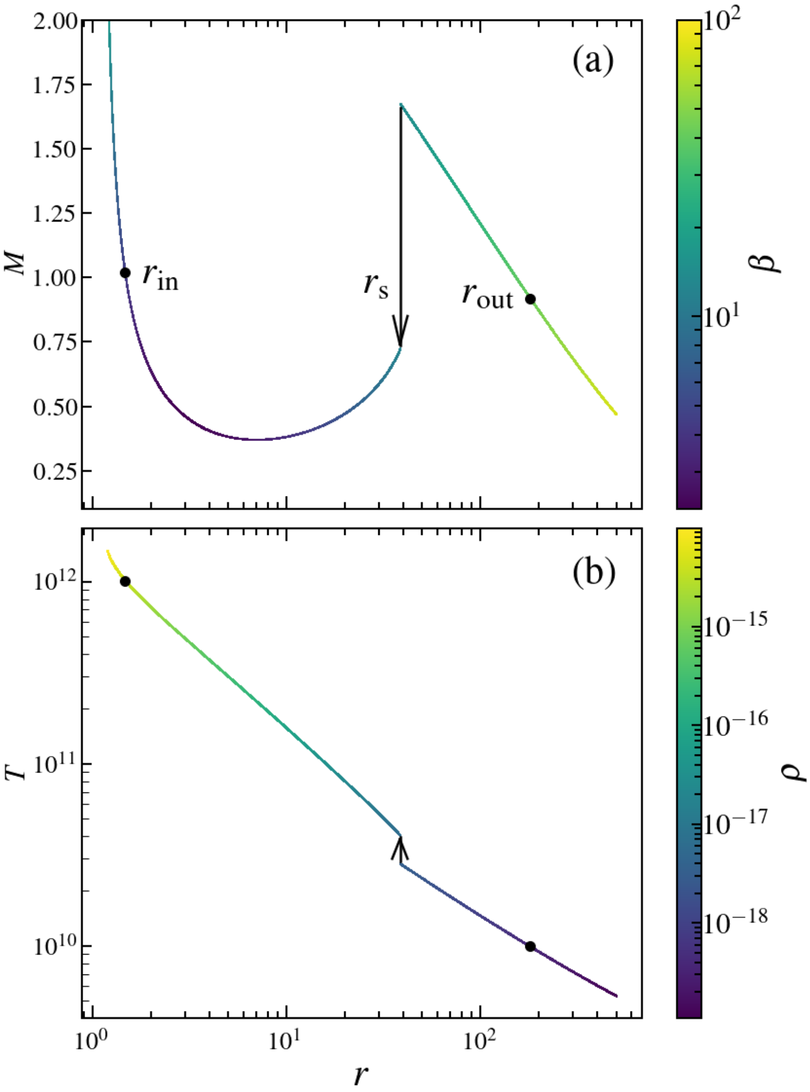

Figure 4.1: Illustration of a shock-induced global accretion solution, where in panel (a) we plot the variation of Mach number ($M = v/C_{\rm s}$) and plasma-β (in color) with radial coordinate (r), and panel (b) depicts the temperature (T) of the flow along with the density (ρ, in color). Here, flow is injected from the outer edge of the $r_{\rm edge} = 500$ with $\lambda_{\rm edge} = 2.266$, $\mathcal{E}_{\rm edge} = 1.00105$, $\beta_{\rm edge} = 80$, $\alpha = 0.01$, $\dot{m} = 0.0001$, $\Phi_{\rm s} = 0.01$, and $a_{\rm k} = 0.99$. Flow experiences shock transition at $r_{\rm s} = 38.37$ shown by the vertical arrow. Filled circles indicates the critical points ($r_{\rm in}$ and $r_{\rm out}$). Color bars in panels (a) and (b) refer the ranges of β and ρ. See the text for details.

and continues to accrete toward the horizon. Subsequently, RHCs become favorable, and the supersonic upstream flow undergoes a shock transition to the subsonic branch at $r_{\rm s} = 38.37$, depicted by the vertical arrow. In this study, we consider the shock to be thin and non-dissipative (Frank et al., 2002). Following the shock transition, the temperature of the downstream flow is increased as the kinetic energy of the upstream flow is converted into thermal energy in the downstream. Additionally, because of shock compression, the convergent flow becomes compressed, leading to an increase in density in the downstream

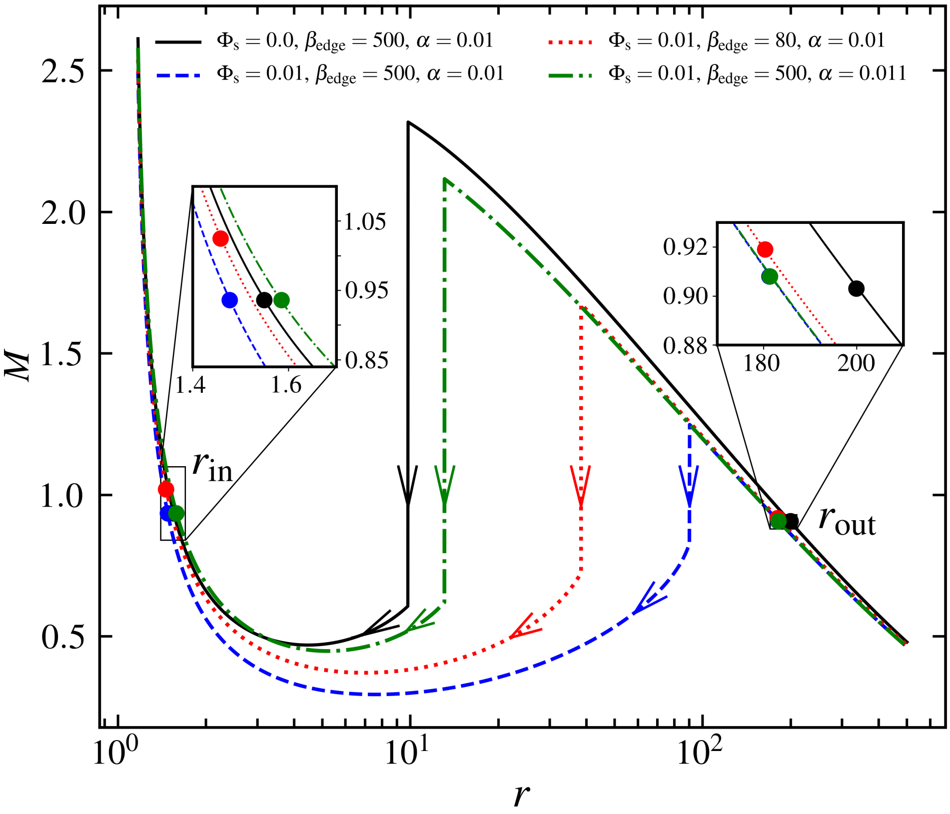

Figure 4.2: Plot of Mach number $M = v/C_s$ with the radial distance r. Flows of fixed $\mathcal{E}_{edge} = 1.00105$, $\lambda_{edge} = 2.266$ are injected from $r_{edge} = 500$ with distinct Φ_s, β_{edge} and α values. Here, $a_k = 0.99$ and $\dot{m} = 0.0001$. Vertical arrows depict the corresponding shock radii at $r_s = 9.82$ (solid), 90.24 (dashed), 38.37 (dotted) and 13.09 (dot-dashed). Inner (r_{in}) and outer (r_{out}) critical points are zoomed in on the insets for clarity. See the text for details.

flow (PSC). In Figure 4.1b, we show the temperature (T) profile of the global shocked accretion solution presented in Figure 4.1a, with density (ρ) variation indicated by colors. The range of the flow density is shown in the color bar on the right side of panel (b). The density compression across the shock front is characterized by the compression ratio, defined as $R = \Sigma_+/\Sigma_-$, whereas the temperature jump is measured by the shock strength, which is defined as $S = M_-/M_+$. For the shocked solution presented in Figure 4.1, we obtain $R = 1.93$ and $S = 2.31$.

Next, we investigate the comprehensive impact of viscosity, thermal conduction, and magnetic fields on the shock transition in accretion flows with a fixed outer boundary. In this analysis, we inject matter towards the black hole from the outer edge of the disk fixed at $r_{edge} = 500$ with local energy $\mathcal{E}_{edge} = 1.00105$ and angular momentum $\lambda_{edge} = 2.266$. The mass accretion rate is set to $\dot{m} = 10^{-4}$, and the Kerr parameter is chosen as $a_k = 0.99$. For parameters set $(\alpha,\ \beta_{edge},\ \Phi_s) = (0.01,\ 500,\ 0.0)$, the shock is formed at $r_s = 9.82$, as indicated by the vertical arrow and the shocked accretion flow solution is shown by the solid (black) curve in Figure 4.2. For this shock-induced solution, we obtain the

Table 4.1: Model parameters, flow variables and shock properties for shock-induced global accretion solutions presented in Figure 2.2 are tabulated. In columns $1-9$, conduction parameter ($\Phi_{\rm s}$), plasma-$\beta_{\rm edge}$, viscosity parameter (α), inner critical point ($r_{\rm in}$), angular momentum ($\lambda_{\rm in}$) at $r_{\rm in}$, plasma-$\beta_{\rm in}$, outer critical point ($r_{\rm out}$), angular momentum ($\lambda_{\rm out}$) at $r_{\rm out}$, plasma-$\beta_{\rm out}$, shock radius ($r_{\rm s}$), compression ratio (R), and shock strength (S) are presented. See the text for details.

$\Phi_{\rm s}$	$\beta_{\rm edge}$	α	$r_{\rm in}$ ($r_{\rm g}$)	$\lambda_{\rm in}$ ($r_{\rm g}c$)	$\beta_{\rm in}$	$r_{\rm out}$ ($r_{\rm g}$)	$\lambda_{\rm out}$ ($r_{\rm g}c$)	$\beta_{\rm out}$	$r_{\rm s}$ ($r_{\rm g}$)	R	S
0	500	0.01	1.549	1.944	20.195	199.91	2.070	274.711	9.82	2.74	3.81
0.01	500	0.01	1.477	1.947	27.328	181.25	2.054	266.812	90.24	1.39	1.50
0.01	80	0.01	1.458	1.949	4.531	180.28	2.056	42.512	38.37	1.93	2.31
0.01	500	0.011	1.582	1.915	25.770	181.36	2.039	267.013	13.09	2.55	3.40

compression ratio $R = 2.74$ and $S = 3.81$. The flow passes through both inner and outer critical points at $r_{\rm in} = 1.549$ and $r_{\rm out} = 199.91$, which are marked using filled circles. When thermal conduction is activated ($\Phi_{\rm s} = 0.01$) while keeping the other model parameters fixed, the shock front is pushed outward to $r_{\rm s} = 90.24$. This occurs because thermal conduction enhances the local thermal pressure, which in turn forces the shock to settle at a larger radius (Singh & Das, 2025). For this case, the flow exhibits the inner and outer critical points at $r_{\rm in} = 1.477$, and $r_{\rm out} = 188.25$, and $(R,\ S) = (1.39, 1.50)$, with the resulting solution depicted by the dashed (blue) curve. Subsequently, as the magnetic field strength is increased to $\beta_{\rm edge} = 80$ with $\Phi_{\rm s} = 0.01$ and $\alpha = 0.01$, we observe that the shock front moves toward the horizon as indicated by the dotted (red) vertical arrow at $r_{\rm s} = 38.37$. Here, the inner and outer critical points are at $r_{\rm in} = 1.458$, and $r_{\rm out} = 180.28$, and $(R,\ S) = (1.93, 2.31)$. This inward shift of the shock is expected, as the density and temperature in the PSC are higher than in the upstream flow. This results in more enhanced cooling, which reduces the thermal pressure, ultimately causing the shock to settle towards the horizon. Overall, it is evident that thermal conduction induces an effect opposite to the magnetic fields in determining the shock transitions. Finally, when viscosity increases ($\alpha = 0.011$) while maintaining $\Phi_{\rm s} = 0.01$ and $\beta_{\rm edge} = 500$, we find that the shock moves further inward to $r_{\rm s} = 13.09$, represented by the dotted green vertical arrow. The increased viscosity facilitates more efficient angular momentum transport, weakening the centrifugal repulsion and causing the shock to move inward. For this solution, we have the inner and outer critical points at $r_{\rm in} = 1.582$, and $r_{\rm out} = 180.36$, and $(R,\ S) = (2.55, 3.40)$. We tabulate the model parameters and shock properties in Table 4.1. With these results, we point out that the combined effects of thermal conduction, viscosity, and magnetic fields regulate the shock properties, including the size of the post-shock corona ($r_{\rm s}$), density compression (R) and temperature jump (S).

We proceed further to compare the size of the PSC by investigating the shock radius ($r_{\rm s}$) as a function of conduction parameter ($\Phi_{\rm s}$) for flows with varying viscosity (α)

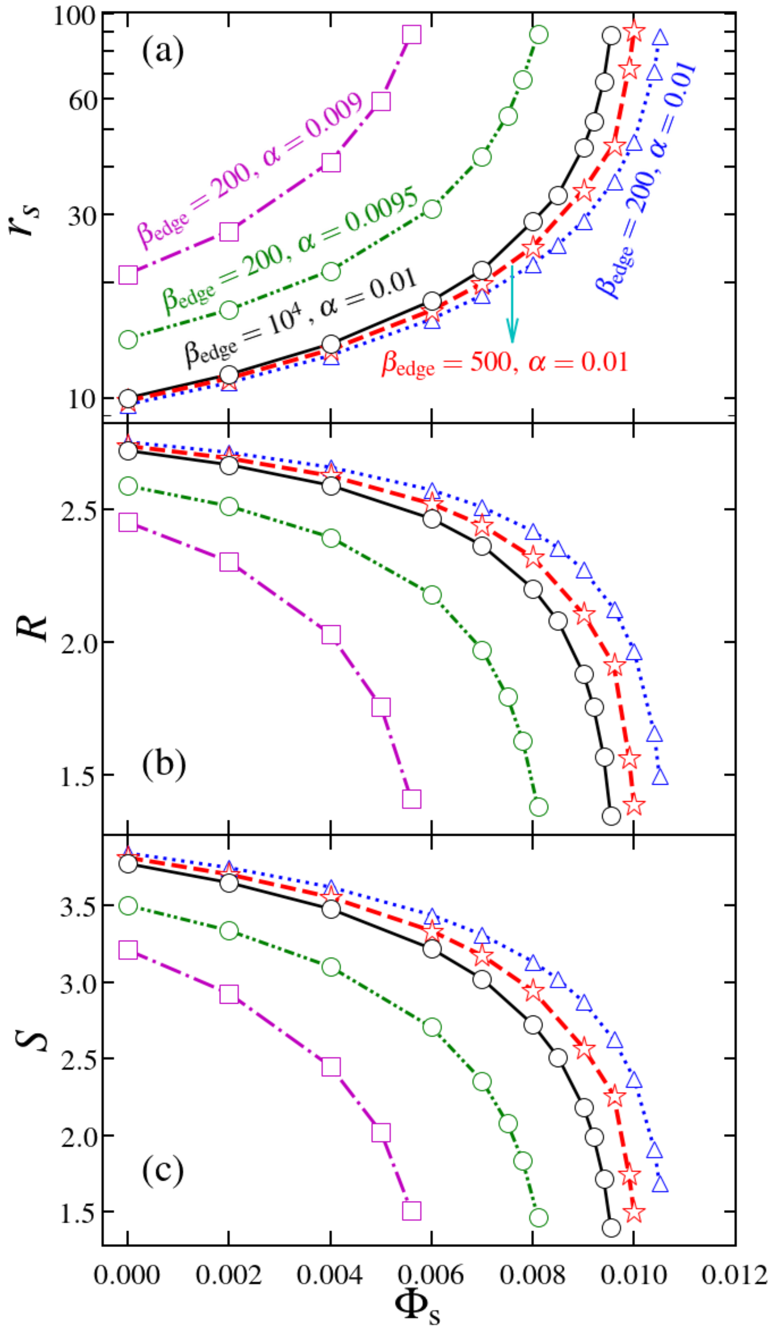

Figure 4.3: Plots of the shock properties varying with $\Phi_{\rm s}$ for different values of the $\beta_{\rm edge}$ and α. We illustrate the shock radius (r_s), compression ratio (R), and shock strength (S) in panels (a), (b), and (c), respectively. Here, we fix $\alpha = 0.01$, and $a_{\rm k} = 0.99$. See the text for details.

and magnetic field strengths ($\beta_{\rm edge}$). Here, matter is injected from $r_{\rm edge} = 500$ with $\mathcal{E}_{\rm edge} = 1.00105$ and $\lambda_{\rm edge} = 2.266$ onto a black hole with spin $a_{\rm k} = 0.99$. We begin with $\beta_{\rm edge} = 200$ at $r_{\rm edge} = 500$ and vary α. The obtained results are presented in Figure 4.3(a), where open squares, circles and triangles connected with dot-dashed, dot-dot-dashed, and dotted lines correspond to $\alpha = 0.009$, 0.0095 and 0.01, respectively. We observe that for a fixed $\beta_{\rm edge}$ and α, the shock radius $r_{\rm s}$ moves away from the horizon as $\Phi_{\rm s}$ is increased.

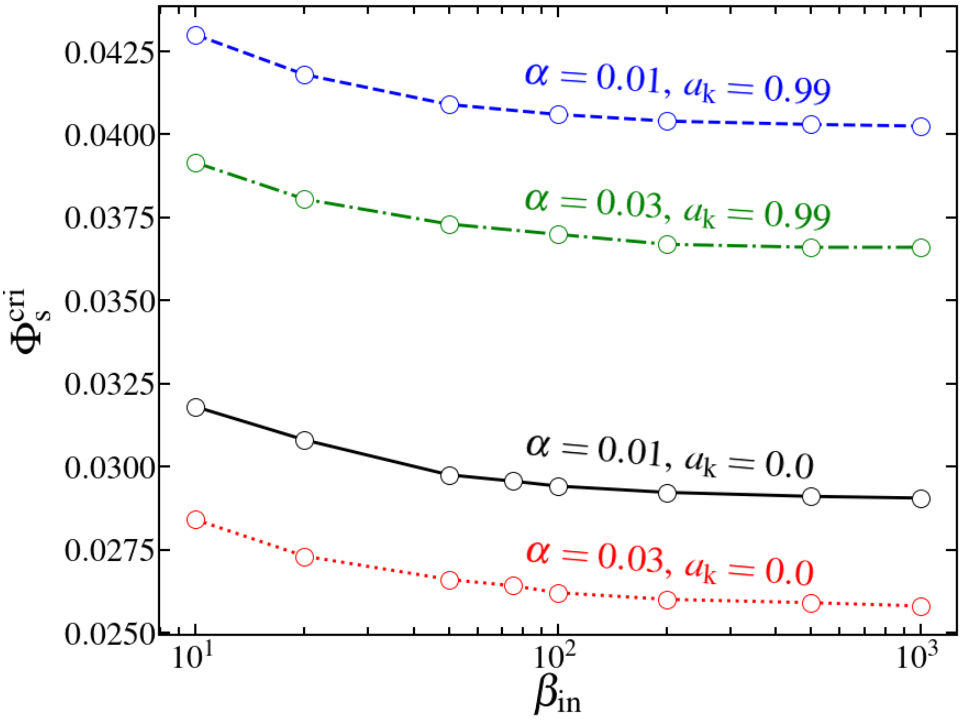

Figure 4.4: Variation of Φ_s^{cri} with the β_{in} for various different values of α for non-rotating ($a_k = 0.0$) and maximally rotating ($a_k = 0.99$) BHs. Here, Φ_s^{cri} is the limiting value of the Φ_s beyond which shock solutions vanish. See the text for details.

However, when thermal conduction exceeds its critical value, the shock disappears as RHCs become unfavourable. Furthermore, for a fixed Φ_s, as α increases, the shock moves down to a smaller radius due to the weakening of the centrifugal repulsion, which results from the more efficient outward angular momentum transport. Thereafter, we examine the effect of the magnetic field on shock dynamics. We see that for gas pressure dominated flow (*i.e.*, $\beta_{edge} = 10^4$) with $\alpha = 0.01$, the shock forms further from the black hole at a given Φ_s. As the magnetic field strength increases (*i.e.* β_{edge} decreases), the shock radius r_s proceeds towards the black hole. The open circles, asterisks, and triangles joined with solid (black), dashed (red), and dotted (blue) lines represent the variation of r_s with Φ_s for $\beta_{edge} = 10^4$, $\beta_{edge} = 500$, $\beta_{edge} = 200$, respectively. Indeed, high energy radiation flux emanating from the disk is primarily determined by radiative cooling processes, which exhibit strong dependence on the density ρ and temperature T distributions across the shock front (Chakrabarti & Titarchuk, 1995) Mandal & Chakrabarti (2005). Accordingly, in Figure 4.3b, we demonstrate the variation of the compression ratio (R), which measures the density compression across the shock, as a function of Φ_s for the shock-induced accretion solutions depicted in Figure 4.3a. As Φ_s increases, the shock generally moves away from the black hole horizon, causing the post-shock region to experience less compression and resulting in a decrease in the compression ratio R. Effectively, the shock becomes weaker in the presence of thermal conduction. In contrast, when β_{edge} decreases, the shock front moves inward toward the black hole, which results in enhanced compression of the PSC and, consequently, an increase in R. In addition, we also investigate the variation of shock strength S as a function of $\Phi_{\rm s}$ for the solutions shown in Figure 4.3a and observe that S decreases with the increase of thermal conduction, as indicated in Figure 4.3c. Based on these findings, it is evident that shock-induced global accretion solutions exist across a substantial range of $\Phi_{\rm s}$ for various values of $\beta_{\rm edge}$ and α. Notably, these shock driven accretion solutions have been successful in explaining the observed spectro-temporal characteristics of black hole X-ray binary sources, and demonstrated in numerous studies (Chakrabarti & Titarchuk, 1995; Chakrabarti & Manickam, 2000; Mandal & Chakrabarti, 2005; Nandi et al., 2012; Iyer et al., 2015; Das et al., 2021; Majumder et al., 2022; Nandi et al., 2024).

We have established that global shock-induced accretion solutions exist within a specific range of the conduction parameter $\Phi_{\rm s}$, which is limited by its critical value $\Phi_{\rm s}^{\rm cri}$. Importantly, $\Phi_{\rm s}^{\rm cri}$ does not exhibit a universal value; instead, it depends on the other model parameters. To investigate this, we determine $\Phi_{\rm s}^{\rm cri}$ for both non-rotating ($a_{\rm k} = 0$) and rapidly rotating ($a_{\rm k} = 0.99$) black holes, and examine its variation with the magnetic field strength at the inner critical point ($r_{\rm in}$). Since the inner critical points ($r_{\rm in}$) are located close to the horizon, it is reasonable to assume that the flow plunges into the black hole with magnetic fields (β) similar to those at the inner critical point $\beta_{\rm in}$. Hence, we investigate the variation of $\Phi_{\rm s}^{\rm cri}$ with $\beta_{\rm in}$ for different α values and demonstrate the findings in Figure 4.4. It is important to discuss that, while calculating $\Phi_{\rm s}^{\rm cri}$, we freely vary the remaining model parameters. We observe that $\Phi_{\rm s}^{\rm cri}$ increases as the magnetic field strength increaes (*i.e.* as $\beta_{\rm in}$ decreases) regardless of the black hole spin ($a_{\rm k}$). In addition, higher viscosity results in lower values of $\Phi_{\rm s}^{\rm cri}$. Furthermore, we see that for a given set of $(\beta_{\rm in}, \alpha)$, $\Phi_{\rm s}^{\rm cri}$ is larger for higher black hole spin $a_{\rm k}$ and smaller for lower $a_{\rm k}$.

Furthermore, we put efforts to calculate the monochromatic luminosity. For a convergent shocked accretion flow, we obtain,

$$L_\nu = 2\int_{r_{\rm edge}}^{r_{\rm h}}\int_0^{2\pi} Q_\nu^- Hr\, dr d\phi \;\; erg\, {\rm s}^{-1}{\rm Hz}^{-1}, \tag{4.15}$$

where Q_ν^- denotes the total emissivity from at a emission frequency ν. We calculate total emissivity through the contributions from both bremsstrahlung and synchrotron emissivities (Novikov & Thorne, 1973; Rybicki & Lightman, 1986; Wardziński & Zdziarski, 2000) as $Q_\nu^- = Q_\nu^{\rm syn} + Q_\nu^{\rm brem}$, which are given by,

$$Q_\nu^{\rm brem} = 6.8\times10^{-38} n_e^2 T_e^{-1/2}\times(1+4.4\times10^{-10}T_e)\exp\left(\frac{h\nu}{k_BT_e}\right), \quad \text{and}$$
$$Q_\nu^{\rm syn} = \frac{2^{1/6}\pi^{3/2}e^2n_e\nu}{3^{5/6}cK_2(1/\Theta)u^{1/6}}\exp\left[-\left(\frac{9u}{2}\right)^{1/3}\right],$$

where $u = 2\pi m_e c\nu/(eB\Theta^2)$, and $K_2(1/\Theta)$ is modified Bessel function of order two.

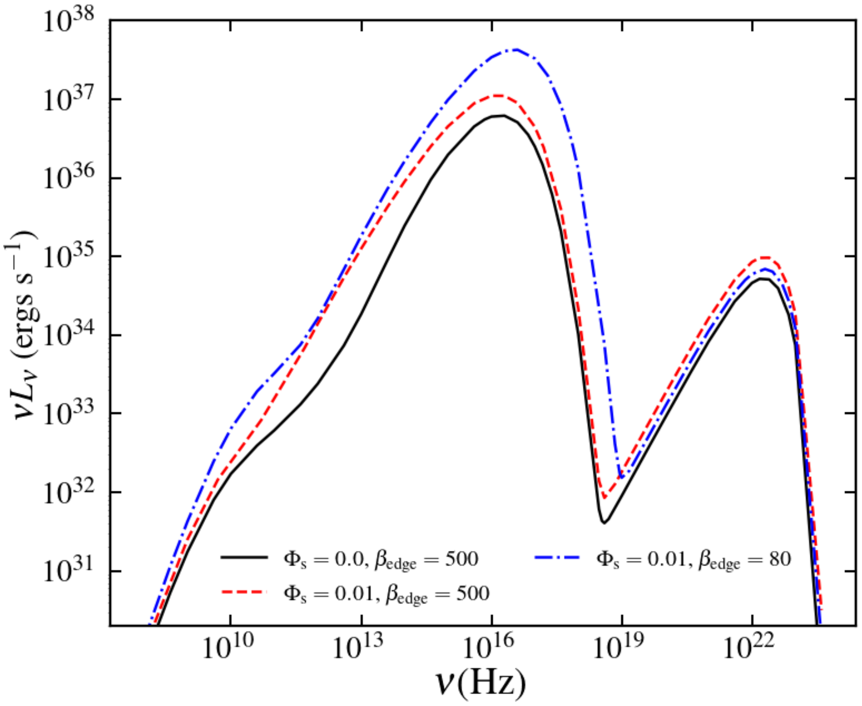

Figure 4.5: Plot of spectral energy distribution (SED) of accretion solutions for various conduction parameter ($\Phi_{\rm s}$) and plasma-β. Solid (black), dashed (red) and dot-dashed (blue) curves indicates results for $(\Phi_{\rm s}, \beta_{\rm edge}) = (0.0, 500)$, $(0.01, 500)$ and $(0.01, 80)$, respectively. See the text for details.

In the present study, we assume strong coupling between electrons and ions, which results in a single temperature accretion flow. Nevertheless, in a realistic scenario, electrons are much lighter than ions, the electron temperature (T_e) must be lower than the ion temperature ($T_i = T$), at least near the vicinity of the black hole. To account for this, we follow the work of (Chattopadhyay & Chakrabarti, 2000) and calculate the electron temperature as $T_e = \sqrt{(m_e/m_i)}T$, where m_i and m_e are the masses of ions and electrons, respectively. Using Eq. (4.15), we estimate the spectral energy distribution (SED) for three different shock-induced accretion solutions with varying $\Phi_{\rm s}$ and $\beta_{\rm edge}$ values. The results are demonstrated in Figure 4.5, where the variation of νL_ν with frequency ν is shown. Solid (black), dashed (red), and dot-dashed (blue) curves depict the results that correspond to $(\Phi_{\rm s}, \beta_{\rm edge}) = (0.0, 500)$, $(0.01, 500)$, and $(0.01, 80)$, respectively. We examine that for all cases, synchrotron photons dominate the lower energy part of the spectrum, with characteristic peaks around $\nu \sim 10^{16}$ Hz, while bremsstrahlung photons contribute to the high-energy part, peaking at $\nu \sim 10^{22}$ Hz. The spectra exhibit a sharp cutoff at $\nu \approx 10^{23}$ Hz, corresponding to an electron temperature $T_e \approx 10^{10}$ K at the inner edge $(r \sim r_{\rm h})$ of the disk. We observe that the peaks of the SEDs are largely remain unaffected to effect of the thermal conduction ($\Phi_{\rm s}$); however, the synchrotron peaks shift to higher frequencies as the flow becomes more magnetized (*i.e.*, smaller $\beta_{\rm edge}$). We also find that the SED is influenced by thermal conduction ($\Phi_{\rm s}$), which eventually enhances the disk luminosity. Notably, enhanced magnetic activity within the disk leads to more luminous spectra from the hot accreting plasma relative to weakly magnetized configurations. It is worth noting that, as our model framework is developed for low accretion rates, the resulting SED is potentially suited for radiatively inefficient accretion flows, including LLAGNs.

4.3 Chapter Conclusion

In this Chapter, we examine the effect of thermal conduction, viscosity and magnetic field on global, transonic, magnetized, viscous, advective accretion flows around rotating black holes in the presence of bremsstrahlung and synchrotron cooling processes. In this theoretical formalism, the accretion disk is permeated by the toroidal magnetic fields and the spacetime geometry is mimicked by the effective potential introduced by (Dihingia et al., 2018a). Furthermore, we utilize the relativistic equation of state (REoS). Within this framework, we solve the governing equations that describe the flow motion in accretion disk and obtain the shock-induced global transonic accretion for set of model parameters, namely accretion rate ($\dot{m}$), viscosity parameter (α), black hole spin ($a_{\rm k}$), conduction parameter ($\Phi_{\rm s}$), plasma-β, energy ($\mathcal{E}$) and angular momentum (λ) of the flow. We observe that magnetic fields and thermal conduction play a decisive role in regulating the shock phenomena, influencing shock location ($r_{\rm s}$), compression ratio (R), and shock strength (S), which in turn alters the emission spectrum of the disk. The key findings of this study are outlined as follows:

- We observe that global transonic magnetized accretion flows experience shock transitions when thermal conduction is present within the disk.
- Our investigation shows that both thermal conduction and magnetic fields play an indispensable role in shock formation. In particular, thermal conduction exerts an effect opposite to that of magnetic fields in determining the shock front dynamics (see Figure 4.2). In addition, we observe that shocks continue to persist in the accretion flow across a significant range of conduction parameter $\Phi_{\rm s}$ and plasma-β, including the viscosity parameter α. Hence, the shock transitions are facilitated by the combined effects of thermal conduction, viscosity, and magnetic fields. These factors comprehensively dictate the shock properties and determine the disk structure of the accretion flow. Moreover, we see that for all cases, strong shocks are formed when $\Phi_{\rm s}$ is small, with shock strength diminishing as $\Phi_{\rm s}$ increases (see Figure 4.3).
- We estimate the critical conduction parameter $\Phi_{\rm s}^{\rm cri}$ that permits global shocked magnetized accretion solutions around both non-rotating ($a_{\rm k} = 0$) as well as rapidly

rotating ($a_\mathrm{k} = 0.99$) black holes. Our results demonstrate that accretion flows around rapidly rotating black holes can accommodate higher values of $\Phi_\mathrm{s}^\mathrm{cri}$ compared to non-rotating black holes, irrespective of magnetic field strengths in the inner disk region (*i.e.*, plasma-β). Furthermore, for a fixed a_k and β_in, we find that $\Phi_\mathrm{s}^\mathrm{cri}$ is larger for weakly viscous flows and decreases with increasing viscosity (see Figure 4.4).

- We conclude the study by understanding the impact of the conduction parameter Φ_s and plasma-β on the disk emission spectrum (SEDs) resulting from the bremsstrahlung and synchrotron cooling processes. Our results suggest that the inclusion of thermal conduction enhances the emission spectrum. Moreover, we determine that increased magnetic activity also results in a more luminous emission spectrum (see Figure 4.5).

Finally, it is essential to acknowledge that the present theoretical framework relies on several simplifying approximations. We approximate the spacetime geometry using an effective pseudo-potential instead of a full general relativistic treatment. Our treatment focuses solely on the toroidal component of the magnetic field, neglecting the poloidal components and the effects of anisotropic thermal conduction in complex magnetic fields. Moreover, we do not incorporate mass loss from the disk, even though thermal conduction may play a significant role in the dynamics of outflows. While all these processes are relevant in accretion dynamics, their consideration is beyond the scope of this paper and will be examined in future studies.

Conclusion and Future Directions 5

> `"...Nothing in life is to be feared, it is only to be understood. Now is the time to understand more, so that we may fear less...."`
>
> *Marie Curie*

The dynamics of relativistic hot accretion flows around rotating black holes have been examined in this thesis with a focus on the contributions of magnetic fields, thermal conduction, and radially varying viscosity. Subsequently, we study the shock-induced global transonic solutions and shock characteristics.

In Chapter 2, the α-prescription for viscous transport is generalized to a power-law form as $\alpha(r) = \alpha_0 r^\theta$ in our investigation of relativistic accretion flows. We examine the generation of centrifugally supported shocks and identify the sets of global transonic accretion solutions by solving the relativistic fluid equations in a pseudo-Newtonian potential framework that mimics the Kerr geometry. In doing so, we employ the relativistic equation of state (REoS) which takes care of the variable nature of adiabatic index (Γ). We find that the viscosity exponent θ plays a pivotal role in governing the flow properties and behaviour of shock properties. A critical threshold of $\theta^{\rm max}$ is determined beyond which standing shocks cannot form. Importantly, $\theta^{\rm max}$ is not universal but varies with the spin of the black hole. In particular, higher spin value ($a_{\rm k} \rightarrow 1$), that implies rapidly rotating black holes, can accommodate higher viscous dissipation to yield shock solutions. Furthermore, we also study the correlation between the viscosity parameters α_0 and $\theta^{\rm max}$ for both non-rotating ($a_{\rm k} \rightarrow 0$) and rapidly rotating BHs ($a_{\rm k} \rightarrow 1$).

In the subsequent Chapter of the thesis, we extended our model by incorporating the effects of saturated thermal conduction. Indeed, thermal conduction becomes important for weakly collisional low-density accretion flows in the radiatively inefficient regime. Employing dissipation parameters, namely viscosity parameter α, thermal conduction parameter $\Phi_{\rm s}$, and cooling parameter f_c, we investigate how thermal conduction influences the dynamics of the flow and shock-induced transonic accretion solutions.

Our results show that thermal conduction can significantly redistribute temperature and energy within the accretion disk especially from the inner, hotter regions toward the outer disk. This redistribution leads to an increase in the temperature and pressure, thereby altering the balance of forces that sustains the shock. Consequently, we observe a systematic outward shift of the shock location ($r_{\rm s}$) with increasing $\Phi_{\rm s}$ and a weakening of the shock strength (S) and compression ratio (R). The shock parameter space in the energy and angular momentum ($\mathcal{E}$–λ) plane further illustrated how thermal conduction and cooling influences the shrinking of parameter space that admits shock transition. We quantify the critical conduction parameter $\Phi_{\rm s}^{\rm crit}$ for shock solutions, beyond which the Rankine–Hugoniot conditions are not favourable, and standing shocks no longer form. Interestingly, this critical conduction threshold increases with black hole spin but decreases with increasing α, which highlights the complex interplay between viscous and conductive dissipation.

In the Chapter 4, we study the role of toroidal magnetic fields on the accretion solutions in the presence of the viscous-conductive framework. Assuming the dominance of the toroidal component (as motivated by simulations and observational modelling), we study the structure of magnetised, viscous, and advective relativistic accretion flows with synchrotron and bremsstrahlung cooling, in addition to thermal conduction.

In this extended framework, we investigate the effect of the magnetic activity via the plasma-β parameter and study how magnetic fields modulate the dynamics of shocks and shock properties. We find that strong magnetic fields (low plasma-β) reduce the pressure support in the post-shock region, and this also decreases the synchrotron cooling in the flow, which pushes the shock radius $r_{\rm s}$ inwards. As the $r_{\rm s}$ vies inwards, increasing shock strength (S) and shock compression (R). However, simultaneous inclusion of thermal conduction reveals a competing effect, enhanced conduction weakens shock strength and compression ratio by increasing the temperature in the post-shock flow. In addition, we identify a critical conduction $\Phi_{\rm s}^{\rm crit}$ for shock solutions, and show that $\Phi_{\rm s}^{\rm crit}$ is sensitive to both magnetic field strength (β) and $\alpha_{\rm B}$. Furthermore, we examined the resulting spectral energy distributions (SEDs) and find that increased conduction and magnetic field strength lead to enhanced disk luminosity.

In conclusion, the comprehensive analysis presented in this thesis significantly advances our understanding of the physics governing relativistic accretion flows onto black holes. It highlights the critical role of dissipation such as both viscous and conductive, as well as magnetic fields in controlling the thermodynamics and radiative signatures of accreting black hole systems.

Future Directions

In this thesis work, we focus solely on the single-temperature flow. However, in the vicinity of the horizon, where flow might be in a free-fall situation, electrons and ions coulamb coupling might not have enough time to establish a single temperature. In such scenarios, electrons and ions will have their own temperature distributions, and hence the flow characteristics are governed by a two-temperature framework (Mandal & Chakrabarti, 2005; Dihingia et al., 2018b, 2020). In future, we aim to study the dynamics of the flow and shock properties in the two-temperature formalism with the inclusion of the effect of thermal conduction in both non-magnetised and magnetised plasma.

In Chapter 2, we considered a power-law description of α viscosity prescription with hydrodynamics approach. However, in the MHD and GRMHD simulation studies, researchers have obtained various profiles of α viscosity (Shafee et al., 2008; Avara et al., 2016; Hogg & Reynolds, 2018; Jiang et al., 2019; Kawanaka & Masada, 2019). In the future study, we plan to investigate the comparative analysis of the accretion flow around BHs with various reported α viscosity prescriptions in both single and two-temperature formalism in MHD framework. Furthermore, the pseudo-Newtonian potential provides an effective approximation to the Kerr metric. However, to capture all relativistic effects such as the frame-dragging effect near the horizon, a natural extension would be to study the accretion flow using full GRMHD equations, including thermal conduction and radiative cooling.

While the current work is based on steady state scenarios, accretion flows in realistic astrophysical environments are inherently time-dependent and often exhibit variability (Giri et al., 2010; Das et al., 2014b; Debnath et al., 2024a). In particular, non-stationary shock oscillations are known to give rise to quasi-periodic oscillations (QPOs) observed in black hole X-ray binaries (Chakrabarti & Manickam, 2000; Nandi et al., 2012; Iyer et al., 2015; Das et al., 2021; Majumder et al., 2022; Harikesh et al., 2025). Time-dependent numerical simulations (Dihingia et al., 2025) can help explore how shocks behave dynamically in the presence of conduction and magnetic fields. Furthermore, we also intend to examine the observational constraints on the theoretically derived parameter space of accretion solutions. For instance, the hysteresis phenomenon observed during state transitions in black hole X-ray binaries may be interpreted as arising from changes within this parameter space, such as the emergence or disappearance of specific solutions.

Appendix A

Appendix: Derivation of wind equation (Chapter 2)

With some simple algebraic steps, the radial momentum equations, azimuthal momentum equations and entropy generation equations are reduced to the following form as,

$$R_0 + R_\upsilon \frac{d\upsilon}{dr} + R_\Theta \frac{d\Theta}{dr} + R_\lambda \frac{d\lambda}{dr} = 0, \tag{A.1}$$

$$L_0 + L_\upsilon \frac{d\upsilon}{dr} + L_\Theta \frac{d\Theta}{dr} + L_\lambda \frac{d\lambda}{dr} = 0, \tag{A.2}$$

$$E_0 + E_\upsilon \frac{d\upsilon}{dr} + E_\Theta \frac{d\Theta}{dr} + E_\lambda \frac{d\lambda}{dr} = 0. \tag{A.3}$$

Using the equations (A1-A3), we obtain the wind equation, derivative of angular momentum and derivative of temperature which are given by,

$$\frac{d\upsilon}{dr} = \frac{\mathcal{N}}{\mathcal{D}}, \tag{A.4}$$

$$\frac{d\lambda}{dr} = \lambda_1 + \lambda_2 \frac{d\upsilon}{dr}, \tag{A.5}$$

$$\frac{d\Theta}{dr} = \Theta_1 + \Theta_2 \frac{d\upsilon}{dr}, \tag{A.6}$$

where,

$$\begin{aligned}\mathcal{N} = {} & E_\lambda \left(-R_\Theta L_0 + R_0 L_\Theta\right) + E_\Theta \left(R_\lambda L_0 - R_0 L_\lambda\right) \\ & + E_0 \left(-R_\lambda L_\Theta + R_\Theta L_\lambda\right),\end{aligned}$$

$$\begin{aligned}\mathcal{D} = {} & E_\lambda \left(R_\Theta L_\upsilon + R_\upsilon L_\Theta\right) + E_\Theta \left(-R_\lambda L_\upsilon + R_\upsilon L_\lambda\right) \\ & + E_\upsilon \left(R_\lambda L_\Theta - R_\Theta L_\lambda\right),\end{aligned}$$

$$\Theta_1 = \frac{\Theta_{11}}{\Theta_{33}} \quad \Theta_2 = \frac{\Theta_{22}}{\Theta_{33}}, \quad \lambda_1 = \frac{\lambda_{11}}{\Theta_{33}}, \quad \lambda_2 = \frac{\lambda_{22}}{\Theta_{33}},$$

$$\Theta_{11} = E_\lambda L_0 - E_0 L_\lambda,\ \ \Theta_{22} = E_\lambda L_\upsilon - E_\upsilon L_\lambda,\ \Theta_{33} = -E_\lambda L_\Theta + E_\Theta L_\lambda,$$

$$\lambda_{11} = -E_\Theta L_0 + E_0 L_\Theta,\ \ \lambda_{22} = -E_\Theta L_\upsilon + E_\upsilon L_\Theta,$$

$$\begin{aligned}
R_0 =& \frac{d\Phi_e^{\rm eff}}{dr} - \frac{3\Theta}{r\tau h} + \frac{F_1\Theta}{\tau\mathcal{F}h} - \frac{\Theta\Delta'}{\tau\Delta h},\ R_\Theta = \frac{1}{\tau h}, \tau = 1 + \frac{m_p}{m_e},\\
R_\lambda =& \frac{F_2\Theta}{\tau\mathcal{F}h},\ R_\upsilon = \upsilon - \frac{2\Theta}{\tau\upsilon h},\ \Delta' = \frac{d\Delta}{dr},\\
E_0 =& -\frac{Q^-}{\rho} - r\alpha\upsilon^2\omega_1 - \frac{2r\alpha\Theta\omega_1}{\tau} + \frac{\upsilon\Theta\left(-rF_1\Delta + \mathcal{F}(3\Delta + r\Delta')\right)}{r\tau\Delta},\\
E_\Theta =& \frac{(1+2n\upsilon)}{\tau},\ E_\lambda - \frac{(F_2\upsilon\Theta + r\alpha\mathcal{F}(\tau\upsilon^2 + 2\Theta)\omega_2)}{\tau\mathcal{F}},\ E_\upsilon = \frac{2\theta}{\tau},\\
L_0 =& -2\alpha\upsilon^2 - \frac{4\alpha\Theta}{\tau} + \frac{r\alpha\upsilon^2\Delta'}{2\Delta} + \frac{r\alpha\Theta\Delta'}{\tau\Delta} - \frac{r}{\tau}\left(\tau\upsilon^2 + 2\Theta\right)\frac{d\alpha}{dr},\\
L_\Theta =& -\frac{2r\alpha}{\tau},\ L_\lambda = \upsilon,\ L_\upsilon = -r\alpha\upsilon + \frac{2r\alpha\Theta}{\tau\upsilon},\\
F_1 =& \frac{F\lambda\omega_1}{(1-\lambda\Omega)^2} + \frac{1}{1-\lambda\Omega}\frac{dF}{dr},\\
F_2 =& \frac{F\Omega}{(1-\lambda\Omega)^2} + \frac{F\lambda\omega_2}{(1-\lambda\Omega)^2},\ \mathcal{F} = \frac{1}{(1-\lambda\Omega)}F,\\
F =& \frac{(r^2 + a_{\rm k}^2)^2 + 2\Delta a_{\rm k}^2}{(r^2 + a_{\rm k}^2)^2 - 2\Delta a_{\rm k}^2},\ \frac{d\mathcal{F}}{dr} = F_1 + F_2\frac{d\lambda}{dr},\ \frac{d\Omega}{dr} = \omega_1 + \omega_2\frac{d\lambda}{dr},\\
\omega_1 =& -\frac{2\left(a_{\rm k}^3 + 3a_{\rm k}r^2 + \lambda(a_{\rm k}\lambda - 2a_{\rm k}^2 + r^2(r-3))\right)}{\left(r^3 + a_{\rm k}^2(r+2) - 2a_{\rm k}\lambda\right)^2},\\
\omega_2 =& \frac{r^2\left(a_{\rm k}^2 + r(r-2)\right)}{\left(r^3 + a_{\rm k}^2(r+2) - 2a_{\rm k}\lambda\right)^2}.
\end{aligned}$$

Appendix B

Appendix: Derivation of wind equation (Chapter 3)

After some algebra, the radial momentum, azimuthal momentum and entropy generation equations read as,

$$R_0 + R_\upsilon \frac{d\upsilon}{dr} + R_\Theta \frac{d\Theta}{dr} + R_\lambda \frac{d\lambda}{dr} = 0, \tag{B.1}$$

$$L_0 + L_\upsilon \frac{d\upsilon}{dr} + L_\Theta \frac{d\Theta}{dr} + L_\lambda \frac{d\lambda}{dr} = 0, \tag{B.2}$$

$$E_0 + E_\upsilon \frac{d\upsilon}{dr} + E_\Theta \frac{d\Theta}{dr} + E_\lambda \frac{d\lambda}{dr} = 0. \tag{B.3}$$

After further simplification, we have,

$$\frac{d\upsilon}{dr} = \frac{\mathcal{N}}{\mathcal{D}}, \tag{B.4}$$

$$\frac{d\Theta}{dr} = \Theta_1 + \Theta_2 \frac{d\upsilon}{dr}, \tag{B.5}$$

$$\frac{d\lambda}{dr} = \lambda_1 + \lambda_2 \frac{d\upsilon}{dr}, \tag{B.6}$$

where

$$\begin{aligned}\mathcal{N} = {} & E_\lambda \left(-R_\Theta L_0 + R_0 L_\Theta\right) + E_\Theta \left(R_\lambda L_0 - R_0 L_\lambda\right) \\ & + E_0 \left(-R_\lambda L_\Theta + R_\Theta L_\lambda\right),\end{aligned}$$

$$\begin{aligned}\mathcal{D} = {} & E_\lambda \left(R_\Theta L_\upsilon - R_\upsilon L_\Theta\right) + E_\Theta \left(-R_\lambda L_\upsilon + R_\upsilon L_\lambda\right) \\ & + E_\upsilon \left(R_\lambda L_\Theta - R_\Theta L_\lambda\right).\end{aligned}$$

The expressions of the coefficients used in the above equations are given by,

$$\Theta_1 = \frac{\Theta_{11}}{\Theta_{33}}, \quad \Theta_2 = \frac{\Theta_{22}}{\Theta_{33}}, \quad \lambda_1 = \frac{\lambda_{11}}{\Theta_{33}}, \quad \lambda_2 = \frac{\lambda_{22}}{\Theta_{33}},$$

$$\begin{aligned}\Theta_{11} =& E_\lambda L_0 - E_0 L_\lambda, \;\; \Theta_{22} = E_\lambda L_\upsilon - E_\upsilon L_\lambda,\\ \Theta_{33} =& -E_\lambda L_\Theta + E_\Theta L_\lambda,\end{aligned}$$

$$\lambda_{11} = -E_\Theta L_0 + E_0 L_\Theta, \;\; \lambda_{22} = -E_\Theta L_\upsilon + E_\upsilon L_\Theta,$$

$$\begin{aligned}R_0 =& \frac{d\Phi_e^{\mathrm{eff}}}{dr} - \frac{3\Theta}{r\tau h} + \frac{F_3\Theta}{\tau F_2 h} - \frac{\Theta}{\tau\Delta h}\frac{d\Delta}{dr},\\ R_\Theta =& \frac{1}{\tau h}, \;\; R_\lambda = \frac{F_4\Theta}{\tau F_2 h}, \;\; R_\upsilon = \upsilon - \frac{2\Theta}{\tau\upsilon h},\end{aligned}$$

$$\begin{aligned}E_0 =& \frac{5\Phi_{\mathrm{s}}}{2}\left(\frac{2\Theta}{\tau}\right)^{3/2}\left(\frac{1}{r} - \frac{F_3}{F_2} + \frac{1}{\Delta}\frac{d\Delta}{dr}\right) - r\alpha\upsilon^2\omega_1\\ &- \frac{2r\alpha\Theta\omega_1}{\tau} + \frac{3\upsilon\Theta}{r\tau} - \frac{F_3\upsilon\Theta}{\tau F_2} + \frac{\upsilon\Theta}{\tau\Delta}\frac{d\Delta}{dr},\end{aligned}$$

$$E_\Theta = -\frac{5\Phi_{\mathrm{s}}}{\Theta}\left(\frac{2\Theta}{\tau}\right)^{3/2} + \frac{(1+2N)\,\upsilon}{\tau}$$

$$\begin{aligned}E_\lambda =& \frac{5\Phi_{\mathrm{s}}F_4}{2F_2}\left(\frac{2\Theta}{\tau}\right)^{3/2} - \frac{F_4\upsilon\Theta}{\tau F_2} - r\upsilon^2\alpha\omega_2 - \frac{2r\alpha\Theta\omega_2}{\tau},\\ E_\upsilon =& \frac{5\Phi_{\mathrm{s}}}{\upsilon}\left(\frac{2\Theta}{\tau}\right)^{3/2} + \frac{2\Theta}{\tau},\\ L_0 =& -2\alpha\upsilon^2 - \frac{4\alpha\Theta}{\tau} + \frac{r\alpha\upsilon^2}{2\Delta}\frac{d\Delta}{dr} + \frac{r\alpha\Theta}{\tau\Delta}\frac{d\Delta}{dr}, L_\Theta = -\frac{2r\alpha}{\tau},\\ L_\lambda =& \upsilon, \;\; L_\upsilon = -r\alpha\upsilon + \frac{2r\alpha\Theta}{\tau\upsilon},\\ F_1 =& \frac{((r^2+a_{\mathrm{k}}^2)^2 + 2\Delta a_{\mathrm{k}}^2)}{((r^2+a_{\mathrm{k}}^2)^2 - 2\Delta a_{\mathrm{k}}^2)}, F_2 = \frac{1}{(1-\lambda\Omega)}F_1,\\ F_3 =& \frac{F_1\lambda\omega_1}{(1-\lambda\Omega)^2} + \frac{1}{1-\lambda\Omega}\frac{dF_1}{dr}, \;\; F_4 = \frac{F_1\Omega}{(1-\lambda\Omega)^2} + \frac{F_1\lambda\omega_2}{(1-\lambda\Omega)^2},\\ &\frac{dF_2}{dr} = F_3 + F_4\frac{d\lambda}{dr}, \;\; \frac{d\Omega}{dr} = \omega_1 + \omega_2\frac{d\lambda}{dr},\end{aligned}$$

$$\omega_1 = -\frac{2\left(a_{\mathrm{k}}^3 + 3a_{\mathrm{k}}r^2 + \lambda(a_{\mathrm{k}}\lambda - 2a_{\mathrm{k}}^2 + r^2(r-3))\right)}{\left(r^3 + a_{\mathrm{k}}^2(r+2) - 2a_{\mathrm{k}}\lambda\right)^2}, \omega_2 = \frac{r^2\left(a_{\mathrm{k}}^2 + r(r-2)\right)}{\left(r^3 + a_{\mathrm{k}}^2(r+2) - 2a_{\mathrm{k}}\lambda\right)^2}.$$

Appendix C

Appendix: Calculation of wind equation (Chapter 4)

$$R_0 + R_\Theta \frac{d\Theta}{dr} + R_\lambda \frac{d\lambda}{dr} + R_\beta \frac{d\beta}{dr} + R_\upsilon \frac{d\upsilon}{dr} = 0, \tag{C.1}$$

$$L_0 + L_\Theta \frac{d\Theta}{dr} + L_\lambda \frac{d\lambda}{dr} + L_\beta \frac{d\beta}{dr} + L_\upsilon \frac{d\upsilon}{dr} = 0, \tag{C.2}$$

$$B_0 + B_\Theta \frac{d\Theta}{dr} + B_\lambda \frac{d\lambda}{dr} + B_\beta \frac{d\beta}{dr} + B_\upsilon \frac{d\upsilon}{dr} = 0, \tag{C.3}$$

$$E_0 + E_\Theta \frac{d\Theta}{dr} + E_\lambda \frac{d\lambda}{dr} + E_\beta \frac{d\beta}{dr} + E_\upsilon \frac{d\upsilon}{dr} = 0. \tag{C.4}$$

After simplifying the above equation, we obtain,

$$\frac{d\upsilon}{dr} = \frac{\mathcal{N}}{\mathcal{D}} \tag{C.5}$$

$$\frac{d\Theta}{dr} = \Theta_1 + \Theta_2 \frac{d\upsilon}{dr} \tag{C.6}$$

$$\frac{d\lambda}{dr} = \lambda_1 + \lambda_2 \frac{d\upsilon}{dr} \tag{C.7}$$

$$\frac{d\beta}{dr} = \beta_1 + \beta_2 \frac{d\upsilon}{dr}, \tag{C.8}$$

where,

$$\begin{aligned}\mathcal{N} = &-E_\beta R_\lambda B_\Theta B_0 + E_\beta R_\Theta B_\lambda L_0 + E_0 R_\lambda B_\Theta L_\beta - E_0 R_\Theta B_\lambda B_\beta + E_\beta R_\lambda B_0 L_\Theta - E_0 R_\lambda B_\beta L_\Theta \\ &- E_\beta R_0 B_\lambda L_\Theta + E_0 R_\beta B_\lambda L_\Theta + E_\lambda [R_\beta B_\Theta L_0 - R_0 B_\Theta L_\beta + R_\Theta(-B_\beta L_0 + B_0 L_\beta) - R_\beta B_0 L_\Theta + \\ &R_0 B_\beta L_\Theta] - E_\beta R_0 B_0 L_\lambda + E_0 R_\Theta B_\beta L_\lambda + E_\beta R_0 B_\Theta B_\lambda - E_0 R_\beta B_\Theta L_\lambda + E_\Theta[R_\lambda B_\beta L_0 - R_\beta B_\lambda L_0 - \\ &R_\lambda B_0 L_\beta + R_0 B_\lambda L_\beta + R_\beta B_0 L_\lambda - R_0 B_\beta L_\lambda]\end{aligned}$$

$$\begin{aligned}\mathcal{D} = &E_\beta R_\lambda B_\theta L_\upsilon - E_\beta R_\Theta B_\lambda L_\upsilon - E_\upsilon R_\lambda B_\Theta L_\beta + E_\upsilon R_\Theta B_\lambda L_\beta - E_\beta R_\lambda B_\upsilon L_\Theta + E_\upsilon R_\lambda B_\beta L_\Theta \\ &+ E_\beta R_\upsilon B_\lambda L_\Theta - E_\upsilon R_\beta B_\lambda L_\Theta + E_\lambda[-R_\beta B_\Theta L_\upsilon + R_\upsilon B_\Theta L_\beta + R_\Theta(B_\beta L_\upsilon - B_\upsilon L_\beta) + R_\beta B_\upsilon L_\Theta \\ &- R_\upsilon B_\beta L_\Theta] + E_\beta R_\Theta B_\upsilon L_\lambda - E_\upsilon R_\Theta B_\beta L_\lambda - E_\beta R_\upsilon B_\Theta L_\lambda + E_\upsilon R_\beta B_\Theta L_\lambda + E_\Theta[-R_\lambda B_\beta L_\upsilon \\ &+ R_\beta B_\lambda L_\upsilon + R_\lambda B_\upsilon L_\beta - R_\upsilon B_\lambda L_\beta - R_\beta B_\upsilon L_\lambda + R_\upsilon B_\beta L_\lambda]\end{aligned}$$

$$\begin{gathered}\Theta_1 = \frac{\Theta_{11}}{\Theta_{33}},\ \Theta_2 = \frac{\Theta_{22}}{\Theta_{33}},\ \lambda_1 = \frac{\lambda_{11}}{\lambda_{33}},\ \lambda_2 = \frac{\lambda_{22}}{\lambda_{33}},\ \beta_1 = \frac{\beta_{11}}{\beta_{33}},\ \beta_2 = \frac{\beta_{22}}{\beta_{33}}, \\ \Theta_{11} = -[(E_\beta L_0 - E_0 L_\beta)(E_\lambda B_\beta - E_\beta B_\lambda) + (-E_\lambda L_\beta + E_\beta L_\lambda)(E_\beta B_0 - E_0 B_\beta)], \\ \Theta_{22} = -[(E_\beta L_\upsilon - E_\upsilon L_\beta)(E_\lambda B_\beta - E_\beta B_\lambda) + (E_\beta \beta_\upsilon - E_\upsilon B_\beta)(-E_\lambda L_\beta + E_\beta L_\lambda)], \\ \Theta_{33} = (E_\lambda B_\beta - E_\beta B_\lambda)(-E_\Theta L_\beta + E_\beta L_\Theta) + (-E_\Theta B_\beta + E_\beta \beta_\Theta)(-E_\lambda L_\beta + E_\beta L_\lambda), \\ \lambda_{11} = -E_\Theta B_\beta L_0 + E_\beta B_\Theta L_0 + E_\Theta B_0 L_\beta - E_0 B_\Theta L_\beta - E_\beta B_0 L_\Theta + E_0 B_\beta L_\Theta, \\ \lambda_{22} = -E_\Theta B_\beta L_\upsilon + E_\beta B_\Theta L_\upsilon + E_\Theta B_\upsilon L_\beta - E_\upsilon B_\Theta L_\beta - E_\beta B_\upsilon L_\Theta + E_0 B_\beta L_\Theta \\ \lambda_{33} = E_\lambda B_\Theta L_\beta - E_\Theta B_\lambda L_\beta - E_\lambda B_\beta L_\Theta + E_\beta B_\lambda L_\Theta + E_\Theta B_\beta L_\lambda - E_\beta B_\Theta L_\lambda, \\ \beta_{11} = -E_\lambda B_\Theta L_0 + E_\Theta B_\lambda L_0 + E_\lambda B_0 L_\Theta - E_0 B_\lambda L_\Theta - E_\Theta B_0 L_\lambda + E_0 B_\Theta L_\lambda, \\ \beta_{22} = -E_\lambda B_\Theta L_\upsilon + E_\Theta B_\lambda L_\upsilon + E_\lambda B_\upsilon L_\Theta - E_\upsilon B_\lambda L_\Theta - E_\Theta B_\upsilon L_\lambda + E_\upsilon B_\Theta L_\lambda, \\ \beta_{33} = \lambda_{33}, \\ R_0 = \frac{d\Phi_{\rm e}^{\rm eff}}{dr} + \frac{4\Theta}{r\tau\beta} + \frac{2\Theta(1+\beta^{-1})}{\tau h}\left(-\frac{3}{3r} + \frac{F_3}{2F_2} - \frac{1}{\Delta}\frac{d\Delta}{dr}\right),\ R_\upsilon = \upsilon - \frac{2\Theta}{\tau h \upsilon}(1+\beta^{-1}) \\ R_\Theta = \frac{(1+\beta^{-1})}{\tau h},\ R_\lambda = \frac{F_4\Theta(1+\beta^{-1})}{\tau h F_2},\ R_\beta = -\frac{\Theta}{\tau h \beta^2} \\ L_0 = -2\alpha\upsilon^2 - \frac{4\alpha\Theta(1+\beta^{-1})}{\tau} + \frac{d\Delta}{dr}\left(\frac{r\alpha(\tau\upsilon^2\beta + 2\Theta(1+\beta^{-1}))}{2\tau\beta}\right), \\ L_\upsilon = -r\alpha\upsilon + \frac{2r\alpha\Theta(1+\beta^{-1})}{\tau\upsilon},\ L_\Theta - \frac{2r\alpha(1+\beta^{-1})}{\tau},\ L_\lambda = \upsilon,\ L_\beta = \frac{2r\alpha\Theta}{\tau\beta^2}\end{gathered}$$

$$\begin{aligned}E_0 = &-\frac{Q^-}{\rho H} + \frac{5\Phi_{\rm s}\Theta}{\tau}\sqrt{\frac{2\Theta}{\tau}}\left(\frac{1}{r} - \frac{F_3}{F_2} + \frac{1}{\Delta}\frac{d\Delta}{dr}\right) + \frac{3\upsilon\Theta}{r\tau} - \frac{F_3\upsilon\Theta}{\tau F_2} - \frac{2r\alpha\Theta\omega_1(1+\beta^{-1})}{\tau} - r\alpha\upsilon^2\omega_1 \\ &+ \frac{\upsilon\Theta}{\tau\Delta}\frac{d\Delta}{dr},\ E_\upsilon = \frac{2\Theta}{\tau} + \frac{10\sqrt{2}\Phi_{\rm s}}{\upsilon}\left(\frac{\Theta}{\tau}\right)^{3/2},\ E_\Theta = -\frac{5\Phi_{\rm s}}{\Theta}\left(\frac{2\Theta}{\tau}\right)^{3/2} + \frac{(1+2N)\,\upsilon}{\tau}\end{aligned}$$

$$E_\lambda = -\frac{F_4 \upsilon \Theta}{\tau F_2} - \frac{5\sqrt{2}\Phi_{\mathrm{s}} F_4}{F_2}\left(\frac{\Theta}{\tau}\right)^{3/2} - r\alpha\left(\upsilon^2 + \frac{2\Theta(1+\beta^{-1})}{\tau}\right)\omega_2,$$

$$E_\beta = -\frac{1}{\beta(1+\beta)}\left(\frac{\upsilon\Theta}{\tau} + \frac{5\Phi_{\mathrm{s}}\Theta}{\tau}\sqrt{\frac{2\Theta}{\tau}}\right),\ B_0 = \frac{3}{4r}+\frac{\zeta}{r}-\frac{F_3}{4F_2}-\frac{1}{4\Delta}\frac{d\Delta}{dr},\ B_\upsilon = \frac{1}{2\upsilon},\ B_\Theta = \frac{3}{4\Theta}$$

$$B_\lambda = -\frac{F_4}{4F_2},\ B_\beta = -\frac{1}{(1+\beta)}\left(\frac{1}{2} + \frac{3}{4\beta}\right)$$

$$F_3 = \frac{F_1\lambda\omega_1}{(1-\lambda\Omega)^2} + \frac{1}{1-\lambda\Omega}\frac{dF_1}{dr},\ F_4 = \frac{F_1\Omega}{(1-\lambda\Omega)^2} + \frac{F_1\lambda\omega_2}{(1-\lambda\Omega)^2},\ F_2 = \frac{1}{(1-\lambda\Omega)}F_1,$$

$$F_1 = \frac{((r^2+a_{\mathrm{k}}^2)^2 + 2\Delta a_{\mathrm{k}}^2)}{((r^2+a_{\mathrm{k}}^2)^2 - 2\Delta a_{\mathrm{k}}^2)},\ \frac{dF_2}{dr} = F_3 + F_4\frac{d\lambda}{dr},\ \frac{d\Omega}{dr} = \omega_1 + \omega_2\frac{d\lambda}{dr},$$

$$\omega_1 = -\frac{2\left(a_{\mathrm{k}}^3 + 3a_{\mathrm{k}}r^2 + \lambda(a_{\mathrm{k}}\lambda - 2a_{\mathrm{k}}^2 + r^2(r-3))\right)}{\left(r^3 + a_{\mathrm{k}}^2(r+2) - 2a_{\mathrm{k}}\lambda\right)^2},$$

$$\omega_2 = \frac{r^2\left(a_{\mathrm{k}}^2 + r(r-2)\right)}{\left(r^3 + a_{\mathrm{k}}^2(r+2) - 2a_{\mathrm{k}}\lambda\right)^2}.$$

Bibliography

Abramowicz M. A., Fragile P. C., 2013, Living Reviews in Relativity, 16, 1

Abramowicz M. A., Zurek W. H., 1981, Astrophys. J. , 246, 314

Abramowicz M. A., Czerny B., Lasota J. P., Szuszkiewicz E., 1988, Astrophys. J. , 332, 646

Aktar R., Das S., Nandi A., Sreehari H., 2017a, Mon. Not. R. Astron. Soc. , 471, 4806

Aktar R., Das S., Nandi A., Sreehari H., 2017b, Mon. Not. R. Astron. Soc. , 471, 4806

Aktar R., Das S., Nandi A., Sreehari H., 2018, Journal of Astrophysics and Astronomy, 39, 17

Aktar R., Nandi A., Das S., 2019, Astrophysics and Space Science, 364, 22

Alston W., Fabian A., Markevičiutė J., Parker M., Middleton M., Kara E., 2016, Astronomische Nachrichten, 337, 417

Aneesha U., Das S., Katoch T. B., Nandi A., 2024, Mon. Not. R. Astron. Soc. , 532, 4486

Artemova I. V., Bjoernsson G., Novikov I. D., 1996, Astrophys. J. , 461, 565

Athulya M. P., Radhika D., Agrawal V. K., Ravishankar B. T., Naik S., Mandal S., Nandi A., 2022, Mon. Not. R. Astron. Soc. , 510, 3019

Avara M. J., McKinney J. C., Reynolds C. S., 2016, Monthly Notices of the Royal Astronomical Society, 462, 636

Baby B. E., Agrawal V. K., Ramadevi M. C., Katoch T., Antia H. M., Mandal S., Nandi A., 2020, Mon. Not. R. Astron. Soc. , 497, 1197

Bachetti M., et al., 2014, Nature, 514, 202

Balbus S. A., Hawley J. F., 1991, Astrophys. J. , 376, 214

Balbus S. A., Hawley J. F., 1998, Reviews of Modern Physics, 70, 1

Bambic C. J., Quataert E., Kunz M. W., Jiang Y.-F., 2024, Mon. Not. R. Astron. Soc. , 530, 1812

Becker P. A., Kazanas D., 2001, Astrophys. J. , 546, 429

Becker P. A., Das S., Le T., 2008, Astrophys. J. Lett. , 677, L93

Begelman M. C., Armitage P. J., 2014, Astrophys. J. Lett. , 782, L18

Belloni T., Klein-Wolt M., Méndez M., van der Klis M., van Paradijs J., 2000, Astron. Astrophys. , 355, 271

Belloni T., Homan J., Motta S., Ratti E., Méndez M., 2007, Mon. Not. R. Astron. Soc. , 379, 247

Blandford R. D., Znajek R. L., 1977, Mon. Not. R. Astron. Soc. , 179, 433

Bondi H., 1952, Monthly Notices of the Royal Astronomical Society, 112, 195

Bondi H., Hoyle F., 1944, Monthly Notices of the Royal Astronomical Society, 104, 273

Bonnet-Bidaud J. M., Mouchet M., Busschaert C., Falize E., Michaut C., 2015, Astron. Astrophys. , 579, A24

Bu D.-F., Wu M.-C., Yuan Y.-F., 2016, Mon. Not. R. Astron. Soc. , 459, 746

Cassatella P., Uttley P., Maccarone T. J., 2012, Mon. Not. R. Astron. Soc. , 427, 2985

Chakrabarti S. K., 1989, Astrophys. J. , 347, 365

Chakrabarti S. K., 1990a, Theory of Transonic Astrophysical Flows. WORLD SCIENTIFIC (https://www.worldscientific.com/doi/pdf/10.1142/1091), doi:10.1142/1091, `https://www.worldscientific.com/doi/abs/10.1142/1091`

Chakrabarti S. K., 1990b, Theory of Transonic Astrophysical Flows. WORLD SCIENTIFIC (https://www.worldscientific.com/doi/pdf/10.1142/1091), doi:10.1142/1091, `https://www.worldscientific.com/doi/abs/10.1142/1091`

Chakrabarti S. K., 1996, Astrophys. J. , 464, 664

Chakrabarti S. K., 1997, Astrophys. J. , 484, 313

Chakrabarti S. K., Das S., 2001, Monthly Notices of the Royal Astronomical Society, 327, 808

Chakrabarti S. K., Das S., 2004, Mon. Not. R. Astron. Soc. , 349, 649

Chakrabarti S. K., Khanna R., 1992, Mon. Not. R. Astron. Soc. , 256, 300

Chakrabarti S. K., Mandal S., 2006, Astrophys. J. Lett. , 642, L49

Chakrabarti S. K., Manickam S. G., 2000, Astrophys. J. Lett. , 531, L41

Chakrabarti S. K., Molteni D., 1993, Astrophys. J. , 417, 671

Chakrabarti S. K., Molteni D., 1995, Mon. Not. R. Astron. Soc. , 272, 80

Chakrabarti S. K., Mondal S., 2006, Mon. Not. R. Astron. Soc. , 369, 976

Chakrabarti S., Titarchuk L. G., 1995, Astrophys. J. , 455, 623

Chakrabarti S. K., Debnath D., Nandi A., Pal P. S., 2008, Astron. Astrophys. , 489, L41

Chakrabarti S. K., Dutta B. G., Pal P. S., 2009, Mon. Not. R. Astron. Soc. , 394, 1463

Chatterjee D., Debnath D., Chakrabarti S. K., Mondal S., Jana A., 2016, Astrophys. J. , 827, 88

Chattopadhyay I., Chakrabarti S. K., 2000, International Journal of Modern Physics D, 9, 717

Chattopadhyay I., Kumar R., 2016, Mon. Not. R. Astron. Soc. , 459, 3792

Chattopadhyay I., Ryu D., 2009, Astrophys. J. , 694, 492

Colella P., Woodward P. R., 1984, Journal of Computational Physics, 54, 174

Coughlin E. R., Begelman M. C., 2014, Astrophys. J. , 781, 82

Cowie L. L., McKee C. F., 1977, Astrophys. J. , 211, 135

Czerny B., 2019, Universe, 5, 131

Czerny B., Elvis M., 1987, Astrophys. J. , 321, 305

Das S., 2007, Mon. Not. R. Astron. Soc. , 376, 1659

Das S., Chakrabarti S. K., 2008, Mon. Not. R. Astron. Soc. , 389, 371

Das S., Sarkar B., 2018, Mon. Not. R. Astron. Soc. , 480, 3446

Das S., Chattopadhyay I., Chakrabarti S. K., 2001, Astrophys. J. , 557, 983

Das S., Becker P. A., Le T., 2009a, Astrophys. J. , 702, 649

Das S., Becker P. A., Le T., 2009b, Astrophys. J. , 702, 649

Das S., Chattopadhyay I., Nandi A., Molteni D., 2014a, Mon. Not. R. Astron. Soc. , 442, 251

Das S., Chattopadhyay I., Nandi A., Molteni D., 2014b, Mon. Not. R. Astron. Soc. , 442, 251

Das S., Nandi A., Agrawal V. K., Dihingia I. K., Majumder S., 2021, Mon. Not. R. Astron. Soc. , 507, 2777

Datta S. R., Mondal T., Mukhopadhyay B., 2022, Mon. Not. R. Astron. Soc. , 513, 204

De Villiers J.-P., Hawley J. F., 2003, Astrophys. J. , 589, 458

Debnath D., Chakrabarti S. K., Nandi A., 2010, Astron. Astrophys. , 520, A98

Debnath D., Chakrabarti S. K., Mondal S., 2014, Mon. Not. R. Astron. Soc. , 440, L121

Debnath S., Chattopadhyay I., Joshi R. K., 2024a, Mon. Not. R. Astron. Soc. , 528, 3964

Debnath S., Chattopadhyay I., Joshi R. K., 2024b, Mon. Not. R. Astron. Soc. , 528, 3964

Dewberry J. W., Latter H. N., Ogilvie G. I., Fromang S., 2020, Mon. Not. R. Astron. Soc. , 497, 451

Dexter J., Begelman M. C., 2019, Mon. Not. R. Astron. Soc. , 483, L17

Dihingia I. K., Das S., Maity D., Chakrabarti S., 2018a, Phys. Rev. D , 98, 083004

Dihingia I. K., Das S., Mandal S., 2018b, Mon. Not. R. Astron. Soc. , 475, 2164

Dihingia I. K., Das S., Nandi A., 2019a, Monthly Notices of the Royal Astronomical Society, 484, 3209

Dihingia I. K., Das S., Maity D., Nandi A., 2019b, Mon. Not. R. Astron. Soc. , 488, 2412

Dihingia I. K., Das S., Prabhakar G., Mandal S., 2020, Mon. Not. R. Astron. Soc. , 496, 3043

Dihingia I. K., Uniyal A., Mizuno Y., 2025, arXiv e-prints, p. arXiv:2506.05750

Done C., Gierliński M., Kubota A., 2007, The Astronomy and Astrophysics Review, 15, 1

Esin A. A., McClintock J. E., Narayan R., 1997, Astrophys. J. , 489, 865

Evans C. R., Hawley J. F., 1988, Astrophys. J. , 332, 659

Event Horizon Telescope Collaboration et al., 2019, Astrophys. J. Lett. , 875, L1

Event Horizon Telescope Collaboration et al., 2021, Astrophys. J. Lett. , 910, L13

Event Horizon Telescope Collaboration et al., 2022a, Astrophys. J. Lett. , 930, L12

Event Horizon Telescope Collaboration et al., 2022b, Astrophys. J. Lett. , 930, L16

Event Horizon Telescope Collaboration et al., 2022c, The Astrophysical Journal Letters, 930, L16

Event Horizon Telescope Collaboration et al., 2024, Astrophys. J. Lett. , 964, L25

Faghei K., 2012, Mon. Not. R. Astron. Soc. , 420, 118

Faghei K., 2013, Astrophysics and Space Science, 345, 125

Fender R. P., Belloni T. M., Gallo E., 2004, Mon. Not. R. Astron. Soc. , 355, 1105

Fragile P. C., Blaes O. M., Anninos P., Salmonson J. D., 2007, Astrophys. J. , 668, 417

Frank J., King A., Raine D. J., 2002, Accretion Power in Astrophysics: Third Edition. Cambridge, UK: Cambridge University Press

Fryxell B., et al., 2000, Astrophys. J. Suppl. , 131, 273

Fukue J., 1987, Publ. Astron. Soc. Japan , 39, 309

Fukue J., 2019, Mon. Not. R. Astron. Soc. , 483, 2538

Fukumura K., Tsuruta S., 2004, Astrophys. J. , 611, 964

Gammie C. F., McKinney J. C., Tóth G., 2003, Astrophys. J. , 589, 444

Ghanbari J., Abbassi S., Ghasemnezhad M., 2009, Mon. Not. R. Astron. Soc. , 400, 422

Ghasemnezhad M., 2018, Mon. Not. R. Astron. Soc. , 480, 281

Ghoreyshi S. M., Shadmehri M., 2020, Monthly Notices of the Royal Astronomical Society, 493, 5107

Ghosh S., Mukhopadhyay B., 2007, Astrophys. J. , 667, 367

Ghosh T., Rana V., 2021, Mon. Not. R. Astron. Soc. , 504, 974

Ghosh A., Banerjee I., Chakrabarti S. K., 2019, Mon. Not. R. Astron. Soc. , 484, 5802

Giri K., Chakrabarti S. K., Samanta M. M., Ryu D., 2010, Mon. Not. R. Astron. Soc. , 403, 516

Harikesh S., Majumder S., Das S., Nandi A., 2025, Mon. Not. R. Astron. Soc. , 540, 2965

Hawley J. F., Krolik J. H., 2001, Astrophys. J. , 548, 348

Hawley J. F., Krolik J. H., 2002, Astrophys. J. , 566, 164

Hawley J. F., Smarr L. L., Wilson J. R., 1984, Astrophys. J. , 277, 296

Hawley J. F., Gammie C. F., Balbus S. A., 1995, Astrophys. J. , 440, 742

Hawley J. F., Gammie C. F., Balbus S. A., 1996, Astrophys. J. , 464, 690

Heil L. M., Vaughan S., Roberts T. P., 2009, Mon. Not. R. Astron. Soc. , 397, 1061

Hogg J. D., Reynolds C. S., 2018, The Astrophysical Journal, 854, 6

Holzer T. E., Axford W. I., 1970, Ann. Rev. Astron. & Astrophys. , 8, 31

Hoyle F., Lyttleton R. A., 1939, Proceedings of the Cambridge Philosophical Society, 35, 405

Huang C.-Y., Ye Y.-C., Wang D.-X., Li Y., 2016, Mon. Not. R. Astron. Soc. , 457, 3859

Ichimaru S., 1977, Astrophys. J. , 214, 840

Igumenshchev I. V., Narayan R., Abramowicz M. A., 2003, Astrophys. J. , 592, 1042

Ingram A. R., Motta S. E., 2019, New Astronomy Reviews, 85, 101524

Ingram A., van der Klis M., Middleton M., Done C., Altamirano D., Heil L., Uttley P., Axelsson M., 2016, Mon. Not. R. Astron. Soc. , 461, 1967

Iyer N., Nandi A., Mandal S., 2015, Astrophys. J. , 807, 108

Jana C., Das S., 2024, Journal of Cosmology and Astroparticle Physics, 2024, 075

Jana A., Debnath D., Chatterjee D., Chatterjee K., Chakrabarti S. K., Naik S., Bhowmick R., Kumari N., 2020, The Astrophysical Journal, 897, 3

Jiang Y.-F., Blaes O., Stone J. M., Davis S. W., 2019, The Astrophysical Journal, 885, 144

Jiang H.-X., Mizuno Y., Dihingia I. K., Nathanail A., Younsi Z., Fromm C. M., 2024, Astron. Astrophys. , 688, A82

Johnson B. M., Quataert E., 2007, Astrophys. J. , 660, 1273

Kaaret P., Feng H., Roberts T. P., 2017, Ann. Rev. Astron. & Astrophys. , 55, 303

Kanbach G., Straubmeier C., Spruit H. C., Belloni T., 2001, Nature, 414, 180

Kara E., Alston W. N., Fabian A. C., Cackett E. M., Uttley P., Reynolds C. S., Zoghbi A., 2016, Mon. Not. R. Astron. Soc. , 462, 511

Kawaguchi T., 2003, Astrophys. J. , 593, 69

Kawanaka N., Masada Y., 2019, The Astrophysical Journal, 881, 138

Kenzhebayeva S., Toktarbay S., Tursunov A., Kološ M., 2024, Phys. Rev. D , 109, 063005

Khajenabi F., Shadmehri M., 2013a, Mon. Not. R. Astron. Soc. , 436, 2666

Khajenabi F., Shadmehri M., 2013b, Mon. Not. R. Astron. Soc. , 436, 2666

Kim J., Garain S. K., Chakrabarti S. K., Balsara D. S., 2019, Mon. Not. R. Astron. Soc. , 482, 3636

King A. R., Pringle J. E., Livio M., 2007, Mon. Not. R. Astron. Soc. , 376, 1740

Kumar R., Singh C. B., Chattopadhyay I., Chakrabarti S. K., 2013, Mon. Not. R. Astron. Soc. , 436, 2864

Kumar A., Chakrabarti S., Das S., 2025, The Astrophysical Journal, 980, 68

Kylafis N. D., Belloni T. M., 2015, Astron. Astrophys. , 574, A133

Landau L. D., Lifshitz E. M., 1959, Fluid mechanics

Lanzafame G., Molteni D., Chakrabarti S. K., 1998, Mon. Not. R. Astron. Soc. , 299, 799

Latif M. A., Schleicher D. R. G., Khochfar S., 2023, Astrophys. J. , 945, 137

Le T., Becker P. A., 2004, Astrophys. J. Lett. , 617, L25

Lee S.-J., Chattopadhyay I., Kumar R., Hyung S., Ryu D., 2016, Astrophys. J. , 831, 33

Liska M., Hesp C., Tchekhovskoy A., Ingram A., van der Klis M., Markoff S., 2018, Mon. Not. R. Astron. Soc. , 474, L81

Lu J.-F., Gu W.-M., Yuan F., 1999, Astrophys. J. , 523, 340

Lyubarskii Y. E., 1997, Mon. Not. R. Astron. Soc. , 292, 679

Maccarone T. J., Coppi P. S., 2003, Mon. Not. R. Astron. Soc. , 338, 189

Machida M., Nakamura K. E., Matsumoto R., 2006, Publ. Astron. Soc. Japan , 58, 193

MacioŁek-Niedźwiecki A., Krolik J. H., Zdziarski A. A., 1997, Astrophys. J. , 483, 111

Madau P., Haardt F., Dotti M., 2014, Astrophys. J. Lett. , 784, L38

Majumder S., Sreehari H., Aftab N., Katoch T., Das S., Nandi A., 2022, Mon. Not. R. Astron. Soc. , 512, 2508

Majumder S., Das S., Agrawal V. K., Nandi A., 2023, Mon. Not. R. Astron. Soc. , 526, 2086

Majumder S., Chatterjee R., Jayasurya K. M., Das S., Nandi A., 2024, Astrophys. J. Lett. , 971, L21

Majumder S., Das S., Nandi A., 2025, Mon. Not. R. Astron. Soc. , 539, 2064

Mandal S., Chakrabarti S. K., 2005, Astron. Astrophys. , 434, 839

Mandal S., Chakrabarti S. K., 2010, Astrophys. J. Lett. , 710, L147

Mao D.-M., Yu W.-F., 2021, Research in Astronomy and Astrophysics, 21, 170

Marcel G., et al., 2018a, Astron. Astrophys. , 615, A57

Marcel G., et al., 2018b, Astron. Astrophys. , 617, A46

Marino A., et al., 2021, Astron. Astrophys. , 656, A63

Matsumoto R., Tajima T., 1995, Astrophys. J. , 445, 767

Matsumoto R., Kato S., Fukue J., Okazaki A. T., 1984, Publ. Astron. Soc. Japan , 36, 71

McKinney J. C., Gammie C. F., 2004, Astrophys. J. , 611, 977

McKinney J. C., Narayan R., 2007, Mon. Not. R. Astron. Soc. , 375, 513

McKinney J. C., Tchekhovskoy A., Blandford R. D., 2012, Mon. Not. R. Astron. Soc. , 423, 3083

Melia F., Misra R., 1993, Astrophys. J. , 411, 797

Meyer F., Liu B. F., Meyer-Hofmeister E., 2007, Astron. Astrophys. , 463, 1

Mignone A., Bodo G., Massaglia S., Matsakos T., Tesileanu O., Zanni C., Ferrari A., 2007, Astrophys. J. Suppl. , 170, 228

Mignone A., Zanni C., Tzeferacos P., van Straalen B., Colella P., Bodo G., 2012, Astrophys. J. Suppl. , 198, 7

Miller J. M., 2007, Ann. Rev. Astron. & Astrophys. , 45, 441

Miller K. A., Stone J. M., 2000, Astrophys. J. , 534, 398

Mineshige S., Kawaguchi T., Takeuchi M., 2000, New Astronomy Reviews, 44, 435

Mitra S., Das S., 2024, Astrophys. J. , 971, 28

Mitra S., Maity D., Dihingia I. K., Das S., 2022, Mon. Not. R. Astron. Soc. , 516, 5092

Mitra S., Ghoreyshi S. M., Mosallanezhad A., Abbassi S., Das S., 2023, Monthly Notices of the Royal Astronomical Society, 523, 4431

Molla A. A., Debnath D., Chakrabarti S. K., Mondal S., Jana A., 2016, Mon. Not. R. Astron. Soc. , 460, 3163

Molla A. A., Chakrabarti S. K., Debnath D., Mondal S., 2017, The Astrophysical Journal, 834, 88

Molteni D., Lanzafame G., Chakrabarti S. K., 1994, Astrophys. J. , 425, 161

Molteni D., Sponholz H., Chakrabarti S. K., 1996a, Astrophys. J. , 457, 805

Molteni D., Ryu D., Chakrabarti S. K., 1996b, Astrophys. J. , 470, 460

Mondal S., 2023, Astrophys. J. , 950, 26

Mondal S., Chakrabarti S. K., Debnath D., 2014, Astrophysics and Space Science, 353, 223

Mosallanezhad A., Zeraatgari F. Z., Mei L., Bu D.-F., 2021, Astrophys. J. , 909, 140

Mosallanezhad A., Zeraatgari F. Z., Mei L., Bu D.-F., 2022, Astrophys. J. , 926, 182

Motta S. E., Rouco Escorial A., Kuulkers E., Muñoz-Darias T., Sanna A., 2017, Mon. Not. R. Astron. Soc. , 468, 2311

Motta S. E., Franchini A., Lodato G., Mastroserio G., 2018, Mon. Not. R. Astron. Soc. , 473, 431

Mukhopadhyay B., 2002, Astrophys. J. , 581, 427

Nagakura H., Yamada S., 2009, Astrophys. J. , 696, 2026

Nakamura K. E., Machida M., Matsumoto R., 2019, Galaxies, 7, 22

Nandi A., Manickam S. G., Rao A. R., Chakrabarti S. K., 2001, Mon. Not. R. Astron. Soc. , 324, 267

Nandi A., Debnath D., Mandal S., Chakrabarti S. K., 2012, Astron. Astrophys. , 542, A56

Nandi A., et al., 2018, Astrophysics and Space Science, 363, 90

Nandi A., Das S., Majumder S., Katoch T., Antia H. M., Shah P., 2024, Mon. Not. R. Astron. Soc. , 531, 1149

Narayan R., Popham R., 1993, Nature, 362, 820

Narayan R., Yi I., 1994, Astrophys. J. Lett. , 428, L13

Narayan R., Yi I., 1995, Astrophys. J. , 452, 710

Nathanail A., Fromm C. M., Porth O., Olivares H., Younsi Z., Mizuno Y., Rezzolla L., 2020, Mon. Not. R. Astron. Soc. , 495, 1549

Novikov I. D., Thorne K. S., 1973, in Dewitt C., Dewitt B. S., eds, Black Holes (Les Astres Occlus). pp 343–450

Oda H., Machida M., Nakamura K. E., Matsumoto R., 2007, Publ. Astron. Soc. Japan , 59, 457

Ohsuga K., Mineshige S., 2011, Astrophys. J. , 736, 2

Ohsuga K., Mori M., Nakamoto T., Mineshige S., 2005, Astrophys. J. , 628, 368

Okuda T., Das S., 2015, Mon. Not. R. Astron. Soc. , 453, 147

Okuda T., Singh C. B., Das S., Aktar R., Nandi A., Dal Pino E. M. d. G., 2019, Publ. Astron. Soc. Japan , 71, 49

Paczyńsky B., Wiita P. J., 1980, Astron. Astrophys. , 88, 23

Page D. N., Thorne K. S., 1974, Astrophys. J. , 191, 499

Palit I., Janiuk A., Sukova P., 2019, Mon. Not. R. Astron. Soc. , 487, 755

Patra S., Majhi B. R., Das S., 2022, Physics of the Dark Universe, 37, 101120

Patra S., Majhi B. R., Das S., 2024, Journal of High Energy Astrophysics, 44, 371

Peitz J., Appl S., 1997, Mon. Not. R. Astron. Soc. , 286, 681

Penna R. F., McKinney J. C., Narayan R., Tchekhovskoy A., Shafee R., McClintock J. E., 2010, Mon. Not. R. Astron. Soc. , 408, 752

Penna R. F., Sądowski A., McKinney J. C., 2012, Mon. Not. R. Astron. Soc. , 420, 684

Piran T., 1978, Astrophys. J. , 221, 652

Popham R., Gammie C. F., 1998, Astrophys. J. , 504, 419

Porth O., Olivares H., Mizuno Y., Younsi Z., Rezzolla L., Moscibrodzka M., Falcke H., Kramer M., 2017, Computational Astrophysics and Cosmology, 4, 1

Porth O., et al., 2019, Astrophys. J. Suppl. , 243, 26

Poutanen J., Lipunova G., Fabrika S., Butkevich A. G., Abolmasov P., 2007, Mon. Not. R. Astron. Soc. , 377, 1187

Raptis S., Lalti A., Lindberg M., Turner D. L., Caprioli D., Burch J. L., 2025, Nature Communications, 16, 488

Rees M. J., Begelman M. C., Blandford R. D., Phinney E. S., 1982, Nature, 295, 17

Reynolds C. S., Nowak M. A., 2003, *Phys. Rep.* , 377, 389

Rezaie S., Ghasemnezhad M., Golshani M., 2025, New Astronomy, 116, 102348

Rezgui G., Marzougui H., Lili T., Preiner R., Ceccobello C., 2022, Mon. Not. R. Astron. Soc. , 514, 3925

Riffert H., Herold H., 1995, Astrophys. J. , 450, 508

Rybicki G. B., Lightman A. P., 1986, Radiative Processes in Astrophysics

Ryu D., Chakrabarti S. K., Molteni D., 1997, Astrophys. J. , 474, 378

Sano T., Inutsuka S.-i., Turner N. J., Stone J. M., 2004, Astrophys. J. , 605, 321

Sarkar B., Das S., 2016, Mon. Not. R. Astron. Soc. , 461, 190

Sarkar B., Dihingia I. K., Misra R., 2025, New Astronomy, 118, 102377

Schnittman J. D., Krolik J. H., 2010, Astrophys. J. , 712, 908

Sen G., Maity D., Das S., 2022, Journal of Cosmology and Astro-Particle Physics, 2022, 048

Shadmehri M., 2008, Astrophysics and Space Science, 317, 201

Shafee R., Narayan R., McClintock J. E., 2008, The Astrophysical Journal, 676, 549

Shakura N. I., Sunyaev R. A., 1973, Astronomy and Astrophysics, 500, 33

Shang J.-R., Debnath D., Chatterjee D., Jana A., Chakrabarti S. K., Chang H.-K., Yap Y.-X., Chiu C.-L., 2019, The Astrophysical Journal, 875, 4

Shapiro S. L., Teukolsky S. A., 1983, Black holes, white dwarfs and neutron stars. The physics of compact objects, doi:10.1002/9783527617661.

Shapiro S. L., Lightman A. P., Eardley D. M., 1976, Astrophys. J. , 204, 187

Sharma P., Quataert E., Stone J. M., 2008, Mon. Not. R. Astron. Soc. , 389, 1815

Singh M., Das S., 2024, Astrophysics and Space Science, 369, 1

Singh M., Das S., 2025, Journal of Cosmology and Astro-Particle Physics, 2025, 068

Singh C. B., Mondal S., Garofalo D., 2021, Monthly Notices of the Royal Astronomical Society, 510, 807

Singh M., Jana C., Das S., 2025, Journal of Cosmology and Astro-Particle Physics, 2025, 055

Sądowski A., Abramowicz M., Bursa M., Kluźniak W., Lasota J. P., Różańska A., 2011, Astron. Astrophys. , 527, A17

Sądowski A., Narayan R., Tchekhovskoy A., Zhu Y., 2013, Mon. Not. R. Astron. Soc. , 429, 3533

Smith D. M., Heindl W. A., Markwardt C. B., Swank J. H., 2001, Astrophys. J. Lett. , 554, L41

Smith D. M., Heindl W. A., Swank J. H., 2002, Astrophys. J. , 569, 362

Sorathia K. A., Reynolds C. S., Stone J. M., Beckwith K., 2012, Astrophys. J. , 749, 189

Sreehari H., Nandi A., Das S., Agrawal V. K., Mandal S., Ramadevi M. C., Katoch T., 2020, Mon. Not. R. Astron. Soc. , 499, 5891

Steinacker A., Papaloizou J. C. B., 2002, Astrophys. J. , 571, 413

Stone J. M., Norman M. L., 1992, Astrophys. J. Suppl. , 80, 753

Stone J. M., Hawley J. F., Gammie C. F., Balbus S. A., 1996, Astrophys. J. , 463, 656

Stone J. M., Pringle J. E., Begelman M. C., 1999, Mon. Not. R. Astron. Soc. , 310, 1002

Stone J. M., Gardiner T. A., Teuben P., Hawley J. F., Simon J. B., 2008, Astrophys. J. Suppl. , 178, 137

Straub O., et al., 2011, Astron. Astrophys. , 533, A67

Strohmayer T. E., Mushotzky R. F., 2003, in AAS/High Energy Astrophysics Division #7. p. 07.03

Suková P., Janiuk A., 2015, Mon. Not. R. Astron. Soc. , 447, 1565

Suková P., Charzyński S., Janiuk A., 2017, Mon. Not. R. Astron. Soc. , 472, 4327

Sunyaev R. A., Titarchuk L. G., 1980, Astron. Astrophys. , 86, 121

Tanaka T., Menou K., 2006, Astrophys. J. , 649, 345

Tchekhovskoy A., Narayan R., McKinney J. C., 2011, Mon. Not. R. Astron. Soc. , 418, L79

Tejeda E., Rosswog S., 2013, Mon. Not. R. Astron. Soc. , 433, 1930

The Event Horizon Telescope Collaboration et al., 2021a, The Astrophysical Journal Letters, 910, L13

The Event Horizon Telescope Collaboration et al., 2021b, The Astrophysical Journal Letters, 910, L13

TianLe-Zhao XiaoFeng-Li ZeYuan-Tang Kumar R., 2024, arXiv e-prints, p. arXiv:2407.01859

Troyer J. S., Cackett E. M., Peille P., Barret D., 2018, Astrophys. J. , 860, 167

Uttley P., Malzac J., 2025, Mon. Not. R. Astron. Soc. , 536, 3284

Uttley P., Cackett E. M., Fabian A. C., Kara E., Wilkins D. R., 2014, The Astronomy and Astrophysics Review, 22, 72

Varniere P., Vincent F. H., Casse F., 2020, Astron. Astrophys. , 638, A33

Vierdayanti K., Mineshige S., Ebisawa K., Kawaguchi T., 2006, Publ. Astron. Soc. Japan , 58, 915

Volonteri M., Rees M. J., 2005, Astrophys. J. , 633, 624

Wang D.-X., Ye Y.-C., Yao G.-Z., Ma R.-Y., 2005, Mon. Not. R. Astron. Soc. , 359, 36

Wardziński G., Zdziarski A. A., 2000, Mon. Not. R. Astron. Soc. , 314, 183

Watarai K.-y., Mizuno T., Mineshige S., 2001, Astrophys. J. Lett. , 549, L77

Wilson J. R., 1972, Astrophys. J. , 173, 431

Yang R., Kafatos M., 1995, Astron. Astrophys. , 295, 238

You B., et al., 2023, Science, 381, 961

Yu W., et al., 2023, Astrophys. J. , 953, 191

Yuan F., Narayan R., 2014, Ann. Rev. Astron. & Astrophys. , 52, 529

Zamaninasab M., Clausen-Brown E., Savolainen T., Tchekhovskoy A., 2014, Nature, 510, 126

Zhu H., Chen X., Wang W., 2023, Mon. Not. R. Astron. Soc. , 523, 4394